TU Delft

Delft University of Technology

Wave Damping through Woody Vegetation

Kalloe, S.A.

DOI
10.4233/uuid:9e4b00ed-d9a5-4d4d-a8df-48f16fb025bd

Publication date
2025

Document Version
Final published version

Citation (APA)
Kalloe, S. A. (2025). *Wave Damping through Woody Vegetation*. [Dissertation (TU Delft), Delft University of Technology]. https://doi.org/10.4233/uuid:9e4b00ed-d9a5-4d4d-a8df-48f16fb025bd

Important note
To cite this publication, please use the final published version (if applicable).
Please check the document version above.

Copyright
Other than for strictly personal use, it is not permitted to download, forward or distribute the text or part of it, without the consent of the author(s) and/or copyright holder(s), unless the work is under an open content license such as Creative Commons.

Takedown policy
Please contact us and provide details if you believe this document breaches copyrights.
We will remove access to the work immediately and investigate your claim.

This work is downloaded from Delft University of Technology.
For technical reasons the number of authors shown on this cover page is limited to a maximum of 10.

Wave Damping through Woody Vegetation

S.A. Kalloe

Wave Damping through Woody Vegetation

Wave Damping through Woody Vegetation

Proefschrift

ter verkrijging van de graad van doctor
aan de Technische Universiteit Delft,
op gezag van de Rector Magnificus Prof. dr. ir. T.H.J.J. van der Hagen,
voorzitter van het College voor Promoties,
in het openbaar te verdedigen op woensdag 29 januari 2025 om 12:30 uur

door

Sudarshini Aurasia KALLOE

Ingenieur in de Civiele Techniek,
Technische Universiteit Delft, Nederland,
geboren te Paramaribo, Suriname

Dit proefschrift is goedgekeurd door de promotoren.

Samenstelling promotiecommissie:

Rector Magnificus,	voorzitter
Dr. ir. B. Hofland,	Technische Universiteit Delft, *promotor*
Dr. B.K. van Wesenbeeck,	Technische Universiteit Delft, *copromotor*
Onafhankelijke leden:	
Dr. M.E. Maza Fernandez	University of Cantabria
Dr. ir. T. Suzuki	Katholieke Universiteit Leuven
Prof. dr. T. J. Bouma,	Universiteit Utrecht
Dr. M. F. S. Tissier,	Technische Universiteit Delft
Prof. dr. ir. M. R. A. van Gent,	Technische Universiteit Delft
Prof. dr. ir. S. N. Jonkman,	Technische Universiteit Delft, reservelid

Keywords: wave damping, frontal-surface area, vegetation mapping, woody vegetation, flexible mimics, physical modelling

Printed by: Ridderprint, www.ridderprint.nl

Cover by: S. A. Kalloe

Copyright © 2025 by S. A. Kalloe

ISBN 978-94-6518-005-2

An electronic copy of this dissertation is available at
https://repository.tudelft.nl/.

CONTENTS

SUMMARY IX

SAMENVATTING XIII

1 INTRODUCTION 3

1.1 Forest-Dike interventions for Flood Safety . . . 4

1.2 Challenges for wave modelling through vegetation . . . 5

1.3 Research Questions . . . 9

1.4 Research Approach and Report Outline . . . 9

1.4.1 Research Project: WOODY . . . 11

2 VEGETATION FRONTAL-SURFACE AREA 15

2.1 Introduction . . . 16

2.2 Theoretical Background . . . 17

2.2.1 Wave attenuation by vegetation . . . 17

2.2.2 Quantifying vegetation . . . 19

2.3 Methods . . . 22

2.3.1 Physical experiments . . . 22

2.3.2 Methods for quantifying A_v . . . 25

2.3.3 Simulating Wave Attenuation and Bulk Drag Coefficients . . . 30

2.4 Results . . . 32

2.4.1 General characteristics of pollard willows . . . 32

2.4.2 Tree model Results . . . 33

2.4.3 TLS correction factor . . . 34

2.4.4 Comparing Frontal-surface Area . . . 36

2.4.5 Comparing Wave Attenuation . . . 36

2.5 Discussion and Conclusion . . . 38

3 POSSIBLE SCALE AND MODEL ERRORS 45
3.1 Introduction . . . 46
3.2 Methods . . . 47
3.2.1 Experimental Setup . . . 47
3.2.2 Scaling . . . 47
3.2.3 Design of Tree Mimics . . . 49
3.2.4 Forest Characteristics . . . 51
3.2.5 Experimental Conditions . . . 52
3.2.6 Wave Damping, Transmission and Reflection . . . 53
3.2.7 Branch Deflection . . . 54
3.2.8 Extending Data Set . . . 55
3.3 Results . . . 56
3.3.1 Comparing Wave Damping . . . 56
3.3.2 Comparing Branch Motion . . . 56
3.3.3 Correcting Wave Damping . . . 57
3.4 Discussion . . . 57
3.4.1 Reynolds scale effects . . . 59
3.4.2 Flexibility model effects . . . 60
3.4.3 Aeration (Weber) scale effects . . . 62
3.5 Conclusions . . . 62

4 FLEXIBILITY EFFECTS 67
4.1 Introduction . . . 68
4.2 Flume Experiments . . . 69
4.2.1 Experimental Set-up . . . 71
4.2.2 Hydrodynamics . . . 72
4.2.3 Vegetation Mimics . . . 72
4.3 Data processing . . . 74
4.3.1 Force Measurements . . . 74
4.3.2 Velocity profiles - Regular Waves . . . 76
4.3.3 Video Images Cones . . . 76
4.4 Results and Discussion . . . 77
4.4.1 Realistic Tree Mimics . . . 77
4.4.2 Flexible Cones . . . 79
4.4.3 Drag Coefficients of Cones . . . 80
4.4.4 Cone Deflections . . . 82

4.4.5 Force reduction . . . 82
4.5 Conclusions . . . 86

5 DISCUSSION TOWARDS APPLICATION 91
5.1 Introduction . . . 92
5.2 A Case Study . . . 93
5.2.1 Deterministic calculation . . . 95
5.2.2 Reduced Probability of Flooding . . . 98
5.3 Potential Locations . . . 100
5.3.1 Mapping Willow Forest Locations . . . 100
5.4 Implementation of riparian forests in flood protection system: an Outlook . . . 101

6 CONCLUSIONS & RECOMMENDATIONS 107
6.1 Main Findings . . . 108
6.2 Recommendation further research . . . 111
6.2.1 Future Measurements . . . 111
6.2.2 Modelling Practices . . . 112

REFERENCES 113

A WAVE DAMPING UNDER STORM CONDITIONS 125
A.1 Introduction . . . 126
A.2 Results . . . 126
A.2.1 Experimental setup . . . 126
A.2.2 Reduction in wave height and run-up through the forest . . . 128
A.2.3 Implications of measurements for wave-vegetation modelling . . . 130
A.3 Discussion . . . 133
A.4 Methods . . . 134
A.4.1 Wave measurements . . . 134
A.4.2 Vegetation measurements . . . 135
A.4.3 Frontal surface area distribution . . . 135
A.4.4 Wave dissipation model . . . 136
A.4.5 Statement on plant materials . . . 137

B SUPPORTING INFORMATION CHAPTER 2 139
B.1 Wave conditions . . . 140

B.2 Tree parameters forest . . . 140
B.3 Position primary branches on the trunk . . . 140
B.4 Analytical Formulation Including for Layers . . . 140

C SUPPORTING INFORMATION CHAPTER 3 145
C.1 Experimental conditions . . . 146
C.2 Branch Motion Real-scale Experiments . . . 148
C.2.1 Sensitivity Analysis . . . *148*
C.3 Difference in Wave damping by Re . . . 150
C.3.1 Analytical Formulation . . . *152*

D SUPPORTING INFORMATION CHAPTER 4 155
D.1 Full Program . . . 156
D.1.1 Hydrodynamic Conditions . . . *156*
D.2 Printer settings . . . 156
D.3 Fenton . . . 157
D.4 Dynamic response cone . . . 157
D.5 Video Images - Post processing . . . 160
D.6 Force-velocity relation complex tree . . . 161
D.7 Possible High Frequency Oscillations in Force Data . . . 162
D.8 Peak Forces on Cones . . . 163
D.9 Peak Forces on 6-Cone Tree . . . 163

E SUPPORTING INFORMATION CHAPTER 5 165
E.1 Vegetatielegger . . . 165
E.2 Dike Design . . . 167
E.2.1 Overtopping . . . *167*
E.2.2 Wave impact . . . *167*
E.2.3 Wave run-up . . . *168*

LIST OF SYMBOLS 174

ACKNOWLEDGEMENTS 175

ABOUT THE AUTHOR 179

SUMMARY

Riparian forests in front of levees can dampen incoming waves and reduce erosion, thereby decreasing the risk of flooding. This makes them a sustainable addition to stand-alone dikes, potentially decreasing the overall costs for future dike reinforcement measures. However, there are currently no guidelines for the design, monitoring, and maintenance of dike-forest combinations as significant uncertainties remain. For instance, most studies on the effectiveness of forests in attenuating waves focus on mild wave climates or rely on scaled tests using simplified tree mimics. As a result, prototype-scale studies on wave damping by forests under extreme conditions—essential for design and assessment purposes—are lacking.

This thesis investigated wave damping by riparian forests, with a specific focus on pollard willow trees, which are commonly found along the riverbanks in the Netherlands and other parts of Europe. The primary aim was to reduce the uncertainties associated with the application of forest-dike combinations. The foundation and source of innovation for this thesis is the data from real-scale flume tests *(van Wesenbeeck et al., 2022)*, conducted on a 40-m-long live pollard willow forest, subjected to significant wave heights up to 1.5 metres (Appendix A). The analysis of these tests revealed several important areas for further investigation.
First, the vertical frontal-surface area (A_v) distribution of leafless trees should be measured in detail (Chapter 2), as leaves were found to minimally affect wave damping. Second, flume studies at various scaled often form the basis of calibration and validation of analytical, numerical and empirical wave-vegetation models, however, the extent to which small-scale tests accurately represent wave-vegetation interaction at real scale remains unknown. The data from the real-scale tests made it possible to design scaled tests (with 3D-printed tree mimics) and compare the results between both scales (Chapter 3). Lastly, during real-scale tests, the live tree branches were observed to sway by nearly 180 degrees under the highest water levels and wave conditions, highlighting the importance of and need for further research into branch flexibility (Chapter 4).

Numerical models of vegetation largely underestimate the vegetation surface by assuming that vegetation consists of only stems and a single branch order and by neglecting tapering of branches. In Chapter 2, we investigate methods to obtain accurate A_v distributions over the height of live willow trees. One method used a combination of manual measurements and tree allometry relations to create *tree models* (resulting in a detailed representation of A_v). This method was compared to the results of a relatively more practical method: Terrestrial Laser Scanning. The findings showed a large variation of (calibrated) bulk drag coefficients between measuring methods and highlight the importance of reliable frontal-surface area estimations and consequently for reliable wave attenuation predictions.

Until now, no prior studies have compared real-scale and scaled tests with woody vegetation. We therefore conducted scaled tests with complex 3D-printed willow tree mimics to explore scale effects in scaled tests with vegetation (Chapter 3). The maximum measured wave damping (30%) was shown to be roughly 1.5 times higher than the real-scale tests (20%) for water levels just above the knot of the trees. The amount of wave height damping decreased for larger water levels, following the same trend as that of the real-scale tests. The largest effects were attributed to increased viscous damping (due to smaller branch Reynolds numbers), and non-exact flexibility scaling. These notable deviations illustrate that real-scale tests, though expensive, may still be needed to validate the results of scaled tests for woody vegetation. Alternatively, accounting for these discrepancies can increase the reliability of scaled tests for wave damping studies on woody vegetation and reduce the need for more expensive real-scale tests.

Additionally, scaled tests with flexible conical shapes were conducted to study the effects of flexibility on wave damping in greater detail (Chapter 4). The first-mode cone deflection was determined at ≈ 0.7 times the length of the cone to avoid higher-order modes in the measurements. The findings showed that cone deflections greater than 5° had a large spread in force reduction and resulted in a significant decrease in measured forces of up to 50% compared to their rigid counterparts. This work demonstrated that the effective length principle, which has already been successfully applied to grassy vegetation such as salt marshes and seagrass, is a promising dimensionless parameter for predicting force reduction in conical shapes–and could potentially be extended to tree canopies.

Lastly, the experimental data was used as input for analytical wave damping models, which allowed us to discuss the opportunities for riparian forest-dike solutions

in the Netherlands (Chapter 5). The outcome of our probabilistic study suggested that pollard forests in front of existing dikes offered the greatest benefit in mitigating failure caused by the erosion of grass on the outer-slope of the dike due to wave impact. We also discussed that the height of the trunk, which determines the location of the knot—where the frontal surface area, and consequently wave damping, are greatest—can serve as a key design parameter for forest-dike systems.

The thesis offers an overview of key parameters and their associated uncertainties, contributing to the ongoing integration of (riparian) forests into dike design and assessment methodologies.

SAMENVATTING

Rivierbossen voor dijken kunnen inkomende golven dempen en erosie verminderen, waardoor het overstromingsrisico afneemt. Dit maakt ze een duurzame aanvulling op tranditionele dijken, met mogelijk lagere kosten voor toekomstige dijkversterkingsmaatregelen. Er zijn echter momenteel geen richtlijnen voor het ontwerp, de monitoring en het onderhoud van dijk-boscombinaties, omdat er nog aanzienlijke onzekerheden zijn. Bijvoorbeeld, de meeste studies naar de effectiviteit van bossen bij het dempen van golven richten zich op milde golfklimaten of maken gebruik van geschaalde testen met vereenvoudigde boom replicas. Hierdoor ontbreken studies op prototypeschaal naar golvendemping door bossen onder extreme omstandigheden– essentieel voor ontwerp–en beoordelingsdoeleinden.

In deze dissertatie is onderzocht hoe oeverbossen golven dempen, met specifieke aandacht voor knotwilgen, die veel voorkomen langs de rivieren in Nederland en andere delen van Europa. Het primaire doel was om de onzekerheden rondom de toepassing van dijk-boscombinaties te verminderen. De basis en bron van innovatie voor dit proefschrift is data van grootschalige testen, uitgevoerd op een 40 meter lang levend knotwilgenbos, blootgesteld aan significante golfhoogtes tot 1,5 meter (Appendix A). Analyse van deze testen bracht verschillende belangrijke onderzoeksvragen naar voren.
Ten eerste zou de verticale frontale-oppervlakte (A_v) van bladloze bomen in detail gemeten moeten worden (Hoofdstuk 2), aangezien bladeren een minimale invloed hadden op de golfdemping. Ten tweede vormen goottesten op verschillende schalen vaak de basis voor de kalibratie en validatie van analytische, numerieke en empirische golf-vegetatiemodellen, maar de mate waarin kleinschalige testen interactie tussen golven en vegetatie op ware schaal correct weergeven, blijft onbekend. De data van de grootschalige experimenten maakte het mogelijk om geschaalde experimenten (met 3D-geprinte boom replicas) te ontwerpen en de resultaten tussen beide schalen te vergelijken (Hoofdstuk 3). Ten slotte werden tijdens de grootschalige experimenten levende boomtakken waargenomen die tot bijna 180 graden bewogen onder de

hoogste waterstanden en golfomstandigheden, wat het belang en de noodzaak benadrukt van verder onderzoek naar het effect van de flexibiliteit van de takken op de golfdemping (Hoofdstuk 4).

Numerieke vegetatiemodellen onderschatten vaak het vegetatieoppervlak door aan te nemen dat vegetatie alleen uit stammen en één takorde bestaat en de vernauwing in de diameter van de takken te negeren. In Hoofdstuk 2 onderzoeken we methoden om nauwkeurige A_v-verdelingen over de hoogte van levende knotwilgen te verkrijgen. Eén methode combineerde handmatige metingen en boom-allometrische relaties om *boommodellen* te creëren (resulterend in een gedetailleerde weergave van A_v). Deze methode werd vergeleken met de resultaten van een relatief praktischere methode: Terrestrische Laser Scanning. De bevindingen toonden een grote variatie in (gekalibreerde) bulkweerstandscoëfficiënten tussen meetmethoden en benadrukken het belang van betrouwbare schattingen van de frontale-oppervlakte, en daarmee voor betrouwbare voorspellingen van golfdemping.

Tot nu toe hebben eerdere studies geen grootschalige en geschaalde experimenten met houtachtige vegetatie vergeleken. Daarom voerden we geschaalde experimenten uit met complexe 3D-geprinte knotwilgenmodellen om schaaleffecten te onderzoeken (Hoofdstuk 3). De maximale gemeten golfdemping (30%) was ongeveer 1,5 keer hoger dan bij de grootschalige testen (20%) bij waterstanden net boven de knot van de bomen. De hoeveelheid golvendemping nam af bij grotere waterstanden, volgend dezelfde trend als die van de grootschalige testen. De grootste effecten werden toegeschreven aan verhoogde viskeuze demping (door kleinere tak-Reynolds-getallen) en niet-exacte schaalverhoudingen in flexibiliteit. Deze afwijkingen illustreren dat grootschalige experimenten, hoewel duur, mogelijk nog steeds nodig zijn om de resultaten van geschaalde experimenten met houtachtige vegetatie te valideren. Alternatief kan het corrigeren voor deze discrepanties de betrouwbaarheid van geschaalde experimenten voor studies naar golvendemping door houtachtige vegetatie verhogen en de noodzaak voor duurdere grootschalige experimenten verminderen.

Bovendien zijn geschaalde experimenten met flexibele conische vormen uitgevoerd om de effecten van flexibiliteit op golvendemping in meer detail te bestuderen (Hoofdstuk 4). De eerste-mode kegeldeflectie werd bepaald op $\approx 0{,}7$ keer de lengte van de kegel om hogere-orde modi in de metingen te vermijden. De bevindingen toonden aan dat kegeldeflecties groter dan 5° een grote spreiding hadden in krachtreductie en resulteerden in een significante afname van gemeten krachten tot 50% in vergelijking met hun rigide equivalent. Dit onderzoek toonde aan dat het effectieve

lengteprincipe, dat al succesvol is toegepast op grasachtige vegetatie zoals kwelders en zeegras, een veelbelovende dimensieloze parameter is voor het voorspellen van krachtreductie in conische vormen—en mogelijk kan worden uitgebreid naar boomkruinen.

Ten slotte zijn de experimentele data gebruikt als input voor analytische golvendempingsmodellen, waarmee we de mogelijkheden voor oeverbos-dijkoplossingen in Nederland hebben besproken (Hoofdstuk 5). Het resultaat van onze probabilistische studie suggereerde dat knotwilgbossen voor bestaande dijken het grootste voordeel boden bij het beperken van falen door erosie van gras op de buitentalud van de dijk door impact van de golven. We hebben ook besproken dat de hoogte van de stam, die de locatie van de knot bepaalt–waar de frontale oppervlakte en daarmee de golvendemping het grootst zijn–als een belangrijke ontwerpparameter voor dijkbossystemen kan dienen.

Deze dissertatie biedt een overzicht van sleutelparameters en hun bijbehorende onzekerheden en draagt bij aan de voortdurende integratie van (oever)bossen in dijkontwerp- en beoordelingsmethodologieën.

Photography by Mischa Keijser

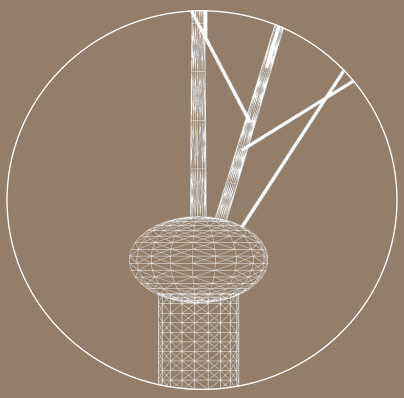

1

Introduction

1

1.1. Forest-Dike interventions for Flood Safety

Climate change affects us on a global scale, in the form of rising temperatures, more intense storms, prolonged droughts, heavier rainfall, and accelerated sea level rise *(IPCC, 2022)*. As most of the world's urbanisation occurs in coastal regions, hundreds of millions of people are foreseen to be impacted, primarily through increased flooding *(Wong et al., 2013)*. Human activities increase the vulnerability of coastal and riverine environments to these threats, particularly through actions such as large-scale deforestation and upstream damming of rivers. This can, for instance, lead to land subsidence, increasing the risk of floods and causing harm to surrounding ecosystems (*Syvitski et al., 2009*; *van Wesenbeeck et al., 2014*). Consequently, today these systems face the challenge of protecting more vulnerable hinterlands, where the risk of flooding increases by both exacerbated natural and human-induced factors.

Conventional flood protection mainly uses 'hard measures', such as dikes and dams, which can disrupt sediment fluxes, can negatively impact ecosystems, and often require frequent dike reinforcement. Awareness of the anthropogenic origin of these environmental challenges has led to climate policies with mitigation and adaptation to climate change as the main objectives. These objectives are followed by many organisations that are exploring new approaches to combat climate change. Flood protection is a good example of a field in need of more attention and could offer the possibility of implementing more sustainable solutions than those used in the past.

Nature-based flood defences, in particular dike-vegetation combinations, can attenuate waves, decrease storm surges, and increase sedimentation. It is also found that vegetation provides resilience against sea level rise, if there is sufficient sediment supply *(Fu et al., 2019)* and accommodation space *(Schuerch et al., 2018)*. This can make Nature-inclusive solutions (often referred to Nature-based Solutions, NbS) more adaptive and cost-effective than conventional flood protection methods. In addition to flood safety benefits, NbS provides several other ecosystem services. Well-known examples are creating breading areas, increasing biodiversity, providing shelter for species *(Rog et al., 2017)* and functioning as carbon sinks *(Chen et al., 2015)*. Although the role of wetlands has been underestimated in the past, there is a growing recognition worldwide of their importance as low-impact multipurpose alternatives to conventional flood defences *(IPCC, 2022)*.

The widely known types of vegetation found in front of flood defences can be aquatic plants (e.g., sea grass), salt marshes, and woody vegetation such as man-

groves and willow trees. Mangroves are highly salt-tolerant plants and are present in coastal ecosystems in the tropics and subtropics. The areas with the most common mangrove genus *Rhizophora* and *Avicennia*, are shown in Figure 1.1. In fresh water habitats, the Salicaceae family, with two living genera namely *Salix* (willows) and *Populus* (poplars) *(Taylor, 2009)*, is preeminent along floodplains in the northern temperate zone *(Karrenberg et al., 2002)*. The locations of *Salix Alba* (a species in the genera *Salix*) are shown in Figure 1.1. These are deciduous trees and can have various tree geometries, depending on pruning practices (see Figure 1.2A). Cypress and Tupelo forests (e.g., *Nainar et al., 2021*) are other examples of freshwater forest ecosystems that can contribute to the safety against flooding.

Unfortunately, the outcome of most wave damping studies through vegetation is site-specific and generally leads to wave damping predictions with large uncertainty. As a consequence, usually high safety factors and therefore high costs are associated with these solutions. An example of where a willow forest is already applied as part of the flood protection system in a riverine area in the Netherlands is the Noordwaard (see Figure 1.3). Still, the majority of riparian forests are not yet included as part of the flood protection system (e.g., see Figure 1.2B).
The design of 'hard' structures, such as a breakwater with distinct armour units or unusual slopes, requires additional testing prior to implementation. This is also the case for forest-dike interventions. Hence, a generalised formulation is needed for a more accurate quantification of these phenomena to promote the presence of vegetation in our flood protection policies and designs.

1.2. Challenges for wave modelling through vegetation

Several studies have been conducted on wave damping through vegetation fields; however, there is a wide spread in the findings. Predictions of wave attenuation through vegetation fields require understanding of wave-vegetation interactions, which depend on both vegetation and hydrodynamic parameters. The amount of wave dissipation through vegetation fields is expressed as the amount of work done by the waves on vegetation *(Suzuki, 2011)*. The effects of vegetation on the incoming wave energy are in most cases predicted with a formulation of *Dalrymple et al. (1984)*, which is extended by *Mendez and Losada (2004)*. This analytical model uses a parametrisation of the drag force using a bulk drag coefficient C_D *(Mendez and Losada, 2004)*.

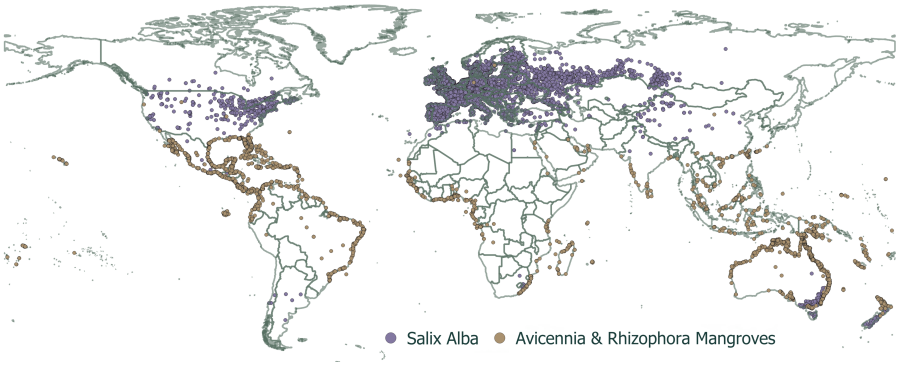

Figure 1.1.: Global occurrence of mangroves (*Rhizophora* and *Avicennia*) and willow trees (*Salix Alba*) *(Data from: gbif.org)*

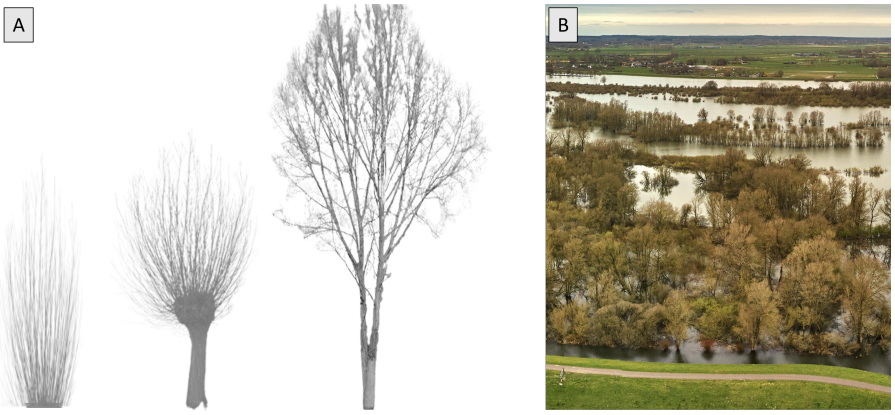

Figure 1.2.: A: An example of a mechanically pruned, manually pruned (also known as pollard willow), and natural willow tree of the species *Salix Alba*; B: Riparian forest partly submerged in front of a dike in the Netherlands, however, not yet accounted for in the flood safety assessment (source: Waterschap Drents Overijsselse Delta)

The bulk drag coefficient is usually fitted to experimental results and also accounts for physical processes which are undefined in the formula, such as changes in velocity profiles inside canopies and flexibility of branches, which makes this coefficient dependent on many parameters and hence difficult to predict. Several studies have been conducted on salt marshes (*Mullarney and Henderson, 2010*; *Maza et al., 2015*; *Vuik, 2019*) and aquatic vegetation (*Luhar and Nepf, 2011*; *Gijón Mancheño, 2016*). However, due to the lack of a generic practical formulation, it is not straightforward how to extend the results of these tests to woody vegetation.

The following knowledge gaps are identified to progress towards a generic practical formulation for wave damping through woody vegetation:

Performance under storm conditions - Data on wave damping by vegetation are mostly gathered from scaled flume tests (e.g., *Maza et al., 2019*), field measuring campaigns (e.g., *Vuik, 2019*), or large-scale tests with salt marshes *(Möller et al., 2014)*. Most field measurement campaigns showed promising wave attenuation rates by mangroves (*Mazda et al., 2006*; *Quartel et al., 2007*); however, these often do not cover extreme conditions. Furthermore, relevant assessments have been made on the breakage of the stems of salt marshes under storm conditions *(Vuik, 2019)*, but are lacking for woody vegetation. Thus, there is a lack of data on wave damping performance and on the breakage of woody vegetation under storm conditions.

Geometric complexity - Oscillatory flow through an array of rigid cylinders depends on the cylinder spacing, density, stroke of motion of the waves, and other flow conditions *(Suzuki, 2011)*. As woody riparian vegetation has a complex tree geometry, the hydrodynamics within these structures is difficult to capture and predict. The geometric complexity of woody vegetation can also lead to inadequate capture of the vegetation structure and to discrepancies in the drag coefficient values. Usually, in field measurements, the structure of plants is simplified and can be a reason for the high scattering of the results. Furthermore, the large variations in space and time of vegetation characteristics make quantifying vegetation parameters more difficult. Measurement methods to identify the plant characteristics, especially frontal-surface area, and how the used method affects the wave damping results, have not yet been

Figure 1.3.: Willow forest in the Noordwaard, the Netherlands (Photo Credit: Robbert de Koning, Jeroen Bosch). At high water in the river the retention area at the foreground floods, and the forest (green arrow) protects the grass-covered dike (white arrow) against wave attack.

investigated for woody vegetation.

Possible model and scale effects - Most wave damping studies use data from laboratory experiments. Laboratory studies have the advantage of testing under controlled hydraulic conditions and can be performed at different scales depending on the flume size. Large-scale or full-scale tests are relatively expensive compared to (small) scaled experiments, while scaled experiments are limited by the dimensions of the flume. Furthermore, scaled experiments generally use stiff cylinders *(Hu et al., 2014)* and scaled-down woody vegetation mimics. This can lead to limitations in reproducing the physics behind wave-vegetation interactions because, for instance, there is an inadequate resemblance to the mechanical behaviour of woody vegetation under wave loads. Furthermore, scaling down woody vegetation is a multiscale problem (i.e., water depths of metres, vegetation stems of decimetres, and branches of centimetres to millimetres), which poses another challenge. Thus, data from controlled laboratory scaled experiments are prone to scaling or model errors *(Heller, 2011)*, and comparisons with real-scale tests are lacking for woody vegetation.

Flexibility effects - Flexibility is shown to be an important parameter for predicting wave attenuation over aquatic vegetation, such as sea-grass and kelp (e.g., *Luhar and Nepf, 2011*; *van Veelen et al., 2020*). Several studies focused on the flexibility of a single stem *(Luhar and Nepf, 2016)* or in sea-grass meadows *(Lei and Nepf, 2019)*, which showed that flexible vegetation introduces less wave damping compared to less flexible vegetation. In the case of woody vegetation, evidence is lacking on the role of flexibility of woody vegetation in oscillatory flow. This is especially the case for the canopy that consists of varying branches and side-branches that taper in diameter. A smaller diameter corresponds to a lower rigidity (higher flexibility). As mentioned previously, the drag coefficient is indirectly accounting for all processes; the quantification of which is still unknown, including the unaccounted processes due to vegetation motion.

This thesis will address the identified knowledge gaps and offer insights that will support the development of guidelines for integrating vegetation into flood protection systems. For these approaches to be incorporated into Dutch flood protection standards, it is crucial to first reduce the uncertainties associated with vegetation-dike solutions *(Het Expertise Netwerk Waterkeren, 2007)*.

1.3. Research Questions

The focus of this research lies in wave transformation and wave dissipation through woody vegetation in oscillatory flow. The role of the flexibility of woody branches and its effect on wave damping is an important aspect. The following research question is formulated:

How can uncertainties in wave predictions through woody vegetation be limited?

This study has the following sub-questions:

i) How much wave damping through forests can we expect under storm conditions?

ii) How can we obtain reliable vegetation input for current wave damping formulas?

iii) What is the potential magnitude of scale or model errors when conducting scaled experiments with woody vegetation?

iv) How can the flexibility effect of woody vegetation be implemented in current wave damping models?

1.4. Research Approach and Report Outline

The sub-questions presented in Section 1.3 will be answered by means of evidence from physical experiments at two scales, namely real-scale (1:1) and 1:10 scaled experiments. This will be used to suggest input values or adjustments for our current analytical expressions to predict wave damping through woody vegetation. This is depicted in Figure 1.4, showing the body of the thesis and the input flows with the arrows between the chapters.

Appendix A - Wave damping under storm conditions

This Appendix shows the real-scale flume experiments with a 40-m-long forest (i.e., 32 live pollard willow trees, species *Salix Alba*) conducted in the Delta flume in the Netherlands. The tests included two water depths at the location of the trees, significant wave heights of up to 1.5 metres, and peak wave periods of up to 7 seconds. The wave damping obtained from different vegetation configurations, namely the 100% canopy density with leaves and without leaves, and the 50% canopy density without

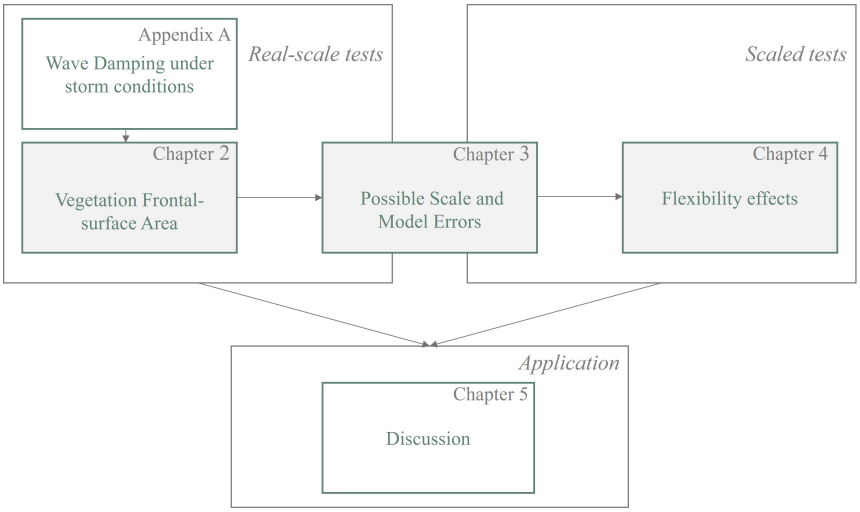

Figure 1.4.: Schematic overview of research methodology and report outline.

leaves, are presented.

Chapter 2 - Vegetation frontal-surface area

In this chapter we show different methods for quantifying the tree's frontal-surface area distribution along the vertical. The real-scale experimental tests with live woody vegetation (*Salix Alba*) under storm conditions, introduced in the previous chapter, are further analysed. These methods are compared in terms of practicality and their effect on wave dissipation by considering the resulting drag coefficient. The proposed method, which relies on species-specific allometric relationships, is used to develop tree model mimics for scaled experiments in the next chapter. In addition, the tree model's result is further explored in Chapter 5, where the integration of vegetation into flood safety assessments is discussed.

Chapter 3 - Possible scale and model errors

Scaled experiments (1:10 scale) using 3D-printed realistic tree mimics are presented. These tests mimic the real-scale tests (described in Chapter 2). Finally, by comparing the tree motion and wave damping at both scales, scale and model effects are identified, which will allow for ways to account for them.

Chapter 4 - Flexibility effects

The effect of the flexibility of the woody branches on the amount of wave damping

will be the focus of this chapter. We simplified the branch geometry to conical shapes with varying flexibility, and conducted scaled flume tests under regular waves. The experimental results can be used in a (quasi-static) model for predicting the cone motion, the corresponding forces, and thereby the wave damping from the simplified objects.

Chapter 5 - Discussion towards Application

We will reflect on this research by considering the applicability of woody vegetation in the Netherlands. The influence of pollard willows on the failure probability for wave impact on grass erosion is determined for a location in the Netherlands, including the influence of flexibility. Moreover, locations where at present sufficient vegetation might be available that can be taken into account for flood safety are identified.

Chapter 6 - Conclusions & Recommendations

The thesis ends with an overview of the conclusions and recommendations derived from the preceding chapters.

1.4.1. Research Project: WOODY

This dissertation is part of the project WOODY, which studies full-scale hydraulic and ecological optimisation of a dike-forest combination. The project is a sequel of the Woodsversuswaves project on real-scale flume tests with live trees. The WOODY project consists of 3 work packages (WP). WP1 is about modelling wave damping through forests, which is discussed in this thesis; WP2 is focused on ecology and whether dike-forest combinations support nature goals, by Corrine van Starrenburg, and WP3 which is on failure mechanisms of forests and creating guidelines for dike-forest combinations, by Alejandra Gijon. All WOODY data can be found in the 4TU repository. This project is financed by the Dutch Research Council (NWO) through the Open Technology Program, number 17194. This project is supported by Rijkswaterstaat, NIOZ, Deltares, Waterschap Drents Overijsselse Delta, Van Oord, Boskalis, and the World Wildlife Fund.

Photography by Mischa Keijser

2

Vegetation Frontal surface area

This Chapter has been published in *Frontiers in Marine Science* as:

Kalloe, S.A., Hofland, B., Antolínez, J., & van Wesenbeeck, B. K. (2022a). Quantifying Frontal-surface Area of Woody Vegetation: A Crucial Parameter for Wave Attenuation. *Frontiers in Marine Science*, 9(March), 1–18. https://doi.org/10.3389/fmars.2022.820846

2.1. Introduction

Current flood protection systems are under pressure due to climate change, in the form of more intense and frequent storms, heavier rainfall, and accelerated sea level rise *(Oppenheimer et al., 2019)*. Dikes will need to be made higher and stronger to keep up with changing climate, which will increase costs *(Jonkman et al., 2013)*. Because of this, the interest in more cost-effective solutions has grown in recent years for both coasts and rivers. Using vegetation in front of dikes has attracted a lot of attention for its contribution to flood safety, as it adapts to rising sea levels, promotes sedimentation and is able to attenuate incoming waves *(van Wesenbeeck et al., 2013)*. In addition to flood safety benefits, these so-called eco-engineering solutions or hybrid flood defences provide several ecological benefits, such as increasing biodiversity by providing nursery habitat for fish and breeding areas for birds *(Rog et al., 2017)*.

Many studies were conducted on wave attenuation (oscillatory flow) through vegetation fields, such as kelp *(Mendez and Losada, 2004)*, salt marshes *(Vuik, 2019)* and mangroves (*Mazda et al., 2006*; *Quartel et al., 2007*). Two processes that lead to wave energy damping through vegetation are wave breaking and wave-vegetation interactions *(Vo-Luong and Massel, 2008)*. Both vegetation characteristics (such as vegetation density, geometry and height) and hydrodynamic conditions (such as wave-current interactions, wave orbital velocity, and wave period *(Hu et al., 2014)* influence these processes. The hydrodynamics around one rigid cylinder and an array of rigid cylinders is relatively well understood under oscillatory flow, and is commonly used to mimic the presence of vegetation fields in physical and numerical models. These models use a simplified description of tree structures containing a single diameter and density of branches. Woody vegetation, such as mangroves in tropical regions and willow trees in temperate regions, has complex structures (i.e., varying branch densities, diameters, and angles). These structures not only make it difficult to capture the hydrodynamics, but also the vegetation parameters (such as frontal-surface area), which is needed to estimate the wave attenuation. This, along with spatial and seasonal variations of the vegetation, can lead to inadequate estimates of vegetation parameters. Usually, the structure of plants is simplified (e.g., rigid cylinders with a certain diameter and density) in analysis of field measurements and is assumed to be constant in space or roughly divided into coarse layers *(Suzuki, 2011)*. These simplifications affect the wave attenuation from numerical or physical models, which in turn can be one of the reasons for the wide range of C_D values found in literature (e.g., *Wu and Cox, 2015*; *He et al., 2019*). To gain more insight into the dissipation of wave energy through woody vegetation fields, it is necessary to have reliable es-

timates of the relevant vegetation parameters and accurate ways of measuring them. We hypothesise that current methods of representing vegetation (illustrated in Figure 2.1) are overly simplified and that more thorough vegetation quantification including diameter tapering and branch angles will improve model predictions of vegetation and wave reduction.

The purpose of this study is to compare different methods for quantifying the frontal-surface area of woody vegetation and to present their effect on wave damping predictions. We used data from large-scale flume experiments with live willow trees under storm conditions, where significant wave heights, H_{m0}, up to 1.5 m were tested *(van Wesenbeeck et al., 2022)*. During these physical experiments, both manual measuring techniques and Terrestrial laser scanning (TLS) were performed; these are described in Section 2.3. The frontal-surface area estimation from the TLS data is compared to *tree models* (i.e., simplified representations of the tree structure). These *tree models* are developed by combining manual measurements and allometric relations, which are also included in Section 2.3. Afterwards, we used SWAN to calculate the wave damping corresponding to the different tree models and the TLS output. These results are compared to the wave damping measured from large-scale experiments in Section 2.4. Finally, methods for quantifying the frontal-surface area of vegetation, and recommendations for further research are suggested in Section 2.5.

2.2. Theoretical Background

2.2.1. Wave attenuation by vegetation

Many studies predicted the wave attenuation by vegetation using an increased bottom friction coefficient (e.g., *Hasselmann and Collins, 1968*; *Quartel et al., 2007*), while other studies (e.g., *Dalrymple et al., 1984*; *Kobayashi et al., 1993*) represented the vegetation as an array of cylinders, considering the wave forcing on these structures. The latter approach (i.e., cylinder approach) relates the wave attenuation to the plant geometry (i.e., the vegetation height, diameter, and density), which is preferred over the former. Studies such as *Dalrymple et al. (1984)* used the time-averaged energy conservation equation. Here, the wave energy dissipation by vegetation, ε_v, is due to the work done by the waves on the vegetation, integrated over the submerged vegetation height. The time-averaged rate of wave energy dissipation per unit horizontal area becomes:

$$\frac{\partial}{\partial x}\left(\frac{1}{8}\rho_w g H^2 c_g\right) = \varepsilon_v \,, \tag{2.1}$$

$$\varepsilon_v = \int_{-h}^{-h+h_v} Fu\, dz\,, \tag{2.2}$$

The resulting force on the vegetation is given by the Morison equation *(Morison et al., 1950)*:

$$F_x = F_D + F_i = \frac{1}{2}\rho_w C_D b_v N u u + \frac{\pi}{4}\rho_w C_M b_v^2 N \frac{\partial u}{\partial t}\,, \tag{2.3}$$

where F_D is the drag force and F_i is the inertia force. The Morison equation is solely suitable for determining the drag forces on slender objects (neglecting diffraction of waves around the object). We can still use this equation for predicting drag forces on trees with low canopy densities (i.e., no porosity effects namely effects of blockage and sheltering) *(Etminan et al., 2019)*, and the ratio between the wave length and the diameter of the individual branches is small. Furthermore, most studies assume linear wave theory to be valid within vegetation fields; therefore, the total force on the vegetation is solely due to the drag forces as the inertia forces are out of phase with the velocity signal. *Dalrymple et al. (1984)* found an analytical solution for the wave height evolution through a vegetation field. His study focused on vegetation on a flat bottom subject to regular waves. This application has been extended by *Mendez and Losada (2004)*, taking into account the sloping bottom and irregular waves. The wave height decay through a vegetation field can be determined with the following equation *(Mendez and Losada, 2004)*:

$$\frac{H_{rms}}{H_{rms,in}} = \frac{1}{1+\beta X}\,, \tag{2.4}$$

with the wave attenuation coefficient, β, as

$$\beta = \frac{1}{3\sqrt{\pi}}\widetilde{C}_D b_v N k \frac{\sinh^3 kh_v + 3\sinh kh_v}{(\sinh 2kh + 2kh)\sinh kh} H_{rms,in}\,, \tag{2.5}$$

where H_{rms} is the root-mean-square wave height behind the vegetation field, $H_{rms,in}$ is the incoming root-mean-square wave height (in front of the forest m), X is the distance inside the forest, $\widetilde{C}_D$ is the bulk drag coefficient, N is the number of vegetation stems per horizontal area, b_v is the average diameter of the individual stems, k is the wave number, h_v is the height of the vegetation that is submerged, and h is the water depth. To date, the formulation of *Mendez and Losada (2004)* has been widely applied and the vegetation parameters can be varied in space in the spectral version of this vegetation dissipation model.

Suzuki (2011) adapted Equation 2.5 such that the vertical structure of vegetation

can be taken into account (i.e., C_D, b_v and N can vary over intervals along the vertical). This is implemented in numerical wave models such as SWAN (phase-averaged model) *(Suzuki, 2011)*. For other wave models, such as SWASH (phase-resolving model), the wave dissipation due to vegetation is based on the Morison equation as function of time and also requires the same geometric information of the trees as vegetation input (i.e., N and b_v).

The bulk drag coefficient is an important but uncertain parameter *(Kobayashi et al., 1993)*, as it generally accounts for neglected processes. For example, we usually assume rigid cylinders, thus neglecting vegetation motion, which influences the relative velocity. Obviously, this becomes less valid for relatively flexible vegetation and can influence the wave attenuation by these fields. Furthermore, simplifications of the vegetation geometry can also affect wave attenuation processes. Nevertheless, several studies reveal relations between the bulk drag coefficient and dimensionless hydraulic parameters, such as the Reynolds number, Re (e.g., *Hu et al., 2014*) and the Keulegan-Carpenter number, KC (e.g., *Jadhav et al., 2013*). Both Re and KC are predictors of the wake structures behind the vegetation *(Sumer and Fredsoe, 1998)*. KC is also a measure of the relative importance between drag and inertia. These studies generally show that C_D decreases with increasing KC and Re. In addition, other studies find better relations with non-dimensional parameters containing also vegetation characteristics such as the vegetation submergence ratio *(Mendez and Losada, 2004)* and the spacing between cylinders *(Suzuki, 2011)*. These relations make it possible to choose a value for the bulk drag coefficient accordingly. In the case of woody vegetation with enough space between branches without motion, one can expect the C_D values to be similar to that of rigid vertical cylinders, which holds a nearly constant value of $\approx$ 1.0 to 1.2 in the sub-critical flow regime ($10^3 \leq Re \leq 10^5$) (*Sumer and Fredsoe, 1998*; *van Wesenbeeck et al., 2022*).

2.2.2. Quantifying vegetation

Knowing the vegetation densities (N) and average diameters (b_v) in space is usually sufficient vegetation input for wave damping models for large enough Reynolds numbers, keeping in mind that the bulk drag coefficient can be used for calibration. An example of two rather simple representations of a pollard willow tree is shown in Figure 2.1. Unlike the simplified description in these wave damping models, the realistic branch structure of woody vegetation is difficult to capture by means of a single diameter and density. It is difficult to get accurate approximations of these values, especially for woody vegetation because these strongly vary in space. Furthermore,

the individual branches are also characterised by an angle (i.e., direction in which they grow) with respect to the incoming waves, which also complicates determining the 'projected' surface area. Alternatively, the frontal-surface area distribution of all the branches, $A_v(z) = b_v.N$, gives a better approximation of the entire tree structure. Hence, this research focusses on determining this parameter *(van Wesenbeeck et al., 2022)*.

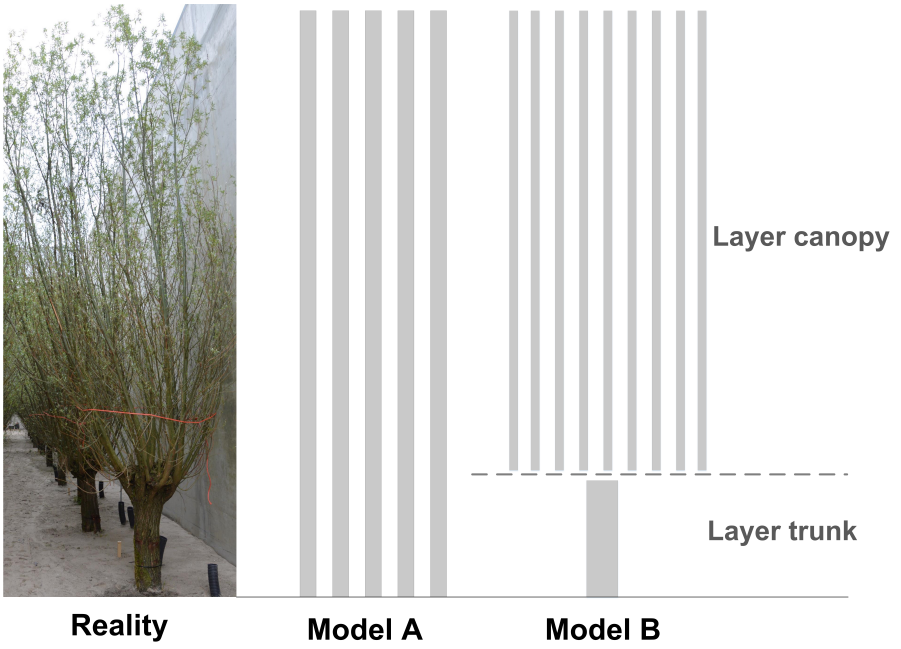

Figure 2.1.: Simple vegetation quantification. Two examples of schematizing a pollard willow tree, namely using a one-layered (Model A) or two-layered model (Model B).

Obtaining vegetation parameters can be done in different ways, namely: by conducting manual measurements or using remote sensing techniques (e.g., optical techniques and lidar, which can be spaceborn, aerborne, or terrestrial); each having its own advantages and disadvantages.

Manual measurements can be categorised into destructive (i.e., for biomass measurements) and non-destructive measures *(Nordh and Verwijst, 2004)*. The latter is a simple way of obtaining geometric information of trees and, accordingly, for calculating wave attenuation. For example, the density and diameters in a certain volume can be determined, after which a vertical and horizontal average value may be used.

This is generally seen as a valid way to quantify vegetation and has been used in several studies (e.g., *Jadhav et al., 2013*; *Ozeren et al., 2014*; *Möller et al., 2014*). Some studies indicate that the vertical variation of vegetation parameters is important to consider (e.g., *Ozeren et al., 2014*); and this vertical variation is already incorporated into numerical models *(Suzuki, 2011)*. Thus, a certain spatial resolution is needed depending on the vegetation type, and conducting hand measurements often becomes tedious.

Although solely hand measurements can be inefficient, we can still indirectly extent this data by using it as input for tree *allometric relations*. These are mainly formulations to obtain difficult tree parameters, such as tree height, through a relatively easy measured parameter such as the diameter at breast height. It is shown to work well for characterizing mangrove roots *(Ohira et al., 2013)*. A branching method, which also uses tree allometry, is developed by *Järvelä (2004)* to calculate the area of trees. This method stems from the *Strahlers ordering scheme*, originally applied on river systems and later on tree structures *(McMahon and Kronauer, 1976)*. This scheme starts at the smallest order ('finger-tip'), where two small bifurcations of the same order meet, they sum up to a higher order stream and so on, until it reaches the highest order stream (*Order=n*). Certain factors in between orders, also referred to as branching factors, are obtained and used to calculate the total area of a tree. These branching factors are mostly dependent on the tree species. For a detailed description on this branching method, we refer to *Järvelä (2004)*.

Lastly, remote sensing techniques can be used to obtain vegetation parameters. Spaceborne and airborne methods are effective for very large-scale measurements, for example identifying the state of the vegetation, but are less accurate for capturing vegetation parameters such as height and canopy structures *(Srinivasan et al., 2014)*. On a smaller scale, optical techniques are commonly used, and provide detailed information on the geometry (e.g., *Norris et al., 2017*; *Maza et al., 2019*). This method becomes more difficult and less accurate when dealing with larger objects, such as trees. For tree and forest scale applications, *Terrestrial laser scanning* (TLS) shows to be a good alternative. A comparison between TLS results and the branching method of *Järvelä (2004)* showed a good agreement in terms of total area of trees, which was afterwards used for determining the flow resistance during floods *(Antonarakis et al., 2009)*.

2.3. Methods

Section 2.3.1 describes the large-scale physical experiments, which includes the set-up and measurements of the forest and of the waves. Different methods for measuring and modelling the frontal-surface area in space result in different estimates for frontal-surface-area distributions over height, $Av(z)$. These methods are described in Section 2.3.2. Results of $Av(z)$, which can follow from combinations of measurements and *tree allometry* relations, are called *tree models* in this work. These tree models are used to determine the input required for the wave attenuation model, A_{veg}. Detailed data of the tree parameters and of the wave damping by these trees is used from large- scale physical experiments; hence, direct comparisons could be made between the measured wave attenuation and the calculated wave attenuation.

2.3.1. Physical experiments

Full-scale experiments were conducted on live pollard willow trees under storm conditions. These experiments were carried out in a 300-m-long, 5-m-wide and 9.5-m-deep wave flume, where significant wave heights (H_{m0}) up to 1.5 m were tested. A 40-m-wide forest was created with 32 pollard willow trees (*Salix Alba*) in front of a concrete levee. These trees formed 16 rows of 2, and were situated on a 85-m-long and 2.33-m-high platform. The platform represented a shallow foreshore, which permitted large wave height-water depth ratios to avoid having wave breaking inside the forest. A more detailed description of the experimental set-up is given in the paper of *van Wesenbeeck et al. (2022)*.

Experimental Setup: Forest

Manual Measurements

The pollard willow trees (*Salix Alba*) were 15 years old with three-year-old primary branches (i.e., branches that directly sprout from the knot of the tree). These primary branches were categorised into 3 classes (see Figure 2.2) based on the diameter at their base, D_B (i.e., diameter at the location above the knot), namely: class 1 ($D_B >$ 50 mm), class 2 ($20 < D_B \leq 50$ mm) and class 3 ($D_B \leq 20$ mm).

The main tree characteristics were manually measured prior to conducting test series 1 (full canopy with leaves). These include the following measurements:

- General tree characteristics:
  - Diameter and height of the trunk (D_{trunk}, H_{trunk})
  - Diameter and height of the knot (D_{knot}, H_{knot})

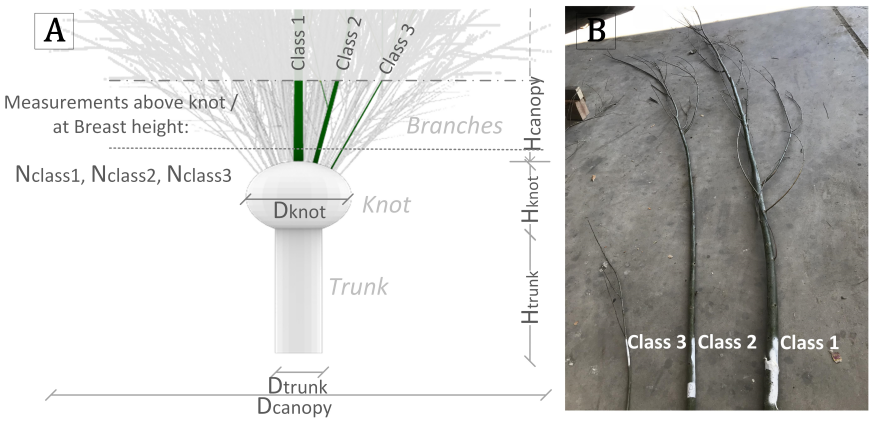

Figure 2.2.: **(A)** General tree characteristics of the pollard willow, **(B)** Examples of the 3 different diameter classes of branches

- The number of branches per diameter class (N_{class1}, N_{class2}, N_{class3})
- Diameter and height of the canopy (D_{canopy}, H_{canopy})

After the experiments, we took the following additional measurements:

- Characteristics of the primary branches:
  - The D_B with corresponding total branch length was measured in order to create an *allometric relation*. *Allometric relations* are commonly used to estimate tree parameters, which are challenging to measure (such as the branch length) from an easier measurable parameter (such as the diameter at breast height). A random sample size of 340 primary branches from the entire forest, which in total consists of 2,852 primary branches, was used.
  - Diameter decay relations were made for each branch class, since branches have a tapering form. This was achieved by measuring the diameter at increments of 1 metre along the main branch. A random sample size of 30 branches was used (10 branches per branch class).
  - Sketches of 9 branches were made. These sketches include the number, length and diameter of all the side branches; and they include the diameter of the main branch at vertical increments of 1 metre.
  - Additionally, strength and elasticity measurements were conducted on the primary branches; however, these are not analysed in the present work.

- Distribution of branch diameter and density over the vertical, by measuring an individual tree (i.e., this tree was from the same location as the tested trees, and contained shoots of the same age), named "*Tree S*":
  - The general tree characteristics were measured (H_{trunk}, D_{trunk}, H_{knot}, D_{knot}, N_{class1}, N_{class2}, N_{class3}, D_{canopy}, H_{canopy})
  - The number of branches and their diameters were measured at 1 metre vertical increments. This was eventually used to compute the density of the branches (N) and the average diameter (b_v) within each vertical interval.

Terrestrial Laser Scanning

In addition to taking manual measurements, we also used Terrestrial laser scanning (TLS). We scanned the forest prior and after each test series to monitor the state of the forest and to detect possible loss of tree biomass. These scans were taken with a FARO FOCUS 3D S 120 scanner from three fixed positions above the flume (Figure 2.5).

Experimental Setup: Wave Measurements

The tests (T001-T042) were carried out with different wave parameters and vegetation configurations. In total 5 test series (TS) were conducted, namely: TS 1 on the trunks of the trees for low hydrodynamic conditions (i.e., low water levels and wave heights), TS 2 on full canopies with leaves, TS 3 on full canopies without leaves, TS 4 on reduced canopy density without leaves, and TS 5 without willows (calibration tests). A more detailed description of the wave conditions is given in Appendix B: Table B.1.

The wave heights in front and behind the forest were measured with two types of wave gauge (i.e., radar wave gauge and resistance wave gauge). The wave damping due to the vegetation is expressed as the ratio between the incoming wave height and the wave height reduction (i.e., the difference in wave height between the tests with vegetation and the tests without vegetation), as applied in *van Wesenbeeck et al. (2022)*:

$$Dr = \frac{(H_{m0,no\,veg} - H_{m0,veg})}{H_{m0,in}}, \tag{2.6}$$

where Dr is the wave damping ratio by vegetation, $H_{m0,veg}$ and $H_{m0,no\,veg}$ are the measured wave heights with and without vegetation at the location behind the forest, and $H_{m0,in}$ is the measured incoming wave height in front of the forest.

2.3.2. Methods for quantifying A_v

Tree model 1 - Primary branch model

The first method considers the primary branches (i.e., main shoots) and their tapering form. Information of the branching structure and side branches is not included, therewith the contribution of the side branches (secondary and tertiary) to the total A_v is neglected. Allometric relations between D_B and the total length of the branches (Section 2.3.1), the total number of branches counted per tree, together with diameter decay relations of the primary branches were used to predict diameter and the total number of branches at vertical increments of 1 m. With this, the frontal-surface area is obtained at vertical increments of one metre for each tree. Hereby it is assumed that the primary branches are oriented perpendicular to the knot, with the largest branches located in the centre of the knot (see Appendix B Figure B.1).

Tree model 2 - Branching model (By example)

As in tree model 1 the side branches were neglected, a branching method similar to that of *Järvelä (2004)* is used to account for the side branches. We made some adjustments based on the measured properties of pollard willows. This method will be illustrated with an example on one tree, named "*Tree S*".

Firstly, the regular pollarding practice on these trees impacts the tree structure, namely with relatively thick knot and trunk with respect to its branches, deviating from the "natural" willow structure. Therefore, the branches are regarded separately from the trunk, applying the method to the primary branches (excluding the trunk). We first identified the initial parameters for each tree. These are given in Table 2.1 for tree S. Besides these parameters, we also defined the minimum diameter,d_{min} of 0.003 m and the height of the canopy, H_{canopy} of 3.4 m.

Table 2.1.: Initial parameters of the branches of tree S for the tree simulation.

	L_{high} (m)	D_B (m)	$N_{high}(-)$
Class 1 ($D_B > 50mm$)	2.52	0.053	3
Class 2 (20< $D_B \leq$ 50mm)	2.52	0.037	18
Class 3 ($D_B \leq$ 20mm)	0.82	0.01	59

Secondly, we used detailed sketches of the branches to obtain three branching factors. These branching factors show the number of side branches that a mother branch can support (R_B), the diameter ratio (R_D) and length ratios (R_L) between subsequent branch orders. These factors are defined as follows: $R_B = \frac{N_{b(m)}}{N_{b(m+i)}}$, $R_D = \frac{D_{(m+1)}}{D_m}$, and $R_L =$

$\frac{L_{(m+1)}}{L_m}$; where m is the child branch, (m+1) is the mother branch, N_b is the number of side branches, D is the diameter, and L is the length of the branch. The obtained branching factors differ per order (Table 2.2), thus we maintained distinct values per order instead of working with the average values and are assumed constant for all trees.

Table 2.2.: Impression of branching method and the resulting branching factors. These factors are defined as follows: R_B= $\frac{N_{b(m)}}{N_{b(m+i)}}$, R_D= $\frac{D_{(m+1)}}{D_m}$, and R_L= $\frac{L_{(m+1)}}{L_m}$; where m is the child branch, (m+1) is the mother branch, N_b is the number of side branches, D is the diameter, and L is the length of the branch.

Branching method impression	Branching factors

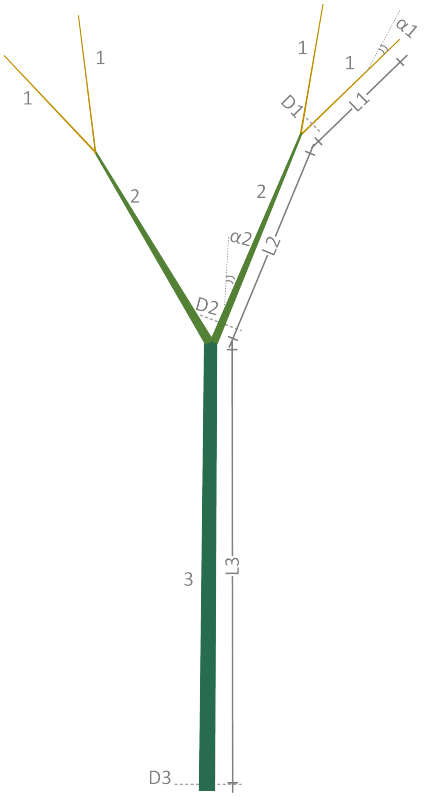

	1st to 2nd order	2nd to 3rd order
R_B	4.19 ($\frac{N_1}{N_2}$)	10.56 ($\frac{N_2}{N_3}$)
R_D	1.71 ($\frac{D_2}{D_1}$)	6.26 ($\frac{D_3}{D_2}$)
R_L	1.44 ($\frac{L_2}{L_1}$)	4.50 ($\frac{L_3}{L_2}$)

Thirdly, the frontal-surface area was determined by applying the branching factors from Table 2.2 on the initial parameters from Table 2.1 . The highest order branch is generally assigned to the trunk; however, in this work the primary branches are the

highest order (3rd order) as mentioned before. The steps to obtain the total frontal-area can be seen in Table 2.3. For example, the diameter factor, R_D, is applied on the highest order branch (i.e., the base diameter), D_3, until a diameter of the smallest order branch (d_1) is equal to the minimal diameter (d_{min}) of ≈ 0.003 m.

Fourthly, we applied a factor of 0.5 on the obtained frontal areas of Table 2.3 to account for the tapering form of the branches, as this is not accounted for in the initial method. Finally, we validated the branching method by applying it to the nine detailed sketches and on the measurements of the individual tree.

Table 2.3.: Frontal area calculation for all the branches of class 1 ($D_B \leq 50$ mm), class 2 (20 mm $< D_B <$ 50 mm), class 3 ($D_B \leq 20$ mm) of *tree S*. The values in bold represents the minimum diameter reached for each class.

Class 1				
Branch-order, m	N_B (units)	D (m)	L (m)	Frontal area (m^2)
3 (Primary branch)	3	0.0530	2.52	0.38
2	32	0.0080	0.56	0.14
1	133	**0.0047**	0.39	0.24
Frontal area, total				0.77

Class 2				
Branch-order, m	N_B (units)	D (m)	L (m)	Frontal area (m^2)
3 (Primary branch)	18	0.032	2.52	1.45
2	190	0.0051	0.56	0.54
1	796	**0.0047**	0.39	0.93
Frontal area, total				2.92

Class 3				
Branch-order, m	N_B (units)	D (m)	L (m)	Frontal area (m^2)
3 (Primary branch)	59	0.010	0.82	0.49
2	247	0.0059	0.57	0.83
1	1035	**0.0034**	0.40	1.42
Frontal area, total				2.75

The method by *Järvelä (2004)* solely computes the *total* surface area of the tree; moreover, it lacks information of the vertical distribution (*Järvelä, 2004*; *Antonarakis et al., 2009*). The distribution cannot be determined from these methods, as no angles between the branches, no tapering of the diameters, and no positions are considered. To determine the height variation of the surface area, we simulated the random structure of individual branches based on the allometric relations described above.

The simulations allow for variations in the branch positions while still following the branching rules. This results in slightly different branches from each simulation, mimicking "real" trees. The tapering form of the branches is included in the simulation by assuming a linear-diameter decay along its length.

This tree model was validated as some tree parameters, such as the angles of the side branches, the start positions of the primary branches on the knot, and the start positions of the side branches on their mother branch, do not have constant values and their distributions are not known. Thus, we validated this tree model against the hand measurements done on a single pollard willow (Tree S), keeping in mind that from these hand measurements we could also obtain $\sum b_{v,i}$ at vertical increments of 1 m. The same step size (1 m) was used to calculate $\sum b_{v,i}$ from the structure as simulated with tree model 2. Furthermore, only diameters larger than 4 mm were considered, as this was the cut-off diameter applied in the hand measurements.

As mentioned above, the angles between the branches were not measured. Still, this may influence the value of $A_v(z)$. Hence, a range of angles between the side branches was simulated from 10° to 45° with 5° increments to determine the influence of the angles and to choose a suitable value. The outcome is shown in Figure 2.3. The angle between 1st and 2nd order branches, α_1=30°, and the angles between 2nd and 3rd order branches, α_2=25°. Finally, the frontal-surface area variation along the height, $A_v(z)$,

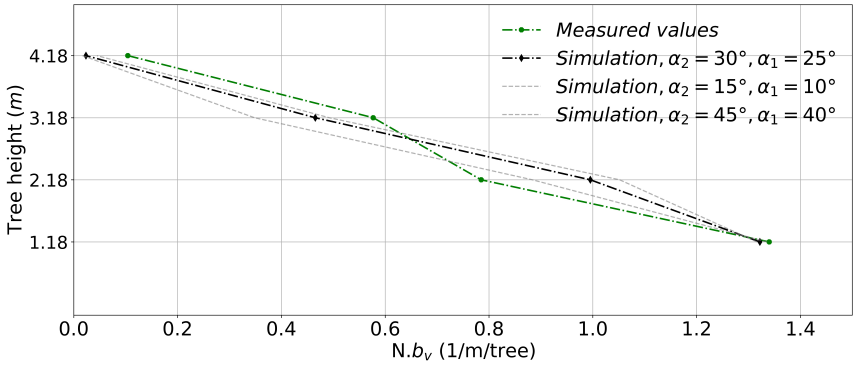

Figure 2.3.: Validation of tree simulations.

was calculated. This is defined as the projected surface area of the simulated branches perpendicular to the incoming waves (see Figure 2.4). Thus, these three-dimensional simulations take the branch angles, positions, and diameter decay into account.

$$\Delta A_v = \frac{1}{2} * \Delta s' * (D_{s,i} + D_{s,i+1}), \tag{2.7}$$

$$\alpha = \arccos \frac{dZ}{\sqrt{dX^2 + dY^2 + dZ^2}}$$

$$\omega = \arctan \frac{dX}{dZ}$$

$$\Delta s = \frac{\Delta z}{\cos \alpha}$$

$$\Delta s' = \frac{\Delta z}{\cos \omega}$$

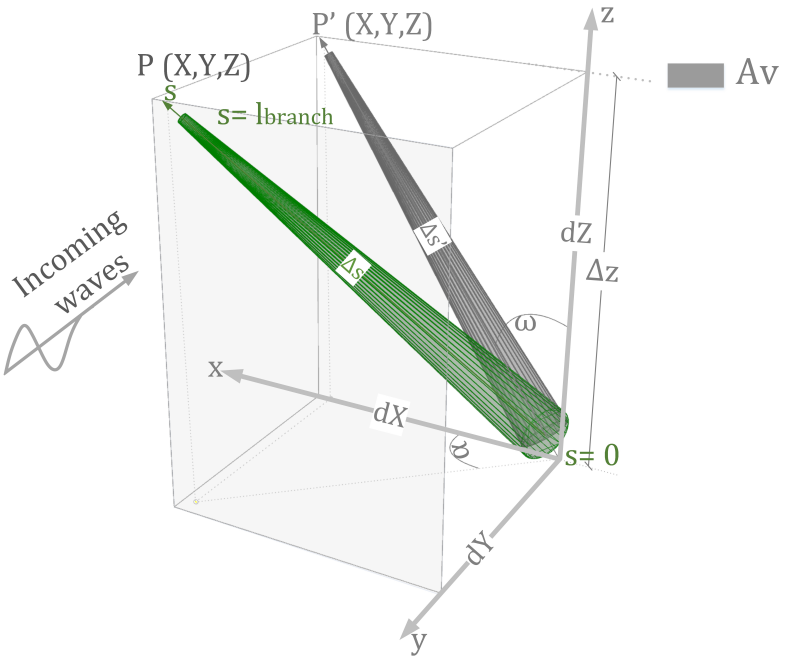

Figure 2.4.: Schematic of the coordinate system used for calculating A_v with the incoming waves from the positive y-direction. P is the endpoint of the branch, and P' is the projected branch perpendicular to the incoming waves.

Terrestrial laser scanning - post processing

Data from scans of the leafless condition of trees were used to obtain $A_v(z)$. This vegetation state coincides with the characteristics that we observe during extreme conditions, which are high hydraulic loads and leafless trees (winter season). Not to mention, scans during leaf-on conditions are less suitable to map the vegetation as

most of the laser beams are directly blocked in the outer layers of the tree by leaf density (see Figure 2.6) and leaves do not add significantly to the wave damping *(van Wesenbeeck et al., 2022)*. Figure 2.5 shows the entire forest without leaves and the 3 positions in the flume from which the TLS scans were created.

The post-processing of the point cloud data included sub-sampling, segmentation and filtering of the point cloud, performed in CloudCompare. Segmentation was done to remove excess information (e.g., measuring equipment, and flume walls) and sub-sampling was needed for the sake of work-ability of the point cloud. Afterwards, the point cloud data of each tree was analysed separately and the frontal area (i.e., does not include the angles of the branches relative to the incoming waves) was constructed using $alpha - shape\ function$, which is a built-in function in MATLAB. This function uses an *alpha parameter* to control how it creates the bounding region around the 3D-point cloud. An alpha shape value of 0.01 is used in this study, shown in Figure 2.6.

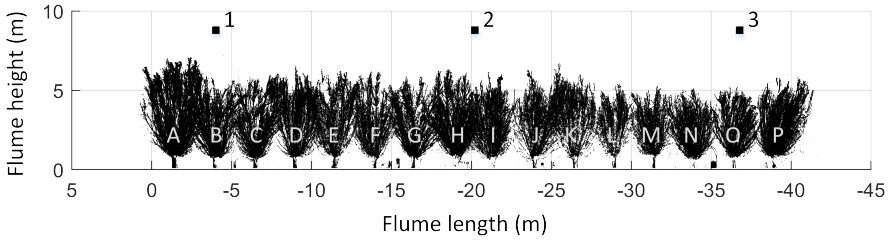

Figure 2.5.: Side view of the 3D-point cloud of the entire forest without leaves. The tree names (A-P) and the laser scanner positions (1-3) are illustrated.

2.3.3. Simulating Wave Attenuation and Bulk Drag Coefficients

The Morison equation is solely suitable for determining the drag forces on slender objects (neglecting diffraction of waves around the object), but can be used for predicting drag forces on trees as well. In this study, the forest is characterised by low canopy densities of around 13 branches per m^2. The average spacing, ΔS becomes $28d$, with d = 10 mm as the average branch diameter. The density parameter as described in *Nepf (1999)*, $ad = d^2/\Delta S^2$, is approximately 0.001, indicating a relatively sparse forest; hence, we can assume no porosity effects (i.e., blockage and sheltering). Thus, the drag coefficient can be considered similar to that of a single cylinder *(Etminan et al., 2019)*. In addition, the ratio between the wave length and the diameter is small, following the characteristic of slender objects.

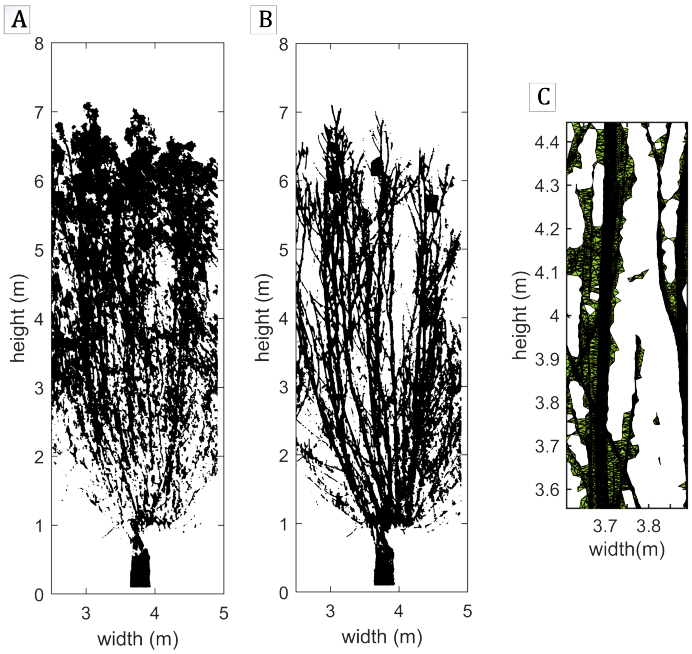

Figure 2.6.: **(A)** Tree A1 with leaves, **(B)** Tree A1 without leaves, **(C)** Surface area by alpha shape function (α_{shape}=0.01).

SWAN in 1D-mode is used in this study to simulate the waves through the forest. The SWAN model was defined in Cartesian coordinates with a spatial discretization of 1 metre. The model is forced with identical JONSWAP spectra to those measured at the deep water locations in the experiments (WHM01-03). SWAN was executed without accounting for wind growth, white capping, refraction, diffraction, quadruplets, triads, and turbulence dissipation, as these processes are not relevant in this flume experiment. On the other hand, frequency shifting in frequency space, bottom friction with a roughness constant of 0.07 $m^2 s^{-3}$, wave breaking , and vegetation dissipation were activated. The wave energy dissipation through vegetation fields accounts for the vertical structure of the vegetation and follows the action balance formulation, as shown in *Suzuki (2011)*. Following the same manner, the energy dissipation by vegetation becomes:

$$\langle \varepsilon_v \rangle = \sum_{i=1:I} \frac{1}{2\sqrt{\pi}} \rho_w \widetilde{C}_D \left(\frac{gk}{2\sigma} \right)^3 A_{veg,i} \frac{(\sinh^3 k\alpha_i h - \sinh^3 k\alpha_{i-1} h) + 3(\sinh k\alpha_i h - \sinh k\alpha_{i-1} h)}{3k \cosh kh^3} {H_s}^3, \tag{2.8}$$

where $\langle \varepsilon_v \rangle$ is the averaged wave energy dissipation due to vegetation; $\widetilde{C_D}$ the bulk

drag coefficient, g the gravitational acceleration constant; k the mean wave number; α_i the ratio between the depth at the top of the vertical layer i and the total water depth ($\alpha_i \leq 1$), where i = 1 represents the lowest vertical layer and i = I the highest vertical layer; h the water depth; $H_{s,in}$ the significant wave height; and $A_{veg,i}$ the total frontal width of vegetation perpendicular to the waves for layer i per unit area. Varying this vegetation parameter $A_{veg,i}$, according to the different tree models, will result in different wave attenuation outcome.

The bulk drag coefficient, $\widetilde{C_D}$, is important for predictive wave models and is therefore often estimated in studies on vegetation (e.g., *Suzuki, 2011*; *Maza et al., 2015*). In this work, the SWAN model is tuned with the measurements such that the modelled wave damping corresponds to the measured wave damping behind the forest. To achieve this, the tuning parameter, namely the bulk drag coefficient, is calibrated using exhaustive search. We made a distinction between the drag coefficient of the canopy ($C_{D,can}$) and the trunk ($C_{D,tr}$) for the tests with high water levels. For these high water level tests, the drag coefficient of the trunk is set to a constant value of 1.2 *(Wieselsberger, 1921)*. The SWAN set-up is made following the same approach as described in *van Wesenbeeck et al. (2022)*. This is repeated for different vegetation input [i.e., $A_v(z)$] from the tree models and TLS results.

2.4. Results

This section shows the general characteristics of the 32 pollard willow trees (Section 2.4.1), and the characteristics of the resulting tree models (Section 2.4.2). We analysed the frontal-surface area, $A_v(z)$ of each tree model, and afterwards we calculated the corresponding wave attenuation and compared these results. In addition, the relation between Keulegan- Carpenter number (KC) and drag coefficient (CD) for each tree model is presented (Section 2.4.5). This provides us more insight into the errors of different tree models and their effects on predicting wave attenuation.

2.4.1. General characteristics of pollard willows

From the manual measurements it follows that the smaller primary branches (Class 3) take up a large portion of the total number of branches in a pollard willow tree (64%), while the larger primary branches (Class 1) only account for 3% of the total number of shoots. Therefore, a larger data set could be obtained for the smaller branches. The fraction of each diameter class is given in Figure 2.7A with corresponding 95%-confidence interval. Furthermore, the gathered data of the D_B is plotted in Figure

2.7B, which includes for the average value and the 95%- confidence interval.

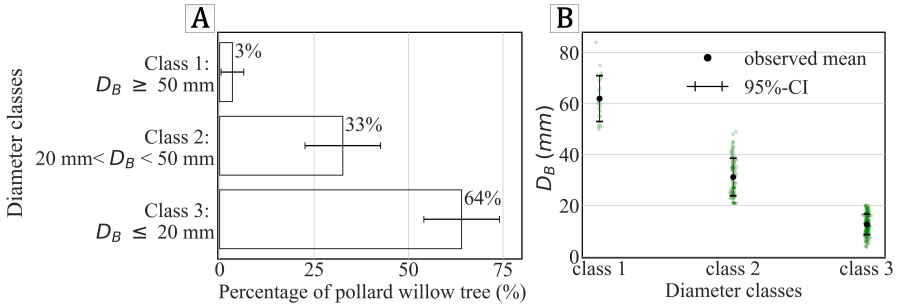

Figure 2.7.: **(A)** Distribution of diameter classes for a pollard willow tree, **(B)** Diameter range found for each class

Other tree parameters such as the D_b, N_{high} and L_{high}, are given in Appendix B Table B.2.

2.4.2. Tree model Results

Tree model 1: Primary branches

Solely considering the primary branches of pollard willow trees is a relatively simple way of mapping the vegetation. Besides this, relatively less wave attenuation is expected from the smaller side-branches as these are more flexible than the primary branches. The manual measurements done at breast height (i.e., the number of branches per class), the allometric relation between D_B and branch length, and the diameter-decay relations were the main input for this tree model. We assumed an average diameter at breast height for each class (see Figure 2.7B). The D_B-length relation, diameter-decay relation, and a simplification of the tree without side-branches (tree model 1), are shown in Figure 2.8. This model is considered as the lower limit of the frontal-surface area as it only accounts for the main branches (neglecting the side branches). It was initially expected to give a reasonable estimate of the total A_v; on the contrary, the comparison to the other tree model that follows hereafter shows that this is not the case.

Tree model 2: Branching method

The branching method uses RNG to describe the branch structure for all branches larger than $\approx$ 3 mm, which is used to create tree model 2. To statistically estimate the $A_v(z)$, trees were simulated in Python to generate random branches that follow

the branching rules shown in Table 2.2. The parameters from Appendix B Table B.2 are input for generating the branches. An example of a generated branch from each class is shown in Figure 2.9A. Figure 2.9B illustrates tree model 2, which is formed by these generated branches positioned on the knot. In Figure 3.3A the $A_v(z)$ as sampled from the generated trees is shown. As each realisation yields a different $A_v(z)$, the output is a distribution for which the mean and the 95% confidence interval are determined.

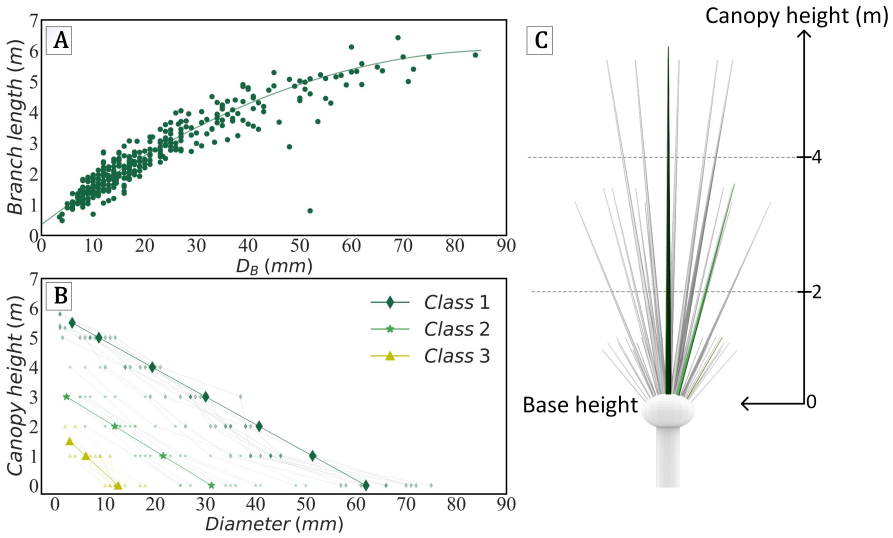

Figure 2.8.: **(A)** The relation between the diameter at the base of the knot (D_B) and the branch length for 340 branches (containing all classes), **(B)** The diameter decay along the length of the branch for 10 branches of each class (class 1, 2, and 3), **(C)** Impression of tree model 1 (i.e., only accounting for main branches).

2.4.3. TLS correction factor

The comparison of A_v (Figure 3.3B) showed an overall underestimation by the TLS results. Though, the TLS showed an overestimation in the upper layers of the trees. This suggests that *occlusion* due to the canopy density is the main reason for the observed errors in the lower canopy layers. A correction factor was applied on one tree at the edge of the forest to improve the TLS results by accounting for the percentage of blocked laser beams.

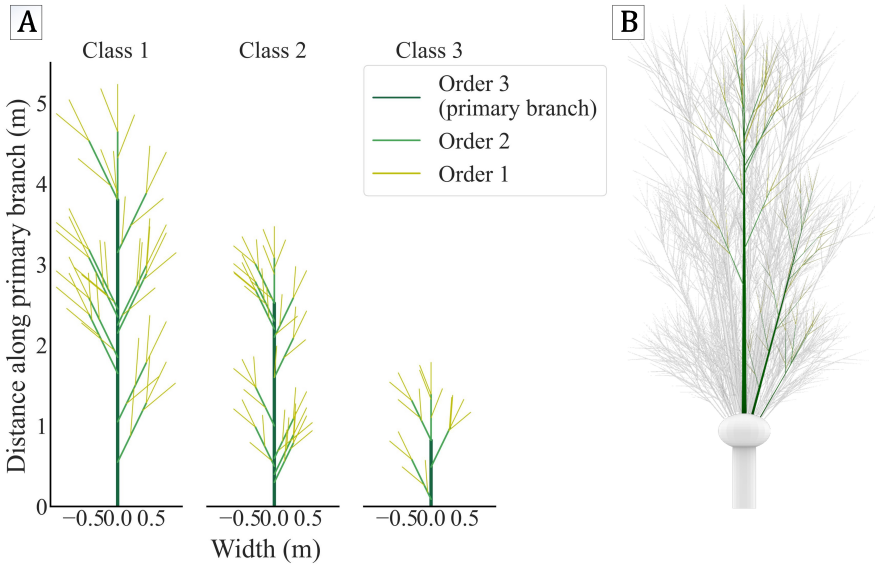

Figure 2.9.: **(A)** An example of 3 simulated branch classes, **(B)** Impression of one simulated tree which consists of a trunk, a knot and multiple branches of each class.

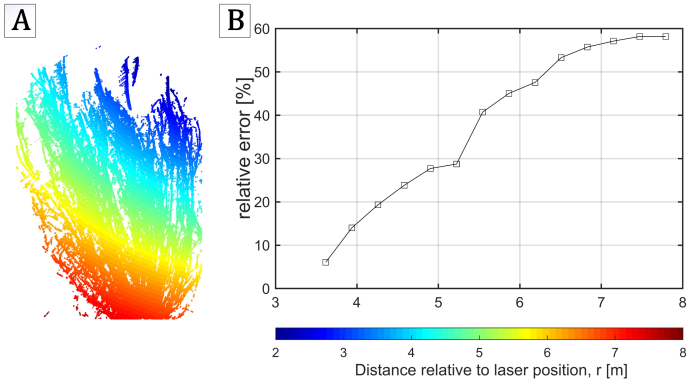

Figure 2.10.: **(A)** Tree P1 with, **(B)** corresponding graph containing the relative error of the laser scanner as function of the penetration distance of the beam, r. The colors and the horizontal axis indicate the distance from the laser scanner.

$$A_{TLS,new,n} = A_{TLS,n} * f_{cor,n}, \tag{2.9}$$

$$f_{cor,n} = \frac{N_{l,t}}{N_{l,t} - \sum_{i=n+1}^{i=m} N_l}, \tag{2.10}$$

where $A_{TLS,n}$ is the area obtained from the 3D-point cloud in layer n, f_{cor} is a correction factor based on the number of blocked laser beams, $N_{l,t}$ is the total amount of laser points send out by the laser scanner, and N_l is the number of laser points blocked in the layer before reaching layer n. The correction increased the $A_{v,tot}$ with 2.45 m^2. However, this correction could only be applied to trees near the laser scanner positions as occlusion by neighboring trees could be neglected. We applied this to tree P1 as this tree is also most likely not hit by laser beams other than the laser scanner nearest to it (see Figure 2.10).

2.4.4. Comparing Frontal-surface Area

The three different tree models are first compared considering their frontal-surface area distributions, shown in Figure 3.3B. All the tree models are set to a similar resolution (i.e., namely at vertical increments of 1 m) of the results to get a more clear comparison between the models. It shows that side branches amount to at least $\approx$ 25% more $A_{v,tot}$ than only the primary branches. Furthermore, the TLS results underestimate the canopies total frontal-surface area compared to the other tree models. The underestimation by the TLS is mainly seen in the lower layers of the trees, while in the upper layers there is an overestimation.

2.4.5. Comparing Wave Attenuation

A strong relation is found between $\widetilde{C_D}$ and the Keulegan- Carpenter number (KC). The KC number is usually calculated as follows: $KC = \frac{U \times T}{L}$, where U is the orbital velocity, T is the wave period, and L is the average diameter of the object. For determining KC, we chose the maximum horizontal orbital velocity based on linear waves U_{0max}, and T_{m02} as a representative wave period of the wave spectrum. The definition of KC is non-trivial for realistic tree structures, as these structures are characterised by a distribution of branch diameters that varies over the height. The KC number in this work is calculated at vertical increments of 1 m and averaged over the height.
The results show a decrease of $\widetilde{C}_D$ with increasing KC numbers (Figure 2.12). Furthermore, the differences in $\widetilde{C}_D$ between the tree models are a consequence of different frontal-surface area distributions. Tree model 1, which is considered as the

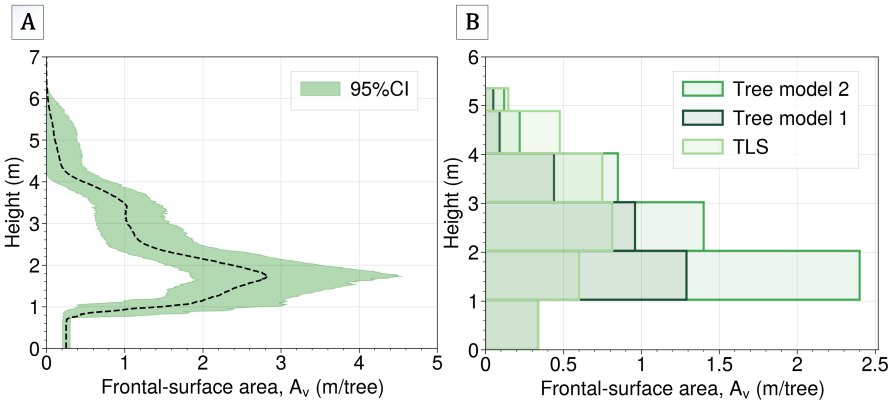

Figure 2.11.: **(A)** The average frontal-surface area (A_v) of the 32 trees in the large-scale experiments with 95% confidence interval using tree model 2, **(B)** Frontal-surface area comparison of the tree models, considering the average tree without leaves in the wave flume.

lower limit for the frontal-surface area, shows larger $\widetilde{C_D}$ values relative to tree model 2, due to its lesser frontal-surface area. The largest $\widetilde{C_D}$ values are observed for tree model 3. This is according to expectation, since the TLS method underpredicts the frontal-surface area of the trees (Section 2.4.4).

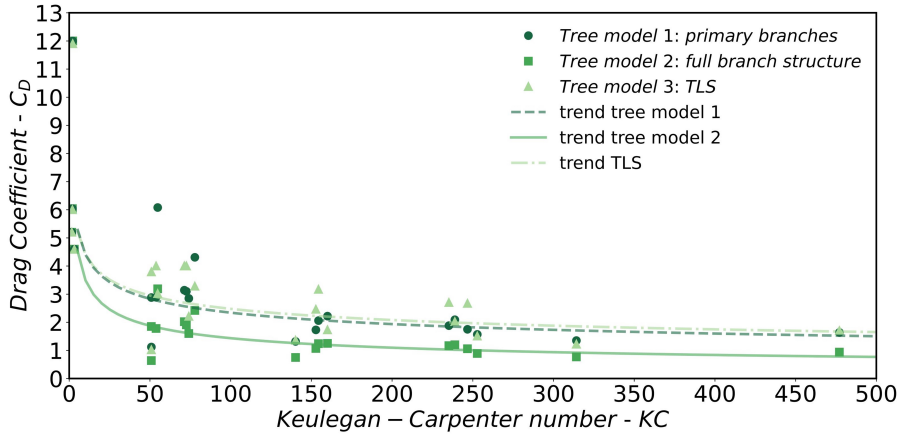

Figure 2.12.: Relation between C_D and KC for tree model 1 (only the Primary branches), tree model 2 (primary branches including the side branches), and tree model 3 (TLS measurements).

2.5. Discussion and Conclusion

Globally, considerable claims are made of how trees, such as mangroves and fresh water trees, reduce impact of waves during extreme storms and tsunamis *(EJF, 2006)*. Most research on wave attenuation by vegetation focused on investigating hydrodynamics around the vegetation structure, whereas less attention is given to vegetation parameters and methods to quantify these structures (e.g., *Huang et al., 2011*; *Wu and Cox, 2015*). Vegetation, such as in salt marshes, is generally quantified in a simplified manner using a spatial average diameter (b_v) and density (N). For example, studies on mangrove forests used similar approaches, where single values for the density and diameter were used to represent the entire structure (e.g., *Phan et al., 2019*) or used single values per layer to represent the roots, trunk and canopy separately (e.g., *Vo-Luong and Massel, 2008*; *Narayan et al., 2011*; *Ismail et al., 2012*). More thorough quantification of especially complex canopies seems to be lacking, but is needed to obtain insight in processes that determine wave attenuation during extremes accurately. For woody vegetation (e.g., willows and mangroves) the frontal-surface area parameter, $A_v(z)$ is an useful way of quantifying this. Some studies have described vegetation using similar parameters concerning the tree frontal area (e.g., *Maza et al., 2017a*; *Maza et al., 2019*). However, these solely considered damping through roots and trunks, neglecting the canopy.

Previously, large-scale experiments were conducted on a well-defined 40-m-long willow forest (*Salix Alba*) for which wave attenuation during storm conditions was determined *(van Wesenbeeck et al., 2022)*, showing that most of the wave damping occurred at mid-water levels through the canopies of the trees. This is where most of the biomass and surface-frontal area was present; hence, improving our estimates of the entire vegetation structure and developing methods to quantify this will improve the predictability of wave attenuation by vegetation for different water levels and wave heights. We used these large-scale experiments to obtain more insight in methods to extract $A_v(z)$ of the trees, using both manual measurements and terrestrial laser scanning (TLS). Manual measurements executed on all the branches at vertical increments of 1 m, are relatively simple measurements, but tedious to perform on every tree. The accuracy of these measurements depends on the size of the vertical increments (i.e., layer thickness). With this, the diameter decay along the vertical is taken into account to a certain extent. However, the angles of the branches are neglected and side branches that are within the layers are also neglected.

Using simple manual measurements as input for allometric relations for trees is an efficient way to include side branches. Based on this, a three-dimensional tree

model is created (included positions and angles of the branches), which was used to determine the frontal-surface area distribution in the vertical, $A_v(z)$. For this method, it is important to note that the initial tree parameters and branching factors used in this research are applicable to "pollard" willows with 3-year-old shoots (*Salix Alba*); these values are likely to differ for "natural" willows of the same species. The simulations from this method can nevertheless be used to obtain a more thorough representation of the trees for numerical and physical models.
The side branches are relatively flexible branches, leading to more extreme branch motion. This in turn can lower the significance that these small branches may have on attenuating waves. On the other hand, it was found that the side branches could take up to 25% of the total frontal-surface area of these trees. Thus, including these branches in tree models may be necessary for wave attenuation predictions.

A more efficient method for assessing $A_v(z)$ could be through TLS measurements. The TLS is a practical method to conduct measurements on a forest scale and has the potential to be combined with satellite data to provide useful parameters for wave damping models. However, the results of the TLS depend on the post-processing and in our case, the chosen α_{shape}- value. We showed that the TLS underestimates the frontal-surface area, especially near the trunk region, where branch densities are largest, which is mainly due to shadowing effects. However, this can be corrected by applying a factor that accounts for the shadowing phenomenon (blockage of the laser beams by high branch densities). These findings encourage further research on the TLS as it is a promising measurement technique for mapping large heterogeneous forests in the field. For this, it is recommended to position the TLS in the direction of the incoming waves to investigate the blockage factor in more depth.

Furthermore, a decrease in bulk drag coefficient with increasing Keulegan-Carpenter number (KC) was shown, which is a trend found also in other vegetation studies (e.g., *Anderson et al., 2011*; *Ozeren et al., 2014*; *Etminan et al., 2019*). The numerical model validation showed large differences in wave attenuation for different tree models and a corresponding large range in bulk drag coefficients, especially for lower KC numbers. This suggests that the discrepancies between the tree models in terms of frontal-surface area are significant for wave attenuation. A range of C_D between 0.94 and 1.70 was obtained for high KC numbers, emphasising the importance of reliable frontal-surface area distributions.

Thus, having feasible methods to obtain reliable frontal-surface area of vegetation fields is relevant for reliable wave predictions. This will increase the potential of implementing hybrid flood defences, existing of coastal or riparian vegetation and

engineered structures, such as embankments or levees. Only a combination of more accurate measurements on vegetation, data and modelling can be used to systematically obtain more insight in what vegetation can actually contribute to flood risk reduction during average and more extreme conditions.

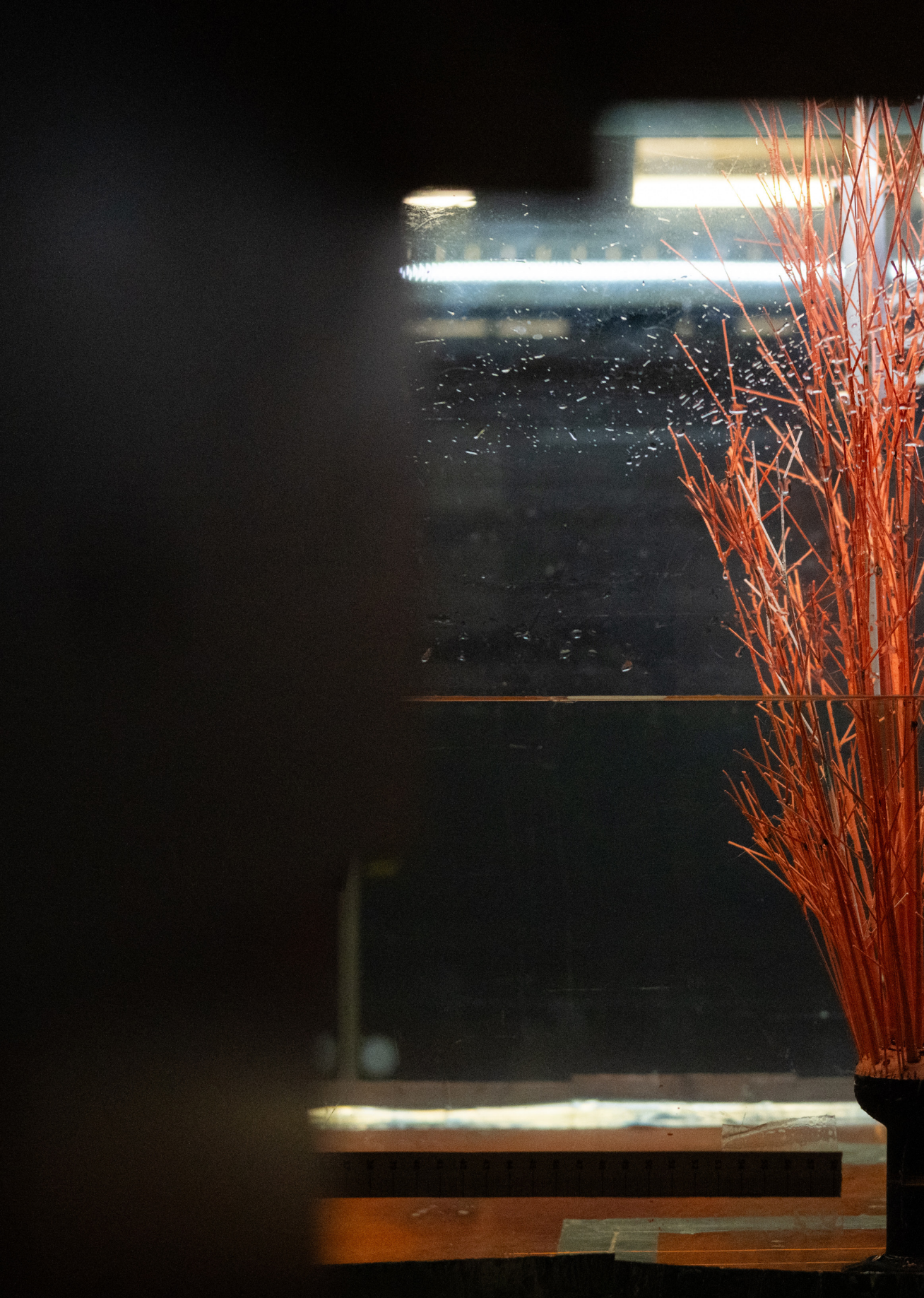

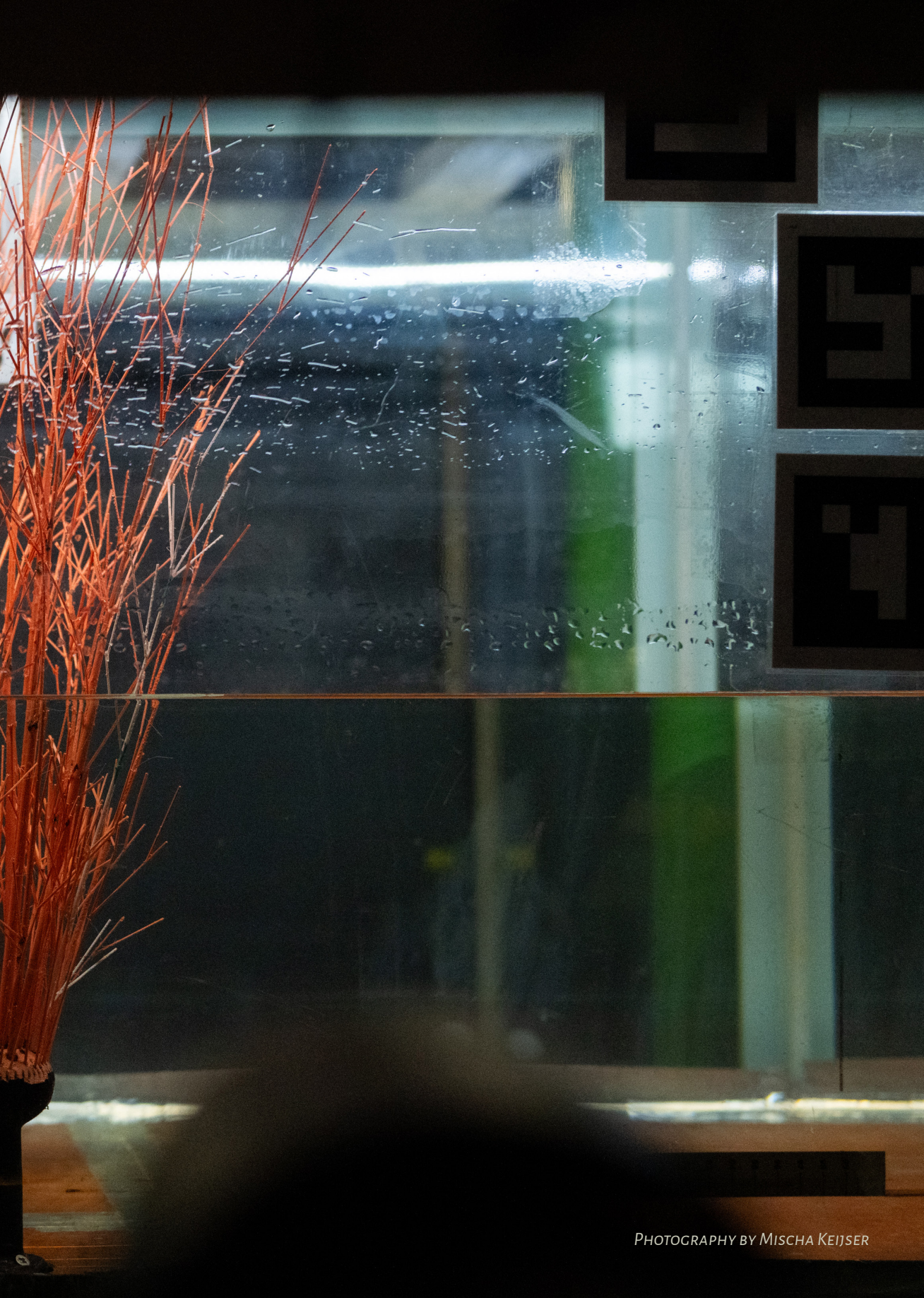

Photography by Mischa Keijser

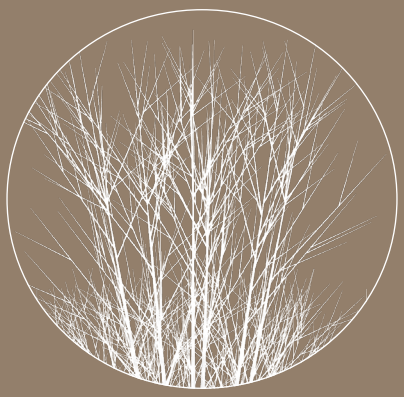

3

Possible Scale and Model Errors

This Chapter has been published in *Ecological Engineering* as:

Kalloe, S.A., Hofland, B. & van Wesenbeeck, B. K. (2024). Scaled versus real-scale tests: Identifying scale and model errors in wave damping through woody vegetation. *Ecological Engineering*, 202(November), 107241. https://doi.org/10.1016/j.ecoleng.2024.107241

3.1. Introduction

Nature-based flood defences, specifically vegetation in front of dikes, can increase the safety against flooding while providing many other ecosystem services (such as storing carbon, sheltering habitat and trapping sediment) *(Riis et al., 2020)*. Over the last decades these solutions are increasing in popularity in the face of climate change *(IPCC, 2022)*. Nonetheless, implementation of these solutions remains a challenge as design guidelines are missing. One of the reasons is that many wave damping predictions are based on data from scaled flume tests or field experiments that cover only mild wave conditions. Validation of these predictions is still scarce, which leads to uncertainties in the design of these hybrid flood defences *(Vuik, 2019)*. To correct for scale errors in scaled experiments, we need validation under storm conditions, especially compared to similar scaled tests.

There are few measurements covering extreme hydraulic conditions at large-scale (e.g., *Möller et al., 2014*) and in the field (e.g, *Vuik, 2019*). However, the link between realistic scale and scaled tests is missing. Measuring extreme conditions during field campaigns is difficult as these events do not occur often, are not in a controlled and repeatable setting, and pose difficulties with measuring equipment. As a result, most field campaigns are conducted during mild wave climate (such as *Phuoc and Massel, 2006*; *Quartel et al., 2007*; *Bao, 2011*; *Norris et al., 2017*) and only few studies cover extreme weather (such as *Infantes et al., 2012*; *Vuik, 2019*), mainly on sea-grasses and salt marshes. Large-scale testing facilities with controlled conditions can be used to test vegetation-wave interactions on realistic scales. However, conducting full-scale (scale 1:1) and large-scale (i.e., up to 1:4 scale *(National Research Council (U.S.), 1999)*) experiments are relatively costly and time consuming, making experiments at reduced scales with vegetation mimics attractive. Hence, scaled flume experiments have been conducted frequently in the past to investigate wave propagation through live grassy vegetation (*Ozeren et al., 2014*; *Maza et al., 2015*) or with mimics representing woody vegetation, such as mangroves (*Ismail et al., 2012*; *Hu et al., 2014*; *Maza et al., 2019*). However, down-scaling experiments can lead to discrepancies with findings at full scale. The deviations between scaled models and their prototype can generally be contributed to three main sources: model effects, measurement effects, and scale effects *(Heller, 2011)*. Firstly, model effects occur when prototype features cannot be captured well enough in a modelling facility, such as material properties and boundary conditions. Secondly, the specific characteristics of a measuring technique may result in measurement effects. Thirdly, the relevant *force-ratios* between the prototype and its scaled model may deviate, which can lead to scale ef-

fects. Differences in the formulation of vortices is one example of these scale effects. These deviations are likely to resonate in numerical models with inherent errors.
In this manuscript, we compare wave damping results from scaled tests with real-scale tests to obtain insight in possible scaling errors in scaled flume tests. For this, we use real-scale experiments with woody vegetation, specifically live willow trees *(van Wesenbeeck et al., 2022)*, to design the set-up of scaled experiments with 3D-printed trees. The latter scaled experiments (scale 1:10) mimic the full-scale experiments in terms of hydraulic conditions, location of the equipment, and consider the geometry and flexibility of the trees. With the results, a first assessment of possible correction for wave damping through woody vegetation when using scaled tests is made. This will make scaled experiments more reliable and may lessen the need for expensive large-scale experiments in the future. Most importantly, current wave-predictions can be made more reliable with knowledge on these scale errors.

3.2. Methods

3.2.1. Experimental Setup

The prototype tests were conducted in a 291×5×9.5 (l×w×h) m^3 wave flume, of which 200 m of the total length was used for the experiments. A detailed description of these tests can be found in *van Wesenbeeck et al. (2022)*. We used a 1:10 scale model (n_L=10) ; this was the largest scaled model that could fit in the available flume (i.e., l×w×h = 40×0.8×1 m^3). A segment of this wave flume was used for these tests to replicate the geometry of the prototype section. For this, a divider made of wood was used to reduce the width of the flume to 0.5 m and a dike construction was built with two slightly different slopes (namely, a composite 1:3.6 upper and 1:3 lower slope) mimicking the dike slopes of the real-scale tests. This dike was placed such that the desired flume length of 20 m was obtained. The scaled experimental set-up is shown in Figure 3.1. Wave gauges (WG1-10) and one video camera from the side of the flume (camera 1: *SONY Handycam* 25 fps) were mainly used for analysis in this manuscript.

3.2.2. Scaling

Scale errors increase with the scale factor (n_L), which is the ratio between the characteristic length in real-world scale (L_p) and in model scale (L_m) *(Heller, 2011)*. To avoid scale effects, scaled models require the following similarities with their prototype: geometric similarity, kinematic similarity, and dynamic similarity *(Hughes,*

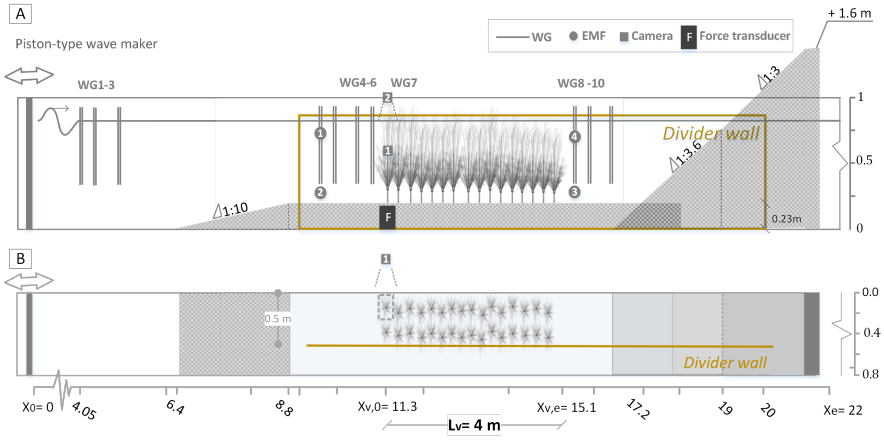

Figure 3.1.: The set-up of the 1:10 scaled tests **(A)** shows a side-view of the set-up, where the wave gauges (WG), electromagnetic flow meters (EMF), two cameras, and force transducer (F) are shown along the flume; **(B)** shows a top view of the set-up, where the two rows of the trees and the divider wall can be seen. The geometry of real-scale test setup was 10 times larger.

1993). For dynamic similarity, the most relevant ratios controlling the investigated phenomenon should be selected and ideally kept constant to the prototype values.
For models of free-surface flows Froude similarity, is typically used, ensuring that most wave-related phenomena are well reproduced, calculated as follows $Fr = \frac{U}{\sqrt{(gh)}}$ with the velocity (U), gravitational constant (g), and the water depth (h). The Reynolds number ($Re = \frac{UD}{\nu}$, where ν is the kinematic viscosity of the fluid and D is a representative diameter), which represents the ratio of inertial force to viscous force, is typically reduced at smaller scale. If Re is larger than a certain threshold, forces that flow around objects separate and the forces on these objects (governed by inertial pressures) will generally follow Froude scaling *(Heller, 2017)*. The tested hydrodynamic conditions were therefore scaled following Fr similitude.
If the motion of (branches of) vegetation is important, the Cauchy number also becomes important (*Luhar and Nepf, 2016*; *Cavallaro et al., 2018*; *van Veelen et al., 2020*). This is related to the elastic force, with Cauchy being a reliable representative number:

$$Ca = \frac{\rho_w U^2 D l^3}{EI},$$

where ρ_w= density of water; U= velocity; D= representative diameter of the object; l= object's length; E= Young's modulus; I= second moment of area. We scaled flexibility using the Cauchy number, implying that the material of the branches is chosen such that the Young's modulus of the model, E_m, equals $1/10$ ($1/n_l$) times the Young's modulus of the prototype, E_p. The E_p was assumed to be within a range of 3800 - 4500 *(Armanini et al., 2005)*. We selected a material within this range, namely Soft-Flexible PLA, with a Young's modulus of 390 MPa.
Scaling based on Fr automatically leads to the correct scaling of certain non-dimensional numbers such as the Keulegan-carpenter number (KC= $\frac{UT}{D}$, representing the ratio of drag-to-inertia force *(Keulegan and Carpenter, 1958)*). However, other relevant ratios may deviate from prototype scale, such as the Reynolds number (Re) as we considered Fr similitude and kept the fluid identical between the model and prototype.

3.2.3. Design of Tree Mimics

We focused on vegetation tests excluding the leaves, as leaves were found to have an insignificant effect ($\leq 4\%$) on the amount of wave damping while having a relatively large frontal-surface area compared to the branches *(van Wesenbeeck et al., 2022)*. The tests included represent two vegetation configurations, namely: trees with 100% canopy density, and 50% canopy density (i.e., where 50% of the branches of each tree were removed).
Tree mimics were made considering a 1:10 geometric scale of the real size trees and including surface areas for different branch orders taken from Chapter 2. The primary branches, which are the main branches that sprout from the tree knot, were categorised into three classes based on manual measurements of the diameter at the knot (i.e., base diameter, D_B). The canopy from the tree simulations in Chapter 2 consisted of these three branch classes, namely: class 1 (Db>50 mm), class 2 (20<D_B≤50 mm), and class 3 (D_B≤20 mm). Furthermore, these classes are built up from branch orders, starting at the tip of the branches (*order* 1, the smallest branch) until the primary branch is reached at the knot (*order* 3). Figure 3.2 shows an example of three different branch classes; the simplified branches; and finally an impression of the entire tree, including one red-coloured medium branch (*class* 2), which was used to follow its movement. With the 3D printer, the minimum diameter that could be printed was 1 mm, while the smallest order branches had a diameter of 0.3 mm. Hence, we decided to have less smallest order branches to still achieve a frontal-surface area distribution over the vertical, which was similar to the live trees (see Figure 3.3). However, geometric deviations between the two scales are inevitable

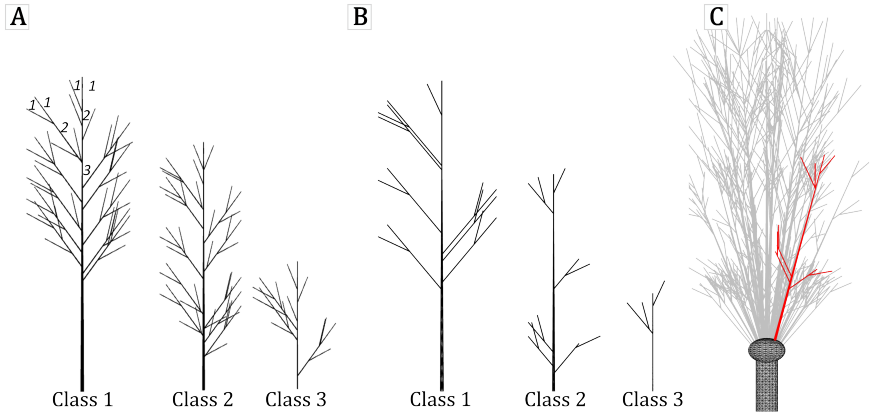

Figure 3.2.: **(A)** A 2D example of the 3 branch classes used to create a tree model of the live trees; and an example of how a branch (i.e., class 1) is built-up from different branch orders (order 1, 2, and 3), **(B)** simplified branch classes for the 3D-printed mimics, **(C)** example of an entire tree, where one medium branch was coloured (red) for tracking the branch motion.

using mimics. For more details on how these mimics were built, we refer to *Kalloe et al. (2022b)*.

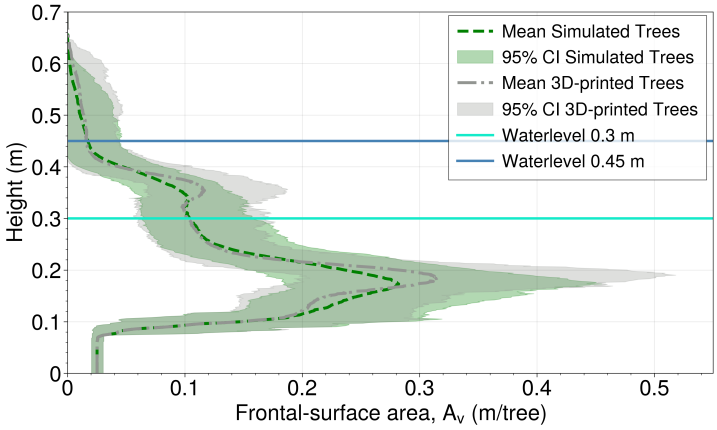

Figure 3.3.: The calculated frontal-surface area profiles of the simulated (from Chapter 2) and 3D-printed trees with the two tested water levels indicated, namely 0.3 and 0.45 m.

3.2.4. Forest Characteristics

The trees were placed in two rows of 16 trees each; an identical configuration to the real-scale experiments. The canopy densities and their distribution over the flume were kept largely the same as in the real-scale experiment. Each individual tree was generated with the same number of main branches of the three classes, while the exact configuration of the branch was randomly generated from allometric relations based on a real pollard willow tree (see Figure 3.2). The entire tree was 3D printed. The trunk and knot needed to be stiff, while the branches of the canopy were printed with flexible material (see Section 3.2.2). To attach the trees to the bed, a streamlined disk of 5 mm thickness was added to the lower part of the trunk. Figure 3.4 shows the live forest and printed mimics. The live branches that sprout from the knot's circumference have a slight curve. As the modelled branches were not curved as in reality, the divergence angle is somewhat smaller, leading to a higher density in the centre compared to the live canopies. This is not expected to influence the wave damping as the inter-branch distance is still large.

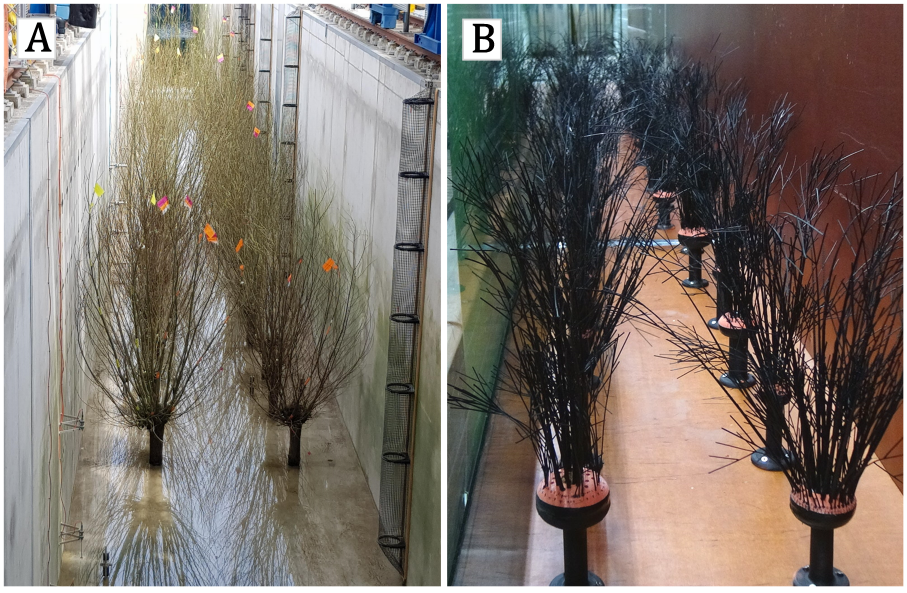

Figure 3.4.: (A) The real-scale experiments with the 50% density live trees, (B) the scaled experiments with 50% density 3D-printed trees (1:10 scale).

3.2.5. Experimental Conditions

The hydrodynamic conditions and the relevant dimensionless numbers (i.e., $\tilde{\mathrm{Re}}$, $\tilde{\mathrm{KC}}$ and $\tilde{\mathrm{Ca}}$) are compared at both scales in Table 3.1. This table shows the values for the largest branches (*class* 1 *order* 3), and the smallest branches (*order* 1).

Table 3.1.: An overview of the wave parameters (i.e., water depth at the forest h_f, significant wave height H_s, and peak wave period T_p) and dimensionless parameters (i.e., $\tilde{Re}$, $\tilde{KC}$ and $\tilde{Ca}$) for the largest (*Class* 1 *Order* 3, base diameter= 62 mm) and smallest branches (*Order* 1, diameter= 3 mm) of the real-scale (R001-R006) and scaled experiments (S001-S006).

	Test	h_f (m)	H_s (m)	T_p (s)	$\tilde{Re}_{large}$ $\times$ $10^3(-)$	$\tilde{Re}_{small}$ $\times$ $10^3(-)$	$\tilde{KC}_{large}$ $(-)$	$\tilde{KC}_{small}$ $(-)$	$\tilde{Ca}_{large}$ $(-)$	$\tilde{Ca}_{small}$ $(-)$
Real scale	R001	3	0.50	2.83	20.2	1.2	22	372	0.09	0.059
	R002	3	1.17	3.58	50.3	2.9	68	1160	0.59	0.345
	R003	3	0.50	4.00	21.9	1.3	32	563	0.11	0.065
	R004	3	1.01	5.66	46.2	2.6	96	1665	0.52	0.280
	R005	4.5	1.61	4.90	46.5	3.2	132	1767	4.28	0.425
	R006	4.5	1.52	6.93	46.8	3.2	181	2475	4.28	0.412
1:10 Scale	S001	0.3	0.05	0.9	0.7	0.1	21	112	0.09	0.0002
	S002	0.3	0.12	1.13	1.6	0.3	66	347	0.56	0.009
	S003	0.3	0.05	1.26	0.7	0.1	32	168	0.11	0.0002
	S004	0.3	0.10	1.79	1.5	0.3	94	499	0.49	0.008
	S005	0.45	0.16	1.55	1.6	0.3	122	530	3.51	0.011
	S006	0.45	0.15	2.19	1.6	0.3	169	742	3.51	0.011

Calculating the non-dimensional numbers (such as *Re* and *KC*) is not straightforward as a tree consists of different components with distinct characteristics (such as diameters and Young's modulus) and are subject to varying velocities. The trees were therefore separated into components, such as a knot, trunk, and different order branches. The non-dimensional numbers were determined for layers over the water column for these separate components. Figure 3.5 shows an example of how Re_i is calculated for a live pollard willow tree. This method shows that the main branches (*order* 3) of each class (*class* 1, 2 and 3) were divided into layers over the water depth because of the change in diameter and velocity values over the vertical axis. The diameter tapering of the main branches sprouting from the knot (*order* 3) was assumed

to be linear over the height. For this a minimum diameter (i.e., *order* 1 or tip of the branch) of 3 mm for the live tree and 1 mm for the printed tree was assumed, while the base diameters of the branches (D_b) were similar between the live and printed tree. This also implies that the tapering (branch slope) of the live trees is larger than the tapering of the branch mimics.

$$\tilde{Re} = \frac{1}{N}\sum_{i=1}^{N}\frac{(\overline{u}_h(z).\overline{D}(z))}{\nu} \quad (3.1) \qquad \tilde{KC} = \frac{1}{N}\sum_{i=1}^{N}\frac{(\overline{u}_h(z).T_p)}{\overline{D}(z)} \quad (3.2)$$

$$\tilde{Ca} = \frac{\rho l^3 \overline{u}_h(z)^2 \overline{D}(z)}{E\overline{I}(z)} \quad (3.3) \qquad I = \frac{\pi \overline{D}(z)^4}{64} \quad (3.4)$$

The horizontal velocity distribution, $u_h(z)$, was calculated with linear wave theory, using H_s and T_p, as follows:

$$u_h(z) = \omega_p \frac{H_s}{2}\frac{\cosh(k_p z)}{\sinh(k_p h)},$$

where wave angular frequency $\omega_p = \frac{2\pi}{T_p}$; wave number $k_p = \frac{2\pi}{L_p}$; and the wave length $L_p = \frac{gT_p^2}{2\pi}\tanh(k_p h_f)$. Finally, the average value was calculated over the water column. The $\tilde{KC}$ value was calculated in a similar manner. This method was different for $\tilde{Ca}$, we used the average diameter and average velocity over the height of each tree component (l).

3.2.6. Wave Damping, Transmission and Reflection

The incoming waves travel from deep water (measured by WG1-3) to the foreshore step (measured by WG4-5), where shoaling and depth-induced breaking of waves can occur. These waves travel further through the synthetic forest, where the incoming wave height decreases due to wave damping by the forest; and the transmitted waves reflect back by the dike slope behind the forest. The incident wave heights were determined at deep water (WG1-3), in front of the forest (WG4-6), and in front of the dike (WG8-10), using the method of *Mansard and Funke (1980)* for 3 wage gauges. For the real-scale experiments the wave separation was done considering a combination of measurements, namely: using the same method with 3 wave gauges in deep water; and co-located wave height and velocity gauges on the platform in front and behind the willow forest using an adapted Maximum Entropy Method *(van Wesenbeeck et al., 2022)*.

The amount of wave damping (Dr) was afterwards calculated in the same manner as

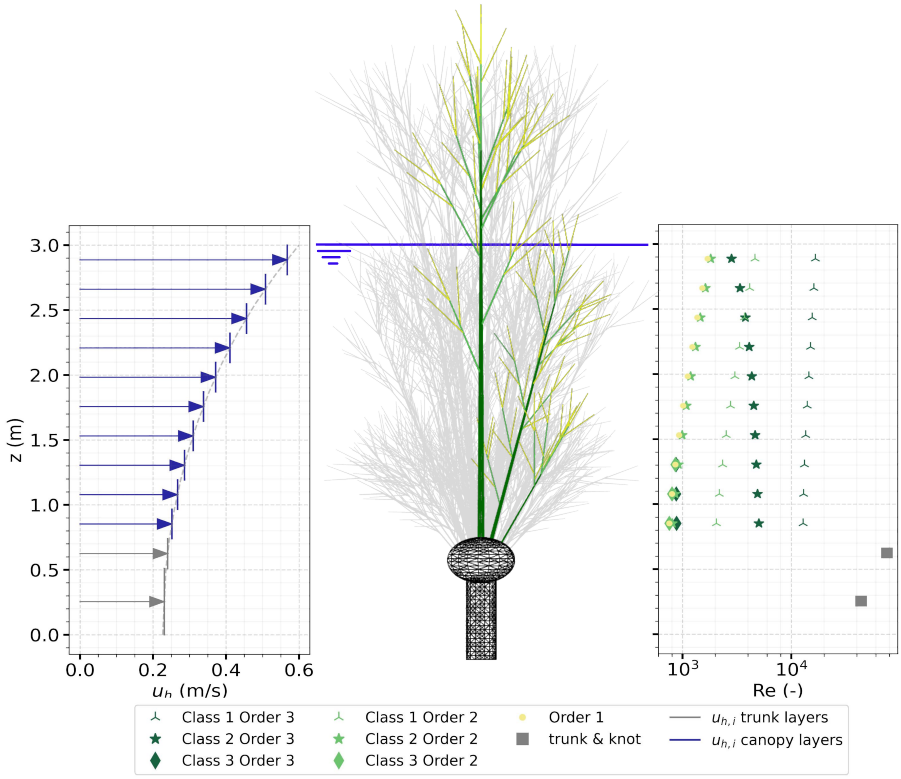

Figure 3.5.: Example of how the Reynolds number is calculated for test R001.

used in *van Wesenbeeck et al. (2022)*:

$$Dr = \frac{H_{m0_{cal}} - H_{m0_{wil}}}{H_{m0_{cal}}}, \tag{3.5}$$

where H_{m0} is the incident wave height behind the forest (i.e., in front of the dike measured by WG8, WG9 or WG10).

3.2.7. Branch Deflection

The branch deflection at both scales was analysed due to variations in dimensionless numbers, as shown in Table 3.1. This can impact the motion, and hence impact the wave damping. We focused on a medium branch (i.e., *Class* 2) situated in the first row of the forest, facing the wave-maker. The motion of the live branch was estimated by observing an orange coloured flag attached on the tip of the branch,

while the mimicked branch of interest was well captured from the side of the flume (see Section 3.2.1) and tracked by its distinct colour (i.e., white) compared to the colour of the canopy (i.e., black). The flag was captured with cameras above the flume (see Appendix C.2, Figure C.1A) with the camera locations obtained from photos of the camera setup. A grid with known dimensions (see Appendix C.2, Figure C.1B) was used to approximate the "real" deflection of the flag, and hence the live branch. Furthermore, we used *Premiere Pro 2022* to remove lens distortions associated with our type of camera (*GoPro HERO4*).

First, the distance between the flag and the camera was approximated to find the required corrections; then the deflections were obtained. The uncertainty bandwidth of the data is found by a sensitivity analysis on the relative distances. We refer to Appendix C.2 for a detailed description of the procedure.

Finally, the deflection is related to a certain wave height in front of the tree. We used linear wave theory to translate the surface elevations at WG6 to a location near the tree. For the scaled tests, this was not needed, as the wave gauge just in front of the forest (WG7) could be used.

The qualitative analysis to obtain the branch motion is performed on one test of 3 m water depth (R201) as the class 2 branch (medium) was not clearly visible during the high water level tests, h_f = 4.5 m (i.e., R205 and R206).

3.2.8. Extending Data Set

Besides the scaled tests that were equivalent to the real-scale tests (shown in Table 3.1), additional scaled tests were conducted. These scaled tests were performed with 100% density mimics and included additional wave conditions for the nearly submerged case (i.e., h_f= 0.45 m); and tests under fully submerged conditions (i.e., h_f= 0.57 m). The entire test overview is shown in Table C.1. These additional tests, thus far, lack the validation of the real-scale experiments. Their results are therefore corrected to obtain the wave damping by live willow trees under these additional hydrodynamic conditions. This was achieved by applying a correction factor (f_n) to the measured wave damping at small-scale. This factor is defined as the average ratio of the measured wave damping between the two scales, considering the 100% canopy density tests.

3.3. Results

3.3.1. Comparing Wave Damping

Two vegetation configurations, namely 100% canopy density and 50% canopy density, were tested at real-scale and 1:10 scale under hydrodynamic conditions shown in Table 3.1. Wave damping measured during the scaled experiments is compared to wave damping of the real-scale experiments, as shown in Figure 3.6. Data from the scaled experiments are all positioned above the grey solid line (real-scale tests); hence, measured wave damping by synthetic willows at a 1:10 scale was overall larger than the wave damping by realistic willow trees.

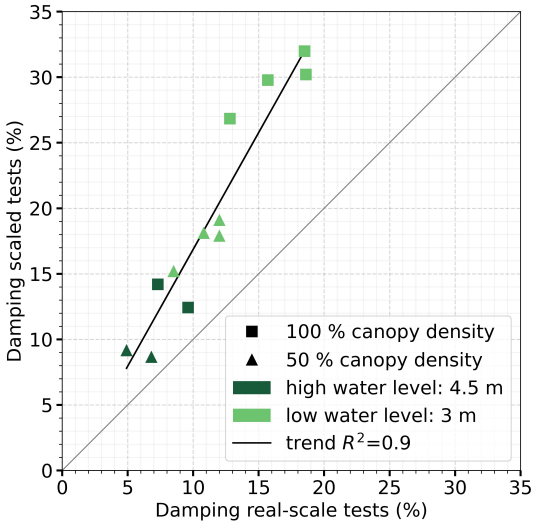

Figure 3.6.: Measured wave damping from real-scale experiments versus measured wave damping from scaled experiments (grey line); for vegetation with 100% canopy density (squares) and 50% density (triangles).

3.3.2. Comparing Branch Motion

The deflection of one medium branch was determined using video images from both scaled and real-scale experiments. The obtained estimated deflections are shown in Figure 3.7. The data points shown in this figure represent single waves taken from one irregular wave test with ca. 1000 waves at real-scale (R201 with h_f=3 m, H_s=0.5 m, T_p=2.83 s) and its equivalent scaled test (S201 with h_f=0.3 m, H_s=0.05 m, T_p=0.9 s). The uncertainty bandwidth for live branches is added as the exact positions of the live branch and camera were unknown. Overall, deflections of mimicked branches were

lower than the observed deflections of the live branches. For both scales, a positive trend is observed between wave height and deflection.

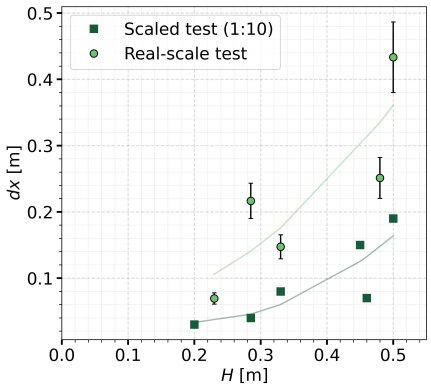

Figure 3.7.: Shows the maximum deflection (dx) with corresponding wave height (H). These results are for one test of the real-scale tests, R201 (squares), and scaled tests, S201 (circles). The deflection and wave height of test S201 were multiplied by $n_L = 10$.

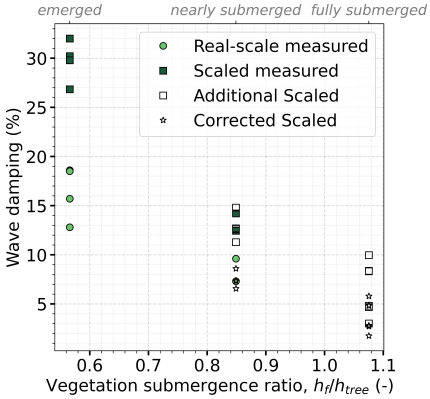

Figure 3.8.: Shows the measured wave damping through 100% density trees at real-scale (green circles) and scaled (green squares) for different submergence ratios; and additional scaled tests (squares) and the expected damping (stars) after applying a correction for scale errors on these additional scaled tests.

3.3.3. Correcting Wave Damping

The amount of wave damping through the forest with 100% canopy density is shown for emergent, nearly submerged, and fully submerged conditions (see Figure 3.8). Only the emergent and nearly submerged cases have equivalent real-scale results, while the fully submerged tests are shown with and without a correction factor, $f_n = 0.5$. After applying the correction factor, the results show that the fully submerged trees dampen significantly less waves than the emergent and nearly submerged cases.

3.4. Discussion

Until now, many studies on wave damping through woody vegetation have used data from scaled experiments that are susceptible to scale errors; which in turn can result

in discrepancies in wave attenuation through real-scale forests. Here, we confirm and illustrate the mismatch in wave damping between scaled and full-scale tests. Wave damping by a pollard willow forest is over-predicted by approximately a factor 1.5 in 1:10 scaled tests. This can be caused by multiple factors that we elaborate on below.

First, Froude similarity is applied for scaling these types of experiments; however, simultaneously the Reynolds number will deviate (i.e., relatively lower) from its prototype value. Usually a lower limit for Reynolds is used to still get similar wake formation behind the vegetation elements, yet very little to no data of full-scale tests with extreme conditions exist with live vegetation, thus the validation is lacking (e.g., *Wu and Cox, 2015*; *Maza et al., 2019*). In this study, we used data from full-scale experiments with live willow trees to design 1:10 scaled experiments, following Froude similitude. We scaled the trees according to the Cauchy number to replicate similar motion. However, there is no common approach to calculate these non-dimensional numbers (e.g., Fr, Re, and Ca). Most research uses a single value for defining dimensionless numbers. This is fitting for vegetation with relatively simple geometry such as salt marsh (e.g., *Luhar and Nepf, 2016*; *Jacobsen et al., 2019*). However, it becomes less representative for woody vegetation that consists of a trunk and canopy, which consists of branches of different orders. Previous studies on mangroves tried to include this by defining dimensionless numbers for roots, the stem, and the canopy (e.g., *Maza et al., 2019*; *He et al., 2019*; *Kelty et al., 2022*). This approach assumes an idealised vegetation model, implying that the elements of the roots or canopy did not vary in size or properties (e.g., single diameter). In the current study, we calculated dimensionless discrete numbers for the various components of the tree (i.e., trunk and various branch orders) in the water column and showed that this results in a wide range of values for dimensionless numbers (see Figure 3.5). Dimensionless numbers were defined on the scale of the single elements. Other studies (e.g., *Maza et al., 2019*; *He et al., 2019*) may use other characteristic length scales based on total canopy width or summed branch diameters, which can result in higher Reynolds numbers.

Second, the frontal-surface area distribution along the height of each individual trees, which was shown to be an important parameters in previous studies, was determined using various methods described in Chapter 2. During these experiments a comprehensive representation of the trees was discussed and we used these results for 3D-printing the mimics; hence, we regarded the frontal-surface area to be well-represented. Furthermore, fluid forces are argued to be more prominent in scaled experiments than in the prototype. This has been referred to in previous work as

'damping' effect (e.g., *Heller, 2011*). Hence, calibration runs (tests without vegetation) were included in our test program to account for the influence of bed and wall friction at both scales. At the same time, we excluded the leaves from the scaled tests as large over-estimations of wave damping are expected, as Cauchy scaling of leaves and finding the appropriate material is prohibitively challenging. Most importantly, the leaves of the real-scale willows had an insignificant effect on wave damping under storm conditions *van Wesenbeeck et al. (2022)*. In the end, we observed still overestimation effects in the scaled tests that could not be fully explained by a single reason. It is assumed that this large component can be caused by the following reasons: (1) dissimilar Reynolds number leading to increased viscous damping, (2) simplified flexibility scaling, and (3) other mechanisms (such as air entrainment differences).

3.4.1. Reynolds scale effects

Firstly, Fr similitude was used to scale the global hydrodynamic conditions of these experiments and Ca for the trees, while Re was not considered. Re is nevertheless important to ensure similar wake formation behind the structure, making both Fr and Re necessary to investigate the wave transformation through vegetation. Generally lower Reynolds numbers were obtained during these scaled experiments, compared to the real-scale tests that were in fully turbulent flow. As a consequence of this, higher drag forces can be expected for lower Reynolds numbers. The Re-C_D relation is represented in Figure 3.9 for a single rigid cylinder in flow *Sumer and Fredsoe (1998)*. The $\tilde{Re}$ range of the largest and smallest branches was added to this figure, illustrating the difference in regimes between the two tested scales, especially for the smallest diameter branches. This difference alone could lead to an increase of 5% points in wave damping through the 40-metre-long willow forest. This estimation was based on the conventional analytical formula (*Dalrymple et al., 1984*; *Mendez and Losada, 2004*), using a weighted average drag coefficient (C_{Dw}) based on Figure 3.9 for both the average live tree ($C_{Dw} \approx 1$) and the mimicked tree ($C_{Dw} \approx 1.37$) (see Appendix C.3).

For high Reynolds numbers ($\geq 10^4$), which usually is the case in real-scale settings, the friction drag only accounted for maximum 2% of the total drag force and pressure drag is the main contributor *(Achenbach, 1968)*. For lower Reynolds numbers, where there is not yet complete turbulent wake development behind the branches, the skin friction might increase depending on the relative roughness of the object (Moody diagram). This is also expected between 3D-printed branches and fluid, leading to higher friction and causally higher wave damping. On the other hand, the roughness

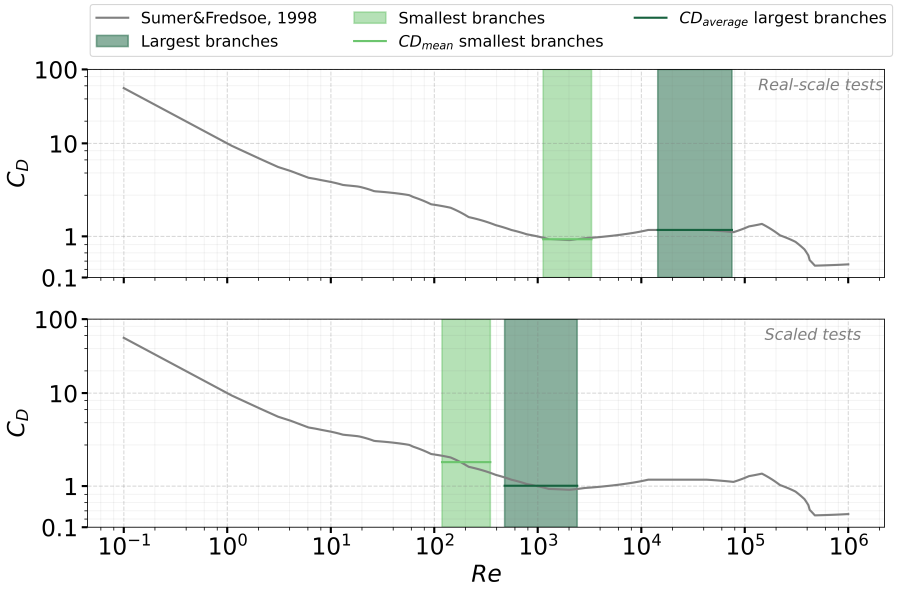

Figure 3.9.: shows the *Re* range of the real-scale tests (upper) and the scaled tests (below) for the smallest and largest branches.

of parts of the live tree can lead to earlier transition to turbulence (drag crisis). As this is mainly the case for the trunk and knot of the willow trees, this most likely has a negligible effect on the measured wave damping.

The orientation of the cylinder (branch) relative to the incoming velocity can also affect the forces if the angle of attack is larger than 35° *(Sumer and Fredsoe, 1998)*. Moreover, this dependency disappears for oscillatory flow when KC is large enough ($KC \geq 20$) *(Sumer and Fredsoe, 1998)*. The angle of the side branches relative to the trunk (0°) can be 30° for the 2nd order branches and can reach up to 55° for the 1st order branches (i.e., smallest branches), leading to angle of attack $\approx 35°$ for the smallest branches and the tests have a minimum *KC* of 22, which is yet within both previously mentioned ranges, hence well-resembled.

3.4.2. Flexibility model effects

Secondly, woody vegetation also moved when subjected to storm waves, as discussed in *van Wesenbeeck et al. (2022)*. For simplicity, vegetation is usually considered to behave as rigid cylinders (e.g., *Hu et al., 2014*; *Tinoco and Coco, 2018*; *Sonnenwald et al., 2019*). However, these simplifications can lead to wave damping overestimations. Vegetation motion was shown to impact the amount of wave damping

van Veelen et al. (2020). Relatively smaller deflection was measured in the scaled model compared to the real-scale tests, which can be a consequence of the variability of the Young's Modulus. Studies showed that the E-modulus of branches is not constant across different sections of the branches, such as *van Starrenburg et al. (2024)*, while we used a single value for the Young's modulus, E. For example, *Sutili et al. (2010)* conducted bending tests for 6 different diameter classes of *Salix* $\times$ *Rubens* (willow species), and showed that the average Young's modulus ranged from $\approx$ 3.000 - 5000 $\mathrm{N/mm^2}$ depending on the diameter class.

Besides simplifications regarding the Young's modulus, we also simplified the geometry. Branches with a smaller diameter than 1 mm were not possible with the 3D-printer. To still get similar frontal surface area, we lumped the smallest order branches together. The volume is however not similar between model and prototype. This could result in deviations in inertia forcing; however, we do not expect inertia to play an important role relative to the drag force as the KC number of these small branches is large (see Table 3.1), indicating drag-dominated regime *(Sumer and Fredsoe, 1998)*.

The geometric simplifications lead to thicker and thereby also stiffer 1st *order* branches than required, and stiffer objects are generally known to dampen more than flexible alternatives *(Mullarney and Henderson, 2010)*. One could argue that this is also the case for the printed branches. The flag used for the motion analysis at real-scale, was attached on a 1st *order* branch – a relatively more flexible branch than its scaled mimic. The analysis on the maximum deflection of the tip of the branch (see Figure 3.7) illustrated that the live branches had larger tip displacement than the 3D-printed trees. This is in line with the wave damping measurements: less wave damping for the live trees (more flexible small branches) that also showed more deflection under waves. The discrepancies between the deflections at the two scales were more apparent for higher waves; and we expect a similar trend for the other tests. Unfortunately, this comparison could not be made for these irregular wave tests with larger significant wave heights or higher water levels, as the branch of interest was not visible during these tests. On the contrary, the contribution of the smallest branches to the wave damping is also unknown. We expect the motion of the tip of the branches (i.e., smallest diameter and highest flexibility) to have less impact on the wave damping than the motion of the primary branches. Previous work for example used an effective length parameter for blades *(Lei and Nepf, 2021)*. It is therefore relevant to investigate the effectiveness of the different branch orders in wave damping.

3.4.3. Aeration (Weber) scale effects

Thirdly, waves that travel through the forest, undergo wave transformations and also changes in air entrainment *(Tomiczek et al., 2020)* that can impact the interaction with the structure, and in turn also the wave damping results from scaled tests. Furthermore, only few studies compared scaled experiments to prototype tests for wave damping by woody vegetation. For example, *Kelty et al. (2022)* showed a good agreement between synthetic mangrove forests at two scales. These tests had relatively large scale and rigid tree models, such that here this aeration effect was isolated. The direct effect of decreased mass density does not influence wave damping, as mass density is present in both the wave energy flux and the dissipation term, such that it cancels out in the final dissipation equation, Appendix C.3.1. Overall, this effect is deemed to be smaller than the first two effects.

3.5. Conclusions

Scaled tests with Cauchy-scaled pollard willow mimics (30%) resulted in higher wave damping compared to real-scale tests (20%). This over-prediction is argued to be mainly due to scale effects (Reynolds dissimilarity) and to model effects, impacting flexibility of the canopy. The trade-off between Fr and Re and flexibility modelling is challenging, but nevertheless important to get reliable wave damping results from these tests. Concluding, real-scale studies on realistic vegetation are still warranted to improve our understanding of wave attenuation by flexible woody vegetation. The wave damping by trees is a multi-scale problem. The different elements of a tree (e.g., trunk and branches) are characterised by distinct dimensions and mechanical properties; the drag force experienced by the tree is influenced by the vortices and wave development at canopy-scale and element/branch-scale. We showed the importance of considering all elements of a tree (i.e., smallest to largest size branches) as this leads to a wider range of relevant force ratios. Capturing these elements on a smaller scale was technically and time-wise not feasible. To ensure proper up-scaling for flood risk estimations, correction factors can be considered as presented in this study. Still, more research is needed on varying the scale of the tests, the vegetation properties such as flexibility, and identifying other uncertainties. Based on our results, scaled experimental studies should only be used for conservative wave damping estimates if no real-scale validation study is available.

Photography by Mischa Keijser

4

Flexibility Effects

4.1. Introduction

Woody forests, such as mangroves along coastlines and willow trees in riparian zones, are known to alter the hydrodynamics in their surroundings, thereby increasing safety against flood events. For instance, studies have shown that mangroves can reduce flow velocities and decrease wave heights (*Quartel et al., 2007*; *Bao, 2011*; *Horstman, 2014*; *Best et al., 2022*), promoting sedimentation and stabilising coastlines (*Phuoc and Massel, 2006*; *van Wesenbeeck et al., 2013*). Furthermore, their ability to dampen wave energy can lead to lower hydraulic loads on existing levees or dikes, potentially reducing costs (*IFRCRCS, 2014*; *Gijón Mancheño et al., 2021*; *van Zelst et al., 2021*).

A recent real-scale flume study has demonstrated the resilience of the riparian forest during extreme events, representative of the design conditions for adjacent flood defences *(van Wesenbeeck et al., 2022)*. During these real-scale experiments with pollard willow trees (forming a 40-m-long forest), a maximum reduction in wave height of 20% was measured. In particular, this amount of wave damping occurred at a water depth of 3 metres, whereby the water line was aligned with the maximum frontal-surface area of the tree canopy. For a larger water depth, wave damping declined to 10%. One reason for this can be the natural tapering form of the trees or the flexibility of the branches. Typically, trees are characterised by thinner branches (smaller branch diameters and also more flexible branches) higher up in the canopy *(McMahon and Kronauer, 1976)*. Flexible vegetation mimics are known to dampen less than rigid mimics due to motion *(van Veelen et al., 2020)*. Hence, the increasing flexibility higher up in the canopy, combined with a decreasing frontal-surface area, may lead to less wave damping through the willow forest when subject to large waves at larger water depths.

Research on the effects of flexibility on wave damping was predominantly focused on aquatic or salt marsh vegetation (*Luhar and Nepf, 2016*; *Hong et al., 2022*), which are typically more flexible than woody vegetation. Consequently, the role of the flexibility of trees, such as willows and mangroves, has been largely neglected in wave damping studies. Instead, rigid cylinders are often used as vegetation mimics (*Hu et al., 2014*; *Wu and Cox, 2015*; *Sonnenwald et al., 2019*) or tree components (such as mangrove roots) are treated as inherently rigid structures *(Maza et al., 2019)*. Furthermore, when flexibility effects are considered, research typically focusses on stems with a constant cross-section (diameter and flexibility EI), overlooking the variation of these parameters over the height of the vegetation (e.g., *Luhar et al., 2010*).
Wave damping through idealised 'rigid' vegetation is commonly parametrised by the drag force acting on the vegetation (using the Morison formulation as basis) (*Dal-*

rymple et al., 1984; *Mendez and Losada, 2004*). For trees, this formulation can be applied for several layers along the height of the tree, as each layer can have different properties (generally stem/branch density and representative diameter) *(Suzuki, 2011)* and by using an empirically fitted drag coefficient (C_D) to field or laboratory measurements. However, the drag coefficients derived with such approaches display a wide spread, which hinders their application in NbS designs *(Het Expertise Netwerk Waterkeren, 2007)*. For example, calibrating C_D for forests is a common method to account for any effects that are not directly accounted for by this formula, such as branch thinning from base to tip and flexibility effects. The large differences in C_D values for woody vegetation could be due, among others, to the omission of these aspects mentioned. Moreover, most scaling relationships are based on Re and KC – parameters often used for rigid cylinders — which are ill defined for real trees with complex morphology, flexibility and motion. The degree to which the previous aspects influence the uncertainty in parametrisations of wave damping by woody vegetation, and their relative importance, is currently unknown.

Here, we conducted scaled flume experiments with flexible realistic tree mimics and conical shapes, considering pollard willow trees (Figure 4.1a) and branches (Figure 4.1b). By doing so, we tested the effects of (1) decreasing frontal-surface area, and (2) increasing flexibility along the height of the object. Past studies showed that the Modulus of Elasticity (or Young's modulus) of willow branches deviates over a large range between willow species *(van Starrenburg et al., 2024)* and (or) between branch orders *(Sutili et al., 2010)*. Therefore, materials were selected to ensure a wide range of flexibility. The extent to which flexibility influences the forces on these mimics of woody vegetation was determined by using force and video data. The rigid cone tests served not only as a benchmark for these tests, but were also used to determine C_D for conical shapes. Dimensionless parameters, such as Cauchy (Ca) that are used to characterise cylindrical shapes *(van Veelen et al., 2021)*, were defined and quantified to verify whether these are reliable indicators for predicting the motion of flexible cones under regular waves. Finally, forces on complex trees were measured, which will provide valuable insights for future wave modelling studies.

4.2. Flume Experiments

Experiments were carried out on a scale of 1:10 (with respect to the tests described in Chapter 3) with conical shapes, representing the branches of pollard willow. The main focus of these tests was to keep the frontal-surface area distribution over the water column and the second moment of area (I) constant between tests, while changing

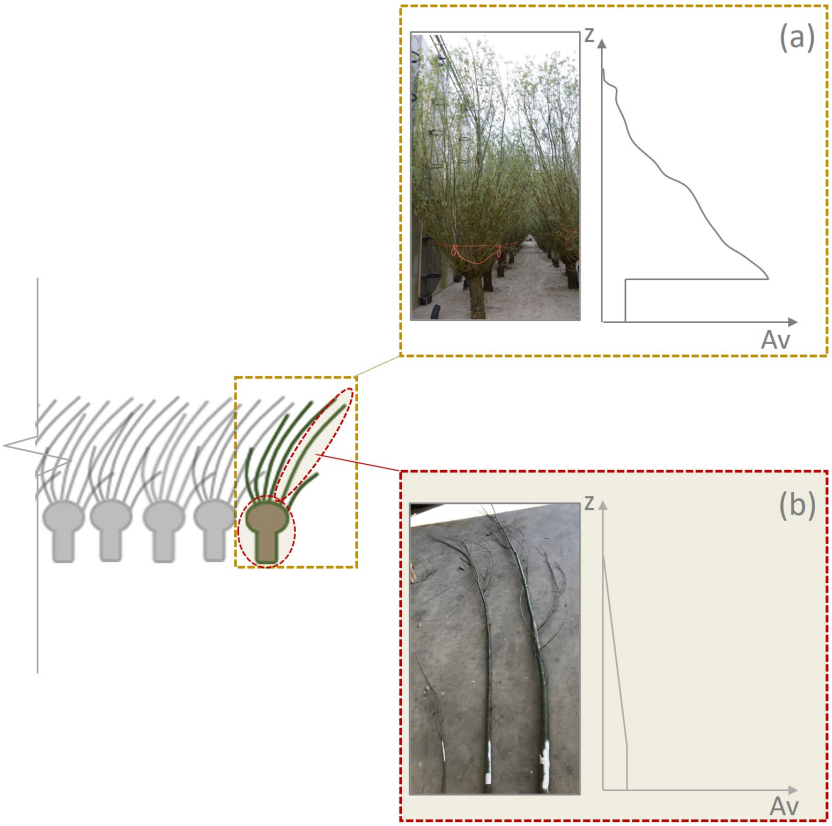

Figure 4.1.: shows a conceptual design of the mimics **(A)** at tree scale, and **(B)** at branch scale a decrease in frontal-surface area along the height.

the Young's Modulus (E) and thereby the flexibility of the objects. In this case, the diameter was similar between the test cases and, therefore, also the Reynolds number ($Re = \frac{UD_b}{\nu}$) and the Keulegan-Carpenter number ($KC = \frac{UT}{D_b}$, where D_b is the branch diameter at the base). In addition to the cone tests, we also conducted tests with a 6-cone tree (simple) and 3D-printed trees (complex), both with two different materials (stiff and flexible). Furthermore, we removed all the side-branches of the complex trees, keeping only the primary branches of the tree (i.e., main branches attached to the knot of the tree). This can be useful in determining the contribution of the side branches – most flexible parts of the tree – to the total force; however, this is outside the scope of this work.

4.2.1. Experimental Set-up

Tests were conducted in a wave flume (height×width ×length = 1 m×0.8 m×40 m) that contained a wooden platform (0.23 m in height). The object was placed after a wooden platform with a 1:10 slope. A force transducer was placed underneath the object, inside the platform to measure the total force on the object without obstructing the velocities. The forces on the entire object were measured with the force transducer (FT). Wave heights were measured with a Wave Gauge (WG7). The motion of the cone was recorded with a camera (*Sony 4K FDR-AX33 20.6 MegaPixels Handycam*). Flow velocity was measured using EMS at the position of the object (EMS3) (Figure 4.2). A wave damping structure was placed at the end of the flume. Additional equipment, such as velocity and wave gauges, was present in the flume but not used in this study.

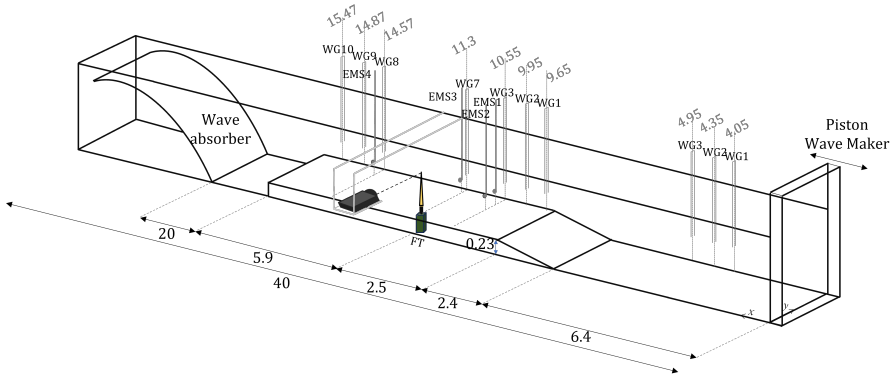

Figure 4.2.: An overview of the test set-up, including all the instruments placed along the flume.

4.2.2. Hydrodynamics

Individual cones and 6-cone tree mimics were tested under regular wave conditions, while realistic trees were tested under irregular waves. The results from the realistic trees were compared to those from the earlier test campaign in Chapter 3, which involved flexible realistic trees with similar morphology. The test programme consisted of 20 different wave conditions shown in Figure 4.3, in which the water depth at the foreshore (h_f), wave height in deep water (H) and the wave period (T) are given. Most of the waves were non-breaking waves, except for tests 6, 9 and 10. The complete test programme and the positions of all the placed instruments are given in Appendix D.1.

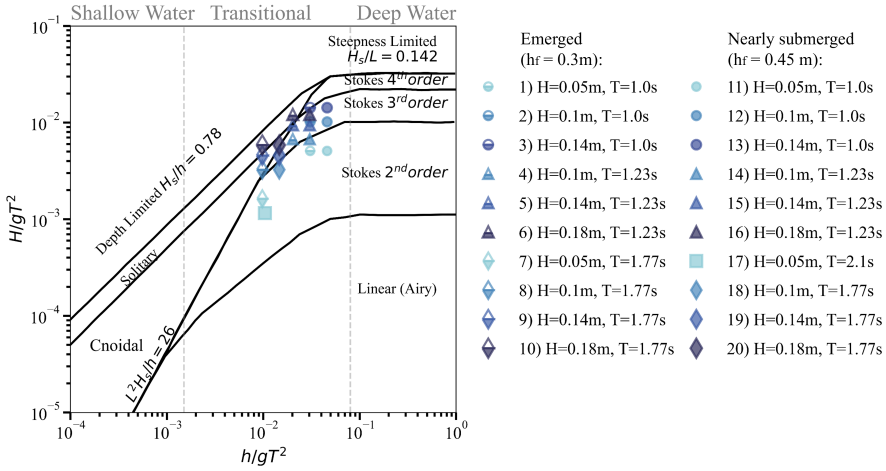

Figure 4.3.: The regular wave conditions (test 1 -20) and their location in the diagram of applicability of different wave theories (adapted from *Le Mehaute (1976)*).

The complex trees were tested under irregular wave conditions for 3 water depths (see Table 4.1).

4.2.3. Vegetation Mimics

Vegetation mimics were based on the live pollard willow trees in *van Wesenbeeck et al. (2022)* and *Kalloe et al. (2022a)*; and consisted of a stiff cylinder (height= 10 cm, base diameter= 3.45 cm) that represents the trunk, and a cone (length= 42.5 cm) that can represent a canopy or branch. The canopy consisted only of one simplified branch in the form of a cone, focussing on the motion of a single element. The

Table 4.1.: Irregular offshore wave conditions with the complex tree mimics with and without side branches. h_d is the water depth at deep water (offshore), while h_f is the water depths at the foreshore.

Emerged conditions (h_d= 0.53 m, h_f = 0.3 m)			Nearly submerged conditions (h_d = 0.68 m, h_f =0.45 m)			Submerged conditions (h_d = 0.8 m, h_f = 0.57 m)		
Test (-)	H_s(m)	T_p(s)	Test (-)	H_s(m)	T_p(s)	Test (-)	H_s(m)	T_p(s)
1	0.05	0.9	5	0.05	0.9	11	0.05	0.9
2	0.12	1.13	6	0.1	1.27	12	0.12	1.13
3	0.05	1.27	7	0.05	1.27	13	0.05	1.27
4	0.10	1.79	8	0.1	1.79	14	0.1	1.79
			9	0.16	1.55	15	0.16	1.55
			10	0.15	2.19	16	0.15	2.19

cone had a constant height (l) of 0.425 m, while the base diameter (D_b) varied. The following two base diameters were tested: (1) 0.0346 m denoted as '*Large Cone*' and (2) 0.0137 m denoted as '*Medium Cone*'. Both cone sizes were 3D-printed using four different materials with varying Young's modulus (E), namely: 3200 MPa (stiff), 56 MPa, 7.5 MPa, and 5 MPa. Important dimensionless numbers, namely the Keulegan-Carpenter and Reynolds numbers, are calculated across the vertical axis (z) to have an indicator of the flow regime we can expect around the objects.

$$I(z) = \frac{\pi}{64} D_c^4(z),\ Re(z) = \frac{U_{h,max}(z).D_c(z)}{\nu},\ KC(z) = \frac{U_{h,max}(z).T}{D_c(z)}$$

An overview of both cone models with varying rigidity (EI), KC and Re along the height of the cones is shown in Figure 4.4. For further details on the printer settings and materials, we refer to Appendix D.2.

For conical shapes, $\tilde{Ca}$ and $\tilde{L}$ are defined as follows:

$$\tilde{Ca} = \frac{\rho_w \bar{D} \hat{U}_{h,max}^2 l_{wet}^2 l_{cone}}{E\bar{I}},\ \tilde{L} = \frac{l_{cone}\omega}{\hat{U}_{h,max}}, \tag{4.1}$$

where $\omega = \frac{2\pi}{T}$, $\hat{U}_{h,max}$ represents the horizontal orbital velocity at the waterline according to linear wave theory, $\bar{D}$ is the average diameter throughout the length of the cone and $E\bar{I}$ is the average rigidity throughout the length of the cone (see Figure 4.4).

The *'Medium'* cone was used to construct a 6-cone tree mimic (see Figure 4.5C), which was tested in two variations: one with high stiffness ($E = 3200$ MPa) and the

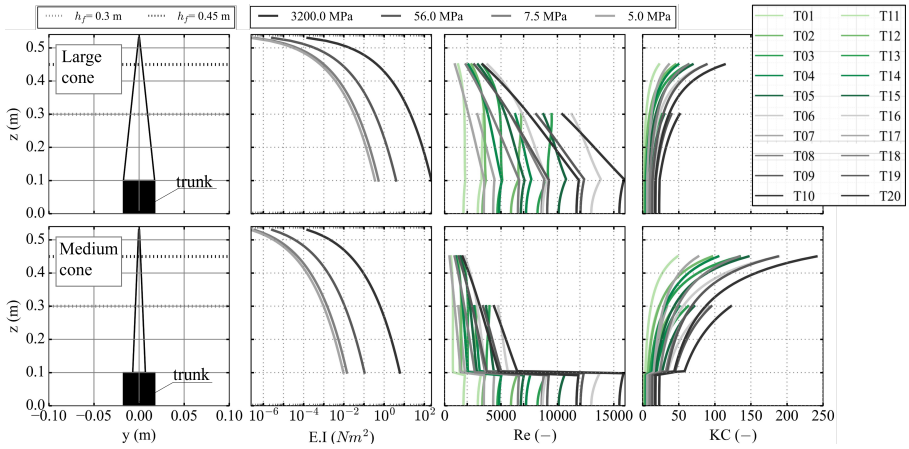

Figure 4.4.: Overview of the geometry of the cones with corresponding stiffness (EI), Reynolds number (Re) and Keulegan-Carpenter number (KC) along the height of the object.

other with low stiffness ($E = 7.5$ MPa).

Furthermore, we reused one *'Realistic'* tree that was in the front row of the forest tested in Chapter 2: *'Tree A1'*. The realistic tree mimic was also tested in a relatively stiff variation (E = 3200 MPa) and a flexible variation (E = 400 MPa).

As mentioned before, the effect of the side-branches was not investigated in this work. We removed all the side-branches (both 1st and 2nd order branches), leaving only the primary branches in the tree (see Figure 4.5B). However, for completeness, the characteristics of the trees are described in Appendix D.1.

4.3. Data processing

4.3.1. Force Measurements

The force transducer, placed below the trunk, measured the horizontal component of the total force on the objects (shown in Figure 4.5). The forces on the cone (i.e., excluding the trunk) were also estimated for further analysis. These cone forces were determined by subtracting the time-series measurements of the trunk tests ('calibration tests') from the tests with the whole object ('trunk+cone'). Hereafter, the first five fully developed waves were selected to calculate the average peak force (F_p). Figure 4.6 shows an example of the cone forces of test 1 with the stiff *Large Cone*. The averaged peak forces obtained for the stiff cones were compared with the results of the flexible cones of identical geometry. We followed these steps to obtain peak

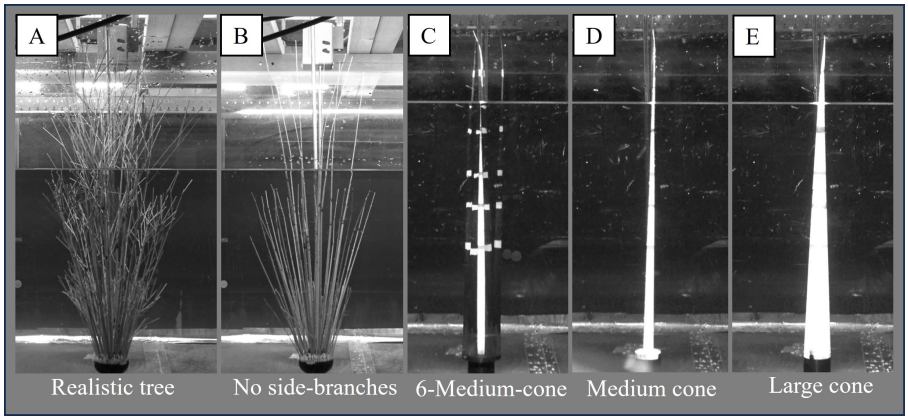

Figure 4.5.: Shows an overview of the tested realistic tree mimics (A and B) and simplified branch mimics (C, D, and E).

forces on all the individual conical shapes and on the 6-cone mimics. Furthermore, the effect of flexibility on the forcing is also analysed for the 'realistic' trees under irregular wave conditions. For this, we compared the significant force on the entire flexible tree with the significant force on the geometrically equivalent stiff tree.

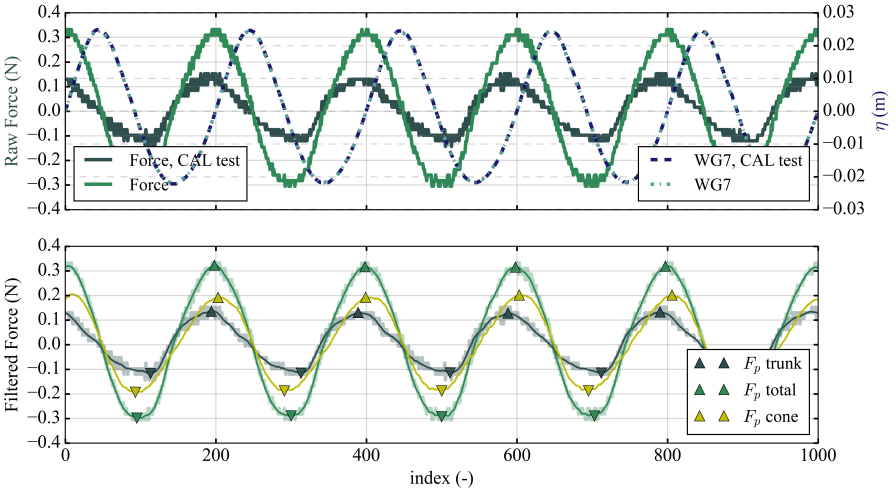

Figure 4.6.: A measurement time series of 5 waves to obtain the average peak force of the cone (yellow upward triangles), F_p. Test 1 with stiff *Large Cone* is shown as an example.

4.3.2. Velocity profiles - Regular Waves

Velocity profiles over the water column were estimated using Fenton's theory (higher-order waves) *(Fenton, 1985)*. The surface elevation predicted by Fenton was compared with the surface elevation measurements (from WG7). Appendix D.3 shows this with the corresponding velocity profiles for each regular wave test.

4.3.3. Video Images Cones

The maximum horizontal displacement that the cone experiences (θ) was determined by recording and tracking the movement at a point located at $\approx 0.7\times$length of the cone, l. This specific point was chosen because it minimises the influence of higher-order modes (up to mode 3) on the motion. This point is shown with the horizontal green dashed line in Figure 4.7A. The shapes result from the modal analysis of a modified version of the model developed by *ter Meulen et al. (2024)*. The cone was represented with 10 two-node 2D Euler-Bernoulli beam elements. The entire length of the cone was hence discretised with 11 nodes (see Figure 4.7A), where each node (except for the base node which serves as a clamped connection) has 3 degrees of freedom. The geometric properties of the elements change along the height of the cone, for instance, the diameter, and therefore the mass and flexural rigidity EI decrease per element. Details on the input can be found in Appendix D.4.

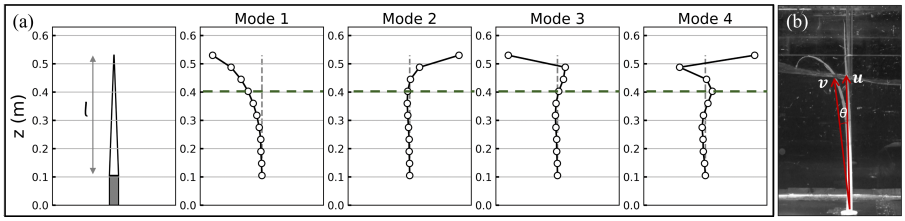

Figure 4.7.: (A) *Large Cone* and its modal shapes (in vacuo modes); (B) example of obtaining θ.

The maximum angle of deflection was determined as the angle between two vectors. First, the state of the cone at rest is vector u, and the state of the cone at maximum deflection is vector v (see Figure 4.7b). The angle θ between the vectors $\vec{u}$ and $\vec{v}$ is:

$$\theta = \cos^{-1}\left(\frac{\vec{u}\cdot\vec{v}}{\|\vec{u}\|\,\|\vec{v}\|}\right),$$

where the dot product $\vec{u}\cdot\vec{v}$ is defined as:

$$\vec{u} \cdot \vec{v} = u_x v_x + u_y v_y,$$

and the magnitudes of the vectors are:

$$\|\vec{u}\| = \sqrt{u_x^2 + u_y^2}, \quad \|\vec{v}\| = \sqrt{v_x^2 + v_y^2}.$$

Furthermore, the video images were also used to obtain the change in position of the cone (response) of the flexible cones over time. The video images were first synchronised with the wave gauge and force data using cross-correlation. For this, data from wave gauge 7 (WG7), located at the tree, was used to ensure that the correlation between the video and wave gauge data exceeded 0.9. After synchronising these data sets, five developed waves were chosen for analysis in this work (by excluding the first 10 waves). Finally, 20 video frames during each wave cycle were used to track the position of the object during one wave. Colour masks were used mainly to obtain the shape of the cones. For more details regarding these video processing steps, we refer to Appendix D.5.

4.4. Results and Discussion

4.4.1. Realistic Tree Mimics

The effect of flexibility on the measured forcing was analysed for realistic tree mimics under irregular wave conditions. We compared the significant peak forces (F_s) measured on the entire flexible tree (including the stiff trunk) to those of the geometrically equivalent stiff tree, as shown in Figure 4.8A.

The results indicate that F_s increases with the calculated depth-averaged maximum velocity based on Linear Wave Theory ($\tilde{U}$), following the classic quadratic drag law $F \propto U^2$. For the stiff trees (dark green markers), the relationship between force and velocity aligns with this law. This relationship has also been observed in other studies using stiff mangrove mimics under varying water depths *(Maza et al., 2017b)*. However, for realistic vegetation with flexible branches, this relationship may deviate. *Vogel (1989)* demonstrated that the force-velocity relationship is not necessarily quadratic, introducing the equation $F \propto \tilde{U}^{2+v}$, where v is the *Vogel* exponent, for regular waves and cylindrical shapes. The range for this exponent is -4/3 $< v <$ -1/10 *(Hong et al., 2022)*, suggesting a more linear relationship between force and velocity. This alteration in the $F - U$ relationship is primarily due to flow-induced deformation, also known as vegetation reconfiguration *(Vogel, 1989)*, which depends on both

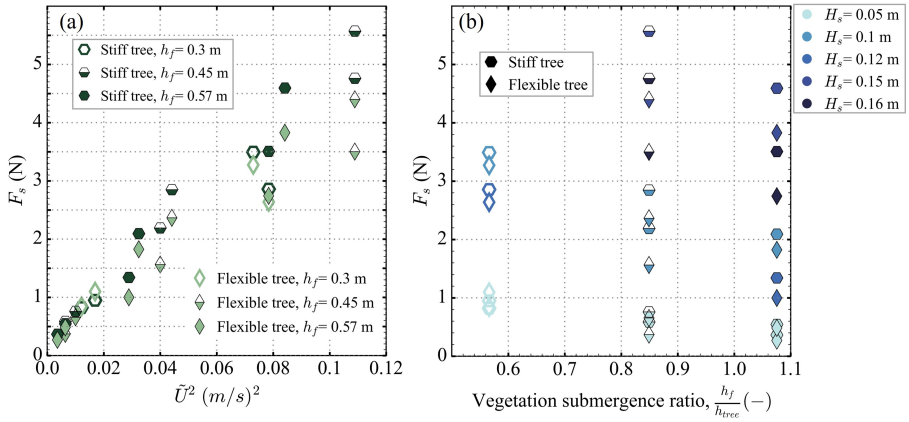

Figure 4.8.: **(a)** Measured significant peak forces (F_s) as function of the calculated depth-averaged maximum velocity based on Linear Wave Theory ($\tilde{U}$) with corresponding water depth (h_f). This is shown for the stiff tree (dark green hexagons) and flexible tree (light green diamonds). **(b)** Force difference for different tree submergence levels.

plant properties (such as structural geometry and material properties) and flow characteristics (such as the velocity profile) *(Hong et al., 2022)*. Our results align with observations by *Hong et al. (2022)*; our F_s measurements for the flexible tree (light green markers) are overall lower than those for the stiff tree (dark green markers). This difference tends to increase with increasing velocities, indicating that a more flexible tree indeed demonstrates a more linear $F-U$ relationship (*de Langre, 2008*; *Leclercq and de Langre, 2016*). This also coincides with findings from a full-scale study conducted with live flexible riparian trees under flow, where the quadratic drag equation seems to be appropriate for very low velocities, while less accurate for high velocities *(Whittaker et al., 2013)*. Notably, in our tests, this relationship was not apparent when using the maximum velocity $\hat{U}_{max}$ instead of the depth-averaged velocity $\tilde{U}$ (see Appendix D.6).

In addition to the velocity relationship, our results illustrate how the level of submergence influences the force experienced by the flexible versus stiff tree. Figure 4.8B shows the measured peak forces at various vegetation submergence levels for flexible trees (diamond markers) and stiff trees (hexagon markers). Flexibility has a minor effect at the lowest water depths (h_f = 0.3 m) compared to the other tested depths, regardless of the velocity. The smallest difference between the tests occurs for the 'emergent' trees ($h_f/h_{tree} \approx 0.55$), corresponding to the waves reaching the least flexible parts of the tree. The largest difference is observed for the 'nearly emergent'

case ($h_f/h_{tree} \approx 0.85$). The force difference between the stiff and flexible trees decreases again for the 'fully submerged' case ($h_f/h_{tree} \approx 1.1$) compared to the 'nearly emergent' case. Moreover, Figure 4.8B demonstrates that vegetation submergence is important not only for the force difference due to flexibility, but also for the total force exerted on trees (and therefore for the expected wave damping by the trees). *Anderson et al. (2011)* showed that the wave damping depends on the plant structure (frontal-surface area) relative to the water depth. Most studies with flexible vegetation show more wave damping at lower water depths (*Stratigaki et al., 2011*; *Maza et al., 2015*). In our scaled experiments, the smallest water depth did not directly correspond to the largest measured forces. Instead, the largest forces were found in the nearly submerged cases (h_f = 0.45 m), which then decreased for the fully submerged case (h_f = 0.57 m). This is arguably due to the higher wave heights achieved in the nearly submerged case compared to the emergent case. Therefore, when comparing similar wave heights among different vegetation submergence levels, the lower water depths indeed experienced the highest forces.

While the analysis of realistic tree mimics provides valuable insight, the study of conical shapes offers a more controlled approach by removing additional effects caused by complex geometries, such as interference by neighbouring branches, varying angle of wave attack, and shape factors on (side) branches with different orientations. The upcoming sections will therefore focus on the conical shapes.

4.4.2. Flexible Cones

The reduction in force due to flexibility is quantified by comparing the peak force of the flexible cone to that of its rigid counterpart ($F_{p,flex}/F_{p,stiff}$). Appendix D.8 presents the peak forces acting on the cone ($F_{p,cone}$), the total peak forces on the trunk&cone ($F_{p,total}$), and the measured cone deflections (θ) for each test. The Large Cones (squares) show relatively smaller deflections ($\theta < 5^{\circ}$) than the Medium Cones (triangles), see Figure 4.9. This is due to the greater overall rigidity (EI) of the Large Cones compared to the Medium Cones. It is important to note that tests involving the *Large Cone 56* MPa (here 56 MPa represents the modulus of elasticity E of the cone material) showed minimal deflections for all tests and were therefore excluded from this analysis.

These results demonstrate an overall declining trend in the measured force-deflection relationship, as expected. This indicates that more flexible cone mimics (represented by lighter green markers) exhibit relatively larger deflections and experience lower peak forces compared to stiffer mimics (represented by darker green markers). Con-

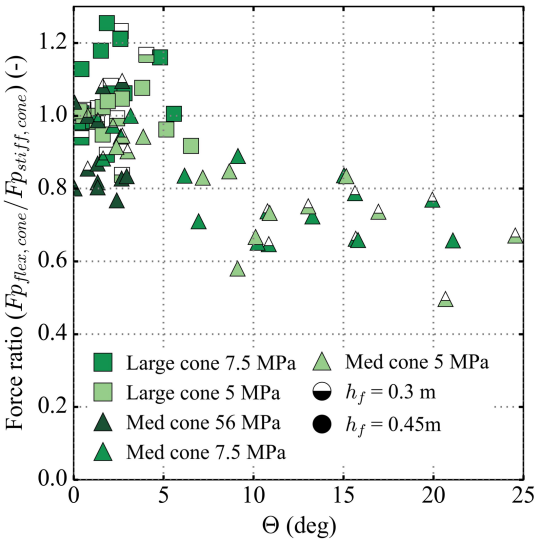

Figure 4.9.: The cone without the trunk ($F_{p,flex,cone}$/ $F_{p,stiff,cone}$). This is illustrated for both Large (squares) and Medium cones (triangles) for two tested water depths (h_f). The colours represent the E-modulus, with dark green indicating lower flexibility and light green indicating higher flexibility.

sequently, we expect reduced wave damping from more flexible conical shapes compared to geometrically equivalent stiff cones. The reduction in wave damping by flexible vegetation is supported by other studies. For instance, *Mullarney and Henderson (2010)* found that the wave damping by salt marsh vegetation was 30 % of that expected from stiff mimics based on field measurements. Similarly, *van Veelen et al. (2020)* reported a 70 % reduction in the drag coefficient for flexible mimics compared to stiff mimics.

Lastly, in certain low deflection cases, mainly for the large flexible cone tests, the peak force increased to a factor of 1.2 compared to the equivalent stiff cone tests. This increase might be attributed to the lock-in phenomenon, where high-frequency lateral oscillations caused by vortex-induced vibrations can occur *(Hong et al., 2022)*, which were also observed in the tests (see Appendix D.7).

4.4.3. Drag Coefficients of Cones

Many studies use the drag coefficient, C_D, of stiff cylinders to model wave damping through woody vegetation. However, in this study, we modelled willow trees using conical shapes and hence determined the drag coefficient of stiff cones. Tests

with stiff large and medium conical shapes were used to find these drag coefficients. Figure 4.10 illustrates that the drag coefficient decreases with increasing KC numbers for both Large and Medium cones. This trend is similar to that observed for stiff cylindrical shapes, where C_D decreases between 1 and 1.5 for high KC numbers (*Keulegan and Carpenter, 1958*; *Wu and Cox, 2015*). The C_D values in this work were obtained using the peak force measurements and peak velocities calculated with Fenton's Theory; this analysis was carried out on a selected subset of tests with KC numbers greater than 20. The main assumption is that the peak force on the object is governed by drag, neglecting the inertia forces.

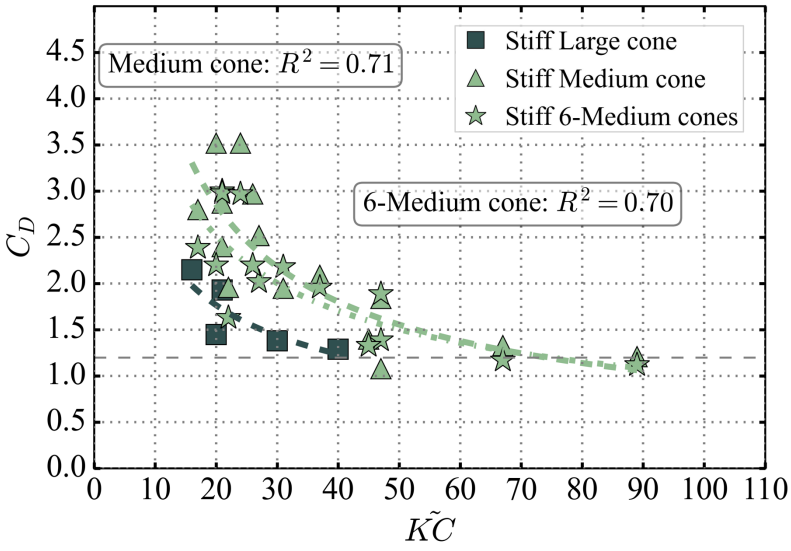

Figure 4.10.: C_D-KC relation for stiff conical shapes. The horizontal grey dashed line illustrates the lower limit of the relation from *Keulegan and Carpenter (1958)*.

Despite this simplification, the drag coefficients obtained can be useful in estimating the expected peak force on flexible conical objects at high *KC* numbers, which is the case for willow branches under extreme wave conditions. The bulk drag coefficients derived from real-scale tests with live pollard willow trees were found to be smaller than 1.2 at high *KC* numbers by *van Wesenbeeck et al. (2022)*. This reduction can be attributed to the flexibility of the canopy under high water levels and wave heights (i.e., high velocities). Nevertheless, their results showed a similar decreasing trend when using the calibration method to obtain C_D.

4.4.4. Cone Deflections

The relation between force (F_p) and deflection of slender tree branches (θ) can be captured by the well-known Euler-Bernoulli beam theory *(Neild and Wood, 1999)*, which can be expressed as follows:

$$\frac{d\phi}{dz} = \frac{M(z)}{EI(z)}, \tag{4.2}$$

where

$$M = \int\int q\,dz = \int F\,dz$$

ϕ is the angular deflection, q is the external load, M is the moment due to the external load, E is the Young's modulus of the material, and I is the moment of inertia. The bending stiffness (EI) represents the restoring force, while q is the external force acting on the object's frontal area along the water depth (i.e., by the wave orbital velocity). The peak force (F_p) on the cone was measured as shown in Section 4.3.1.

Assuming a constant moment (or moment line of constant shape), integrating the equation above yields for the angle at $z = 0.7l$: $\theta(0.7l) \propto Ml_{0.7l}/EI$. The moment will be proportional to $F_p l_{wet}$ (force times arm). Combining these two expressions yields the following hypothesised proportionality for the maximum deflection (θ) at the height of $0.7.l_{cone}$: This assumption is valid for the Large cones since they exhibited relatively small deflections during the experiments. Figure 4.12A confirms a good correlation found for the Large cones using Equation 4.3 with a correlation coefficient $R^2 = 0.94$.

This definition of l_{wet} is applicable for small deflections (specifically $\theta \leq 5°$) when $l_{cone} > h_f$. The initial fit was less suitable for the medium cones, as indicated by an R^2 value of 0.65 (see Figure 4.12B). For large deflections, predominantly observed in these cones, the method for determining the moment arm is inadequate. Investigating whether a 'large-deflection' beam theory (e.g., *Chen, 2010*) can improve the fit for the medium cones is recommended for further analysis.

4.4.5. Force reduction

The reduction of the total peak force due to flexibility effects can be assigned to two aspects, (1) vegetation reconfiguration, which reduces the frontal-area (deflected length) and generally causes a more streamlined shape (*Alben et al., 2004*; *Albayrak et al., 2011*; *Wunder et al., 2011*; *Losada et al., 2016*;), and (2) due to reduced rela-

$$\theta \propto \frac{F_p l_{0.7cone} l_{wet}}{EI}, \qquad (4.3)$$

where

$$l_{wet} = h_f - l_{trunk} + (H/2),$$

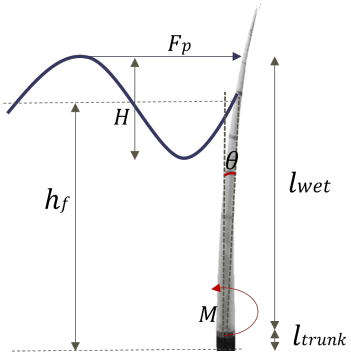

Figure 4.11.: Schematic of the large cone for small deflection and a fully emergent case: $l_{cone} > h_f$.

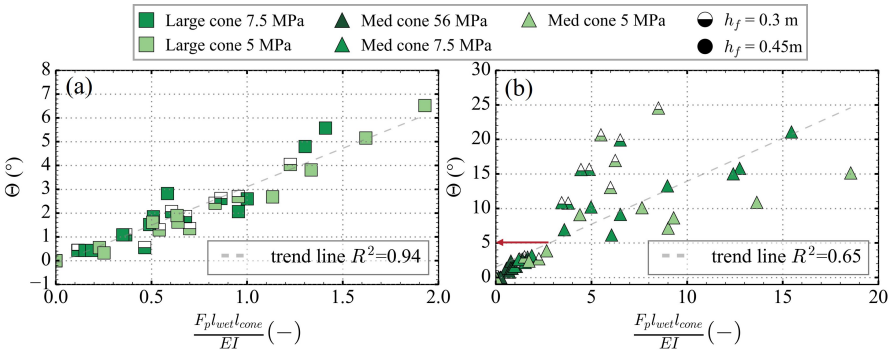

Figure 4.12.: Relation between the measured deflections and the dimensionless number based on the measured peak forces.

tive velocity between the vegetation and the water, which varies along the height of vegetation (*Bradley and Houser, 2009*; *Luhar and Nepf, 2016*; *Lei and Nepf, 2019*).

(A)symmetry and mean position flexible cones

The motion of the 7.5 MPa *Large Cone*, 7.5 MPa *Medium Cone*, and 5 MPa *Medium Cone* are shown as an example in Figure 4.13. The frontal-surface area reduction of

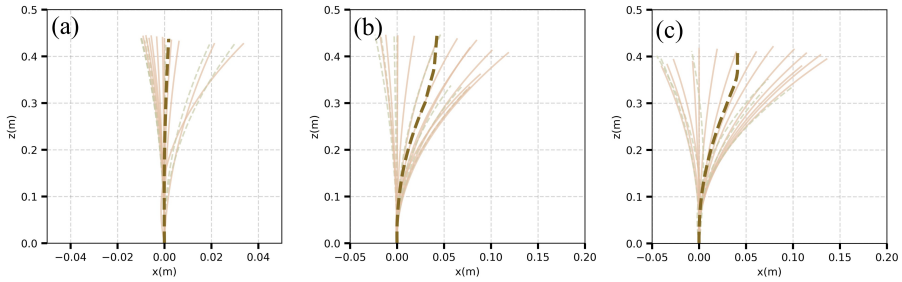

Figure 4.13.: Motion during one wave cycle of test 15: $\{h_f = 0.45$ m; $H = 0.14$ m; $T = 1.23$ s$\}$ for **(a)** 7.5 MPa *Large Cone*, **(b)** 7.5 MPa *Medium Cone*, and **(c)** 5 MPa *Medium Cone*. The thin solid and thin dashed line show forward and backward motion, respectively. The thick dashed line shows the mean position of the cone during one wave cycle.

the Large Cone is negligible as the deflection is ≈ 2 cm ($\theta < 5°$), and the mean position is centred, implying symmetry of the cone movement in time. It can be seen that in contrary to the *Large Cone*, the motion of both medium cones showed to be more asymmetric – leaning towards the direction of the incoming waves. The asymmetry can be due to short period waves, as the flexible stem may have insufficient time to react to changes in short period waves as stated in *Zeller et al. (2014)*. Furthermore, as flexible stems tend to follow the orbital motion of waves, the tip is exposed to a smaller backward velocity (lower in the water column) than the forward orbital velocity (higher up in the water column), which also promotes asymmetry in the direction of wave propagation *(Döbken, 2015)*. Note that at some instances the tip of the cone is missing (e.g., shown in Figure 4.13b,c), because it could not be captured by the current video processing method.

Predicting force reduction

The effective length is a parameter for predicting forces and consequently wave damping in flexible vegetation with a constant diameter, such as idealised salt marsh grasses *(Luhar and Nepf, 2011)*. In the case of trees, which consist of branches with varying diameters, the effective area that contributes to damping becomes more ap-

propriate. The effective area is defined as follows:

$$\frac{A_e}{A} = \frac{F_{p,flex,measured}}{F_{p,rigid,measured}}, \tag{4.4}$$

where $F_{p,flex}$ is the measured peak force on the flexible object, and $F_{p,rigid}$ is the measured peak force on the geometrically equivalent stiff object.

Dimensionless numbers containing the Cauchy number (Ca) and the ratio of vegetation length to wave excursion (L), such as CaL and CaL/KC, have been demonstrated to be effective predictors for the effective length for non-tapered objects (cylindrical or rectangular shapes) under both currents *(Luhar and Nepf, 2011)* and waves (*Luhar and Nepf, 2016*; *Luhar et al., 2017*). For conical shapes, the Ca and L are defined as shown in Equation 4.1.

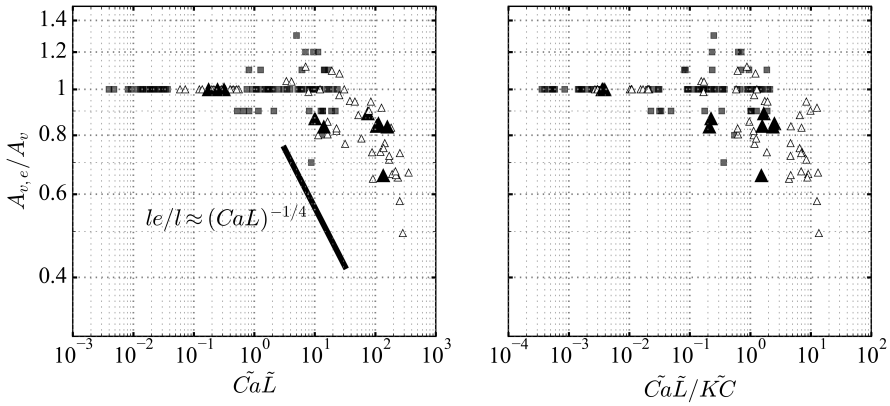

Figure 4.14.: CaL and CaL/KC for predicting the effective area ratio, showing the Large cones (squares) and Medium cones (triangles) for all the tests. The relation $\frac{l_e}{l} \approx (CaL)^{-\frac{1}{4}}$, derived from *Luhar and Nepf (2016)* for sea-grass under wave conditions is shown with the black line.

CaL shows less scatter to predict the effective area compared to CaL/KC. When CaL exceeds 10, a reduction in frontal-surface area and force can be expected, whereas for CaL values less than 10, it can be assumed that the cone exhibits rigid behaviour. These findings are shown in Figure 4.14. Furthermore, our data points show a less steep slope (less severe change in frontal-surface area) than the relation found for sea grass (black line in Figure 4.14).

During typical storm conditions in Dutch riverine areas ($H = 1$ m, $T_p = 5$ s, $h_f = 3$ m), wave orbital velocities can reach up to 1.2 m/s ($\tilde{U}_{max}$). A primary branch of the stiffest willow species (sprouting from a tree knot) can have a Young's modu-

lus (E) of 4500 MPa *(van Starrenburg et al., 2024)*. Considering a typical class 1 branch with a base diameter of 50 mm, a tip diameter of 3 mm (average diameter $\bar{D}$ of $\frac{50+3}{2} = 27$ mm), and a total length of 4 m, the *CaL* is approximately 50, using Equation 4.1. For a less stiff willow species with a Young's modulus of 2000 MPa, the *CaL* would be around 100 for a similar class 1 branch. This indicates that despite the variation in E-modulus between the willow species, the order of magnitude in force reduction remains within the data spread. On the contrary, varying the diameter of the branches while keeping all other properties constant has a larger impact on *CaL*. Smaller diameters (thinner branches) are typical for younger trees, suggesting that canopy age is more important than willow species *(Sutili et al., 2010)*. Still, a younger branch can have a lower *CaL* because it is naturally shorter in length (DBH-length allometric relation). We recommend conducting experiments with live willow branches with varying base diameters to determine the frontal-surface area reduction, with and without side-branches. We expect the tests without the side-branches to follow a trend similar to the results of the conical shapes in this study.

4.5. Conclusions

Our study demonstrated that flexibility significantly influences the forces exerted on, and therefore, the wave damping by pollard willow trees, both in real-scale and scaled tests. The classical $F \propto U^2$ relation was appropriate for relatively stiff trees. However, for flexible and realistic tree mimics, the force-velocity relationship became more linear, particularly under submerged conditions and to a lesser extent under emerged conditions. We designed conical shapes with two different diameter sizes (and hence different moment of inertia $\bar{\mathrm{I}} \approx [1{,}5.10^{-8}; 4{,}2.10^{-10}]$ m^4) and with varying E-moduli ($\mathrm{E} \approx [3200.10^6; 56.10^6; 7{,}5.10^6; 5.10^6]$ $\mathrm{N/m^2}$); and tested (measured deflections and force) these simplified mimics individually under regular wave conditions. The first-mode cone deflection was determined at ≈ 0.7 times the length of the cone to avoid higher-order modes in the measurements. Small deflections (theta$<5°$) could be well captured with the relation based on Euler-Bernoulli ($\theta \propto \frac{\mathrm{F_p l_{wet} l_{cone}}}{\mathrm{EI}}$). On the other hand, cone deflections greater than 5° showed a large spread and resulted in significant decrease in measured forces, with reductions up to 50% compared to their rigid counterpart. Lastly, the *CaL* number showed a strong correlation with the effective surface area for the flexible cones and is a promising indicator for the effective area for conical tree branches.

Photography by Mischa Keijser

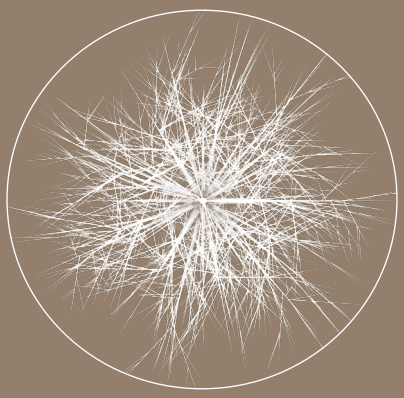

5

Discussion Towards Application

5.1. Introduction

Riparian woodlands – particularly pollard trees – are a unique trait of Dutch rural landscapes and an important habitat for various species *(Cizek et al., 2021)*. In addition, they can also increase the flood safety of the hinterland by dampening incoming waves when (partly) submerged. The safety norms against flooding are becoming stricter in the Netherlands *(Schweckendiek and Slomp, 2018)*. Tighter regulations, along with increases in river discharge and sea level rise (as a consequence of climate change), mean that many dikes will likely need to be reinforced in the upcoming years to meet updated safety standards *(van Loon-Steensma and Schelfhout, 2017)*. Dike reinforcements are costly and require space. Higher and wider dikes will become more difficult to integrate in Dutch landscapes. Implementing existing vegetation or planting additional vegetation in front of the dike can have lower construction costs compared to a dike heightening of 1 m (assuming sufficient space and relatively shallow water) *(Vuik, 2019)*, while also increasing other ecosystem services.

Given the many benefits of floodplains, the EU (e.g., Kaderrichtlijn Water, KRW) and national policies encourage the integration of nature-based solutions in flood risk management plans and emphasise the importance of conserving and restoring floodplain ecosystems where feasible (*Diaz et al., 2019*; *Christiansen et al., 2020*). For instance, the national 'Bossenstrategie' aims to create 2000 hectares of forests along Dutch riverbanks by 2030 (derived from the Programma Aanpak Grote Wateren, PAGW) *(Ministerie van Landbouw Natuur en Voedselkwaliteit, 2020)*. Though attention is required for the successful integration of riparian forests without hindering the river discharge. Projects such as the Room for the River project (a Dutch river management concept) aimed to increase river discharges to sea and, thereby, lowering the flood levels (without rising dike levels). This was achieved by relocation of dikes, depoldering, creating side channels, and removing hydraulic obstacles in rivers such as riparian forests, among other measures *(Silva et al., 2001)*. It is important to note that these programs work together with the Hoogwaterbeschermingsprogramma (HWBP) which focusses on flood safety for 2050, and the Deltaprogramma, whose primary focus points are protecting the country against flooding, sufficient fresh water supply, and to withstand (or adapt) to climate change for 2050.

The suitability of riparian vegetation as part of hybrid flood defences is yet often unclear for practitioners. While guidelines for up-scaling and implementation of nature-based solutions are available (e.g., *Ecoshape, 2024*), quantitative guidelines are still lacking. Due to the many uncertainties related to hybrid flood defences, current dike design procedures recommend excluding the effect of existing riparian

vegetation in the area *(Het Expertise Netwerk Waterkeren, 2007)*. Consequently, traditional dike reinforcement measures, such as raising crest heights or widening dikes, are often the default preference for practitioners – even when they may not be the most cost-effective alternative. However, incorporating existing vegetation into the dike design to delay costly dike renovations could significantly reduce costs in dike reinforcement programmes.

This chapter explores the potential for integrating or preserving riparian woodlands in the Netherlands as a natural flood protection measure. With the insights gained from this thesis, we discuss the effect of vegetation, particularly pollard willow trees, on wave attenuation and how this can be included in probabilistic assessments for dike design. For example, Chapter 2 provided tools, such as the frontal-surface area model of the pollard willow trees and an analytical model to calculate wave damping, which are applied in this discussion chapter. Through a case study in the Netherlands, the practical implications are discussed, demonstrating how pollard willow forests can influence the design of the dikes and enhance the safety assessments of the dikes in the country.

5.2. A Case Study

The impact that a forest can have on the design of the dike is evaluated through a case study area located along the river IJssel near the town of Kampen under Waterschap Drents Overijsselse Delta (WDODelta). Figure 5.1 illustrates the area of interest in front of the dike (trajectory 10-3), which is part of the IJsseldijk that protects the Mastenbroek polder against flooding.

The current dike revetment consists of a grass cover and a bare foreshore (i.e., no forest) in front of the dike. The potential (maximum available) width for a forest to develop is approximately 60-80 m (determined using Google Earth Pro). The level of safety against flooding during the national assessment (occurring every 12 years *(Vergouwe, 2010)*) was not met—specifically for the failure mechanisms of piping, macro-stability, erosion of the grass revetment on the outer slope, and insufficient dike height *(IHW, 2023)*. In the project for the improvement works to reach the reach the required safety standard, WDODelta is looking at different alternatives, with the aim of starting the reinforcement works in 2029. The 'signal value' for this site is 1/10,000 and the 'lower threshold' is 1/3,000 per annum (probability of flooding) *(IHW, 2023)*. The 'signal value' was established because dike reinforcements generally take at least 10 years to complete, and during this time, the flood defence must continue to meet the required protection level (the 'lower threshold') *(Slootjes and*

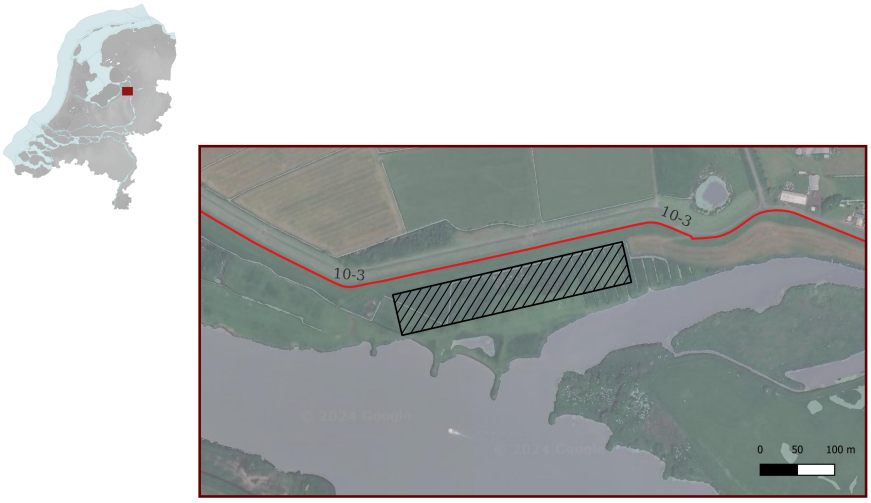

Figure 5.1.: Dike [trajectory 10-3] along the river IJssel, where the black coloured raster shows the potential forest area and the red line indicates the primary dike.

van der Most, 2016).

In the case of hydraulic loads acting on a structure, a forest in front of a levee can decrease wave action (1) by lowering the required crest height, and (2) changing outer-slope and inner-slope revetment (see Figure 5.2). A dike with grass cover is preferred over hard revetments such as asphalt or stone, because (1) it can be cheaper and more sustainable depending on the availability of the materials, and (2) it makes it easier to adapt in the future *(van Loon-Steensma and Schelfhout, 2017)*.

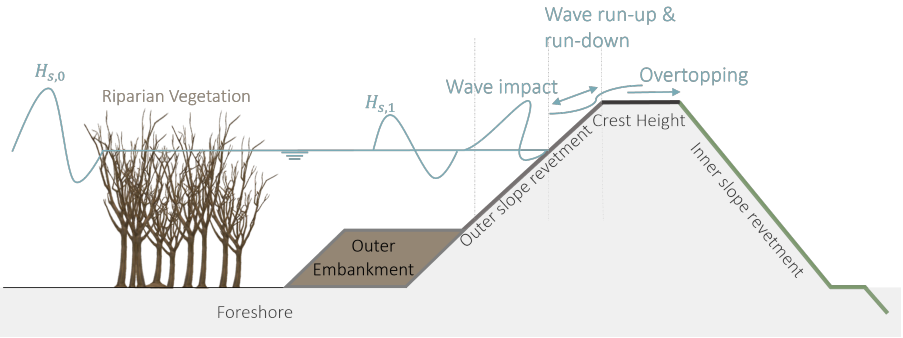

Figure 5.2.: Example of a cross-section of a forest-dike combination.

5.2.1. Deterministic calculation

The hydrodynamic conditions with a 1/10,000-year return frequency are assumed for the calculations of the dike of the dike revetment (inner- and outer-slope) for our case study (dike trajectory 10-3). This design scenario includes a significant wave height H_s of 1.05 m, with a peak period (T_p) of 4 s, and a water level (h) of + 3.34 mNAP, as determined using the Hydra-NL tool [1]. Note that this leads to a conservative design as the input variables are independent from each other. The dike profile used in the analysis was obtained from data from AHN-viewer (Actueel Hoogtebestand Nederland)[2], which was used to find the outer slope (with $\tan\alpha = 0.2$) and the dike crest height (+ 4.25 mNAP). Consequently, the minimum crest freeboard (Rc) was determined as the difference between the crest height and the water level, which has a value of 0.91 m (4.25-3.34 m) *(van der Meer et al., 2018)*. The forest is assumed to be composed of pollard willow trees that are analogous to those tested in *van Wesenbeeck et al. (2022)*. Wave reduction by a potential forest at the case site will be estimated using the implementation of a combination of the layer model of *Suzuki (2011)* and analytical integration of *Mendez and Losada (2004)*. These trees were modelled using six vegetation layers with a frontal surface area distribution based on the 'tree model 2' from Chapter 2. For the bulk drag coefficient, we applied the value for a rigid cylinder, 1.2, but also a value found for flexible willow branches of 0.7 *(van Wesenbeeck et al., 2022)*. A maximum width of 80 metres is available at the site; however, due to tri-annual cutting of the branches of the pollard willows, the entire width will not have a full canopy permanently available. With this is mind, the forest width of 40 m is taken into account in further discussion.

Reduced Wave height

The wave reduction results of varying forest widths and water depths is shown in Figure 5.3. The lower limit of H_s is 0.5 m ($\approx$ 1/100-year return period) and the upper limit of H_s is 1.1 m ($\approx$ 1/10,000-year return period), with a constant peak wave period (T_p) of 4 s, which is a conservative calculation as the expected peak wave period is maximum 3 seconds considering a constant wave steepness for locally generated waves. Wave damping is defined as $\frac{H_0 - H_1}{H_0}$, where H_0 is the incoming wave height and H_1 is the wave height at the toe of the dike; this is calculated for scenarios with and without a forest.

[1] settings: ontwerpmodus for 2050, all uncertainties on, locatie: Dkr 10 IJssel k 992-993 Locatie '1-193440-506070'

[2] ActueelHoogtebestand Nederland is a digital dataset with detailed elevation data for the Netherlands, offering 5 cm accuracy relative to the Amsterdam Ordnance Datum (NAP) *(RWS, 2019)*

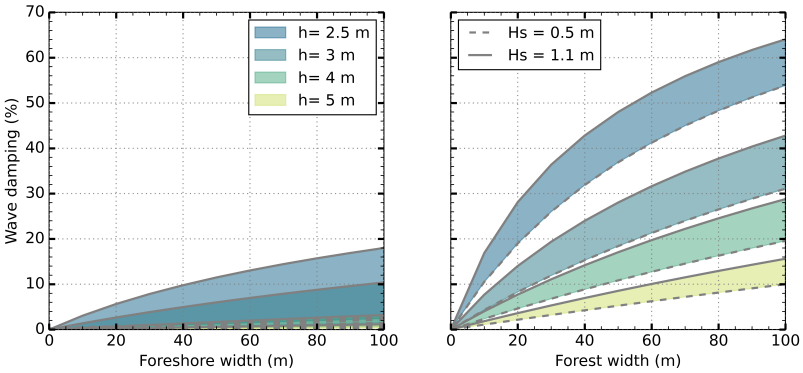

Figure 5.3.: Expected wave damping through various forest widths and water levels combinations. left: wave damping due to a bare foreshore width; right: wave damping due to a foreshore width covered with a forest.

Dike elements

5

We assume the design of the crest height depends on the maximum allowable overtopping discharge (q_{tol}), where an overtopping discharge of 1 l/s/m is initially a standard value to consider for river dikes *(TAW, 2008)*. The maximum allowable discharge depends, among others, on the quality of the inner-slope and crest revetment. For instance, no additional requirements are needed for the resistance against erosion of the inner-slope if a maximum overtopping discharge of 0.1 l/s/m is applied – a sandy inhomogeneous ground with poor quality grass would suffice in this case. If the overtopping discharge is larger than 10 l/s/m, the quality of the revetment should be extremely high paired with high maintenance *(TAW, 2008)* or hard revetment (e.g., grass block pavers, asphalt or stone revetment) can be chosen instead *(Waterkeringen., 1985)*. The overtopping discharge is calculated using the equation in *van der Meer et al. (2018)*, see Appendix E.2. Figure 5.4 shows that a 40-m-long forest can reduce the overtopping discharge such that a moderate grass cover would suffice on the inner slope.

The outer-slope of the dike can erode (fail) due to wave impact and (or) wave run-up (run-down), as calculated with the Gras Buitentalud module *(Deltares, 2019)*. First, erosion due to wave impact is calculated using the formulation for allowed impact duration in Appendix E.2.2, where the top layer and sublayer provide resistance against erosion (failure). The duration of the storm, and therefore the duration of the load (t_{load}) is set to 12 hours *(RWS, 2022)*. Figure 5.5A shows that the wave height of the toe with vegetation makes a clay layer thickness of 0.5 m sufficient to withstand

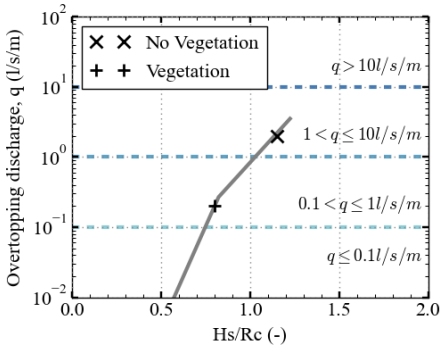

Figure 5.4.: Overtopping discharge without vegetation (cross) and with vegetation (plus) for a 1/10,000 wave height and water depth.

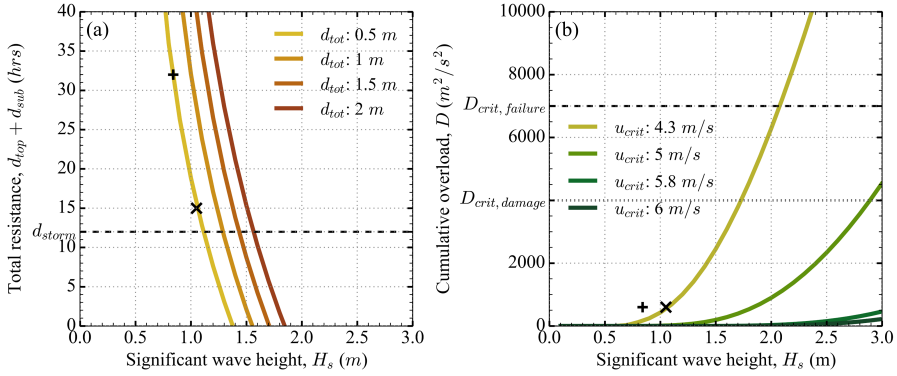

Figure 5.5.: Overtopping discharge without vegetation (cross) and with vegetation (plus), and the grey line indicates the overtopping for a range of wave heights.

wave impact during a 12-hour-long storm, while without vegetation a 1 m thickness of the layer would be more appropriate. Second, wave run-up affects the revetment above the wave impact zone. The load on the dike on the upper slope is quantified by the cumulative overload parameter, D, which is based on the flow velocities over the revetment (see Appendix E.2.3). The critical value of this overload value ($D_{crit,failure}$) depends on the type of revetment. For instance, the resistance against failure for a healthy grass cover is 7000 m^2/s^2 *(Hoven et al., 2013)*. The formulations for obtaining the cumulative overload are shown in Appendix E.2.3. Figure 5.5B shows that the dike can withstand erosion due to wave run-up without vegetation, hence, the forest has no impact on the design regarding wave run-up for the 1/10,000-year wave condition.

5.2.2. Reduced Probability of Flooding

Dikes are designed using reliability methods which can be semi-probabilistic or fully probabilistic. These are linked to the safety levels, which vary across the country; the safety norm per dike trajectory is divided into the probability of failure for different dike failure mechanisms. For instance, the failure budget for revetment failure and erosion is 10% of the total failure probability, where 4,5% is allocated for erosion of the grass revetment *(de Bruijn et al., 2017)*. For instance, the lower limit failure probability allocated for erosion of the grass revetment is $0{,}045 \times 1/3{,}000 = 1{,}5.10^{-5}$ and the signal value is $0{,}045 \times 1/10{,}000 = 4{,}5.10^{-6}$.

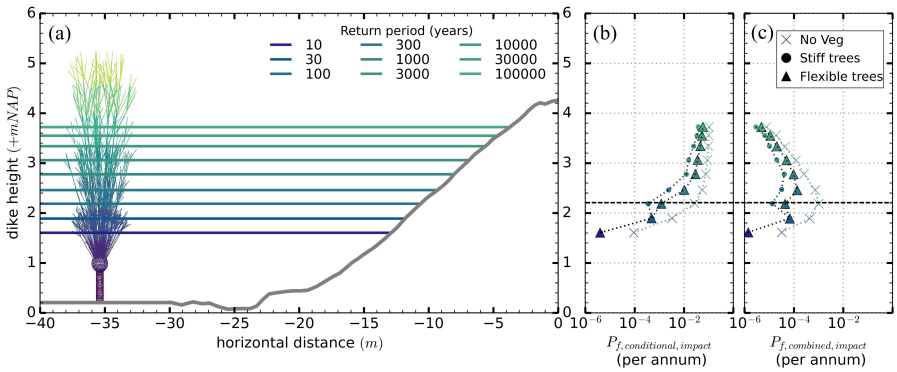

Figure 5.6.: (**a**) Dike cross-section and water elevation levels of varying return periods (1/10 - 1/100,000); (**b**) conditional probability of failure; (**c**) combined probability of failure. (Source: adjusted from *Scheel (2024)*)

A probabilistic study (using Monte Carlo method) has been done on the effect of

vegetation in front of part of the IJssel dike (trajectory $10-3$) *(Scheel, 2024)*. A length-effect parameter of 1 ($N_L = 1$) was assumed for the probabilistic assessments, and the water depths for return periods 1/10 till 1/100,000 (see Figure 5.6A), were determined using Hydra-NL. This probabilistic study showed that the pollard willow forest had most effect on the failure mechanism erosion outer-slope due to wave impact, and not for wave run-up as the hydrodynamic conditions did not lead to severe cumulative overload (as shown in Section 5.2.1); and hence, the probability of failure of the outer-slope revetment due to wave run-up was negligible.

Figure 5.6B shows the conditional probability of failure P(F|h) given the occurrence of the water level, h. The conditional probability of failure is afterwards combined with the marginal probability of occurrence of the specific water level P(h) to determine the combined probability of failure P(F|h)P(h), as shown in Figure 5.6C. Lastly, the total probability of failure due to the outer-slope P_f is calculated by integrating the combined probability of failure curve for wave impact. These results are shown in Figure 5.7 for different scenarios.

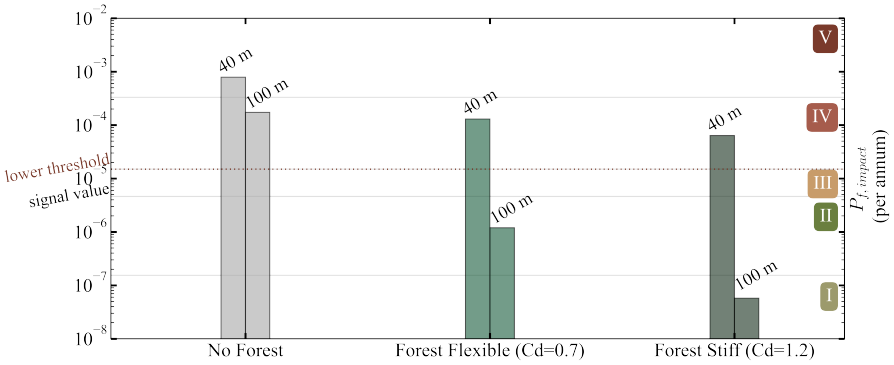

Figure 5.7.: Total probability of failure for wave impact for the different scenarios: 1) no forest for a foreshore width of 40 m and 100 m, 2) forest with 'flexible' trees, and 3) 'stiff' trees for a forest width of 40 m and 100 m. (Source: adjusted from *Scheel (2024)*).

The results in *Scheel (2024)* suggested that the frontal-surface area distribution of vegetation is important in assessing failure probability due to wave impact. This is evident from the observed drop in P_f at the point where the frontal-surface area of the trees reached its maximum around a height of 2 m, as shown by the horizontal dashed line in Figure 5.6. It is also clear that the largest frontal-surface area of the tree, giving most failure probability reduction, is located at the elevation that contributed most to the (unvegetated) probability of failure due to wave impact. Hence, the pollarding

height of trees (that can some extent be chosen freely) seems to be optimal for improving flood safety. Furthermore, the comparison of rigid (C_D= 1.2) and flexible (C_D= 0.7) configurations shows that neglecting flexibility leads to approximately 2-20 times smaller probability of failure estimation, with the largest differences for the wider forest (100 m). These findings also suggest that the discrepancies between scaled and real-scale tests, as shown in Chapter 3), may be less pronounced for relatively small widths. However, as the forest width increases, these discrepancies become more significant, leading to substantial variations in failure probability (P_f). Moreover, the length of the forest (B_f) was identified as a critical parameter. The probability of failure (P_f) for a 40-metre-long forest was calculated to be 10^{-4}, while it decreased to 10^{-6} for a 100-metre-long forest with flexible trees. These variations are significant, as they result in a change in the safety classification of the dike from Level IV (where the dike section meets the alert threshold but does not meet the minimum threshold) to Level II (where the dike section still meets the alert threshold), as illustrated in Figure 5.7. This shift could potentially lead to less heavy (cheaper) outer-slope revetment or postponement for reinforcements.

5.3. Potential Locations

In the previous section, it was shown that the forest width is one of the key parameters for dike-forest solutions. Therefore, it is important to identify locations where the foreshore width is sufficient to support forest growth without conflicting with other objectives, such as increasing roughness in the main discharge channel. This information is valuable during the initial phase of dike reinforcement projects, helping to determine whether dike-vegetation solutions are feasible. The following section will explore potentially suitable locations and provide suggestions for future suitability analysis.

5.3.1. Mapping Willow Forest Locations

Locations with vegetation presence in the Dutch rivers were obtained from the Vegetatielegger *(Rijkswaterstaat, 2024)* – a map with vegetation areas that are categorised using roughness to indicate locations where they do not interfere with the river discharge. The vegetation types ‘Struweel’, ‘Mengklasse 90/10’, and ‘Mengklasse 50/50’ were filtered from this map to calculate the areas where pollard willow trees are allowed to grow. ‘Struweel’ *(shrub)* was the only homogeneous vegetation class selected, because the other types of homogeneous vegetation (namely ‘bos’ *(for-*

est), 'riet' *(reeds)*, and 'gras' *(grass)*) have relatively lower roughness compared to willow species. Furthermore, two mixed vegetation classes were selected, 'Mengklasse 90/10' and 'Mengklasse 50/5', where the vegetation area was multiplied by the maximum allowable area percentage that can contain 'Struweel' vegetation, namely 0.2 and 0.6, respectively (see Appendix E.1 for more information on Vegetatielegger). Furthermore, these vegetation patches were located up to 120 metres in front of a primary dike and were schematised into simple geometries using rectangular shapes (see Figure 5.8 for an example).

The resulting map, with the locations where pollard willow vegetation may grow (and which are close to a primary dike), is shown in Figure 5.9. These locations were categorised as function of their area. This shows that most forests are smaller than 100 m in length (perpendicular to the dike) and there are around 200 sites (5% of all areas) wider (perpendicular to the dike) than 100 m in the Netherlands. Some well-known large nature areas in the Netherlands are for example (1) the Biesbosch area – the largest riparian forest in the Netherlands *(Peters et al., 2021)*; (2) Vossegat in the Grentse Waard, which developed naturally on large sand deposits along the Waal *(Peters et al., 2021)*; (3) Blauwe kamer along the Neder-Rijn near Rhenen, which was a river clay mining area where nature developed *(Silva et al., 2001)*; (4) Duursche Waarden along the IJssel; and (5) Koningsteen along the Maasvallei *(Ministerie van Landbouw Natuur en Voedselkwaliteit, 2008)*. It is important to note that most of the forest locations on the map are part of the Natura 2000-network (protected nature areas).

5.4. Implementation of riparian forests in flood protection system: an Outlook

This chapter highlighted the application potential of water depth for wave attenuation through pollard willow trees. A forest can reduce the probability of dike failure and can be incorporated into probabilistic dike safety assessments, as discussed in Section 5.2.2. These trees are particularly effective in reducing design requirements for water depths that go through the knot of the trees – the location with greatest frontal-surface area. This is also where the least flexible branches are located; however, the change in flexibility for different water levels was not incorporated in the probabilistic assessment. Nonetheless, the probabilistic assessment showed that pollard willow forests, in particular, are expected to have a significant impact on the failure mechanism related to grass erosion on the outer slope due to wave impact. Alternatively,

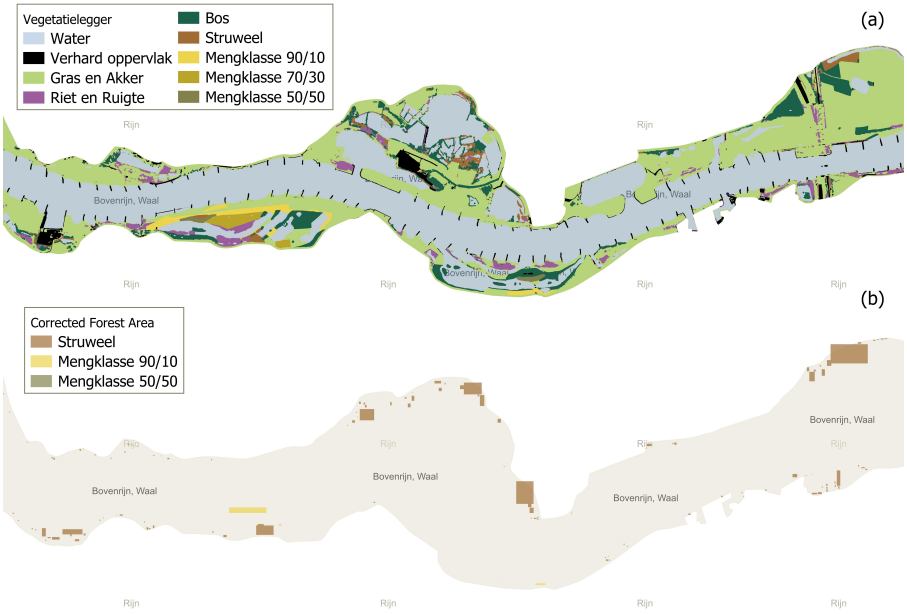

Figure 5.8.: (a) Zoom-in on the Vegetatielegger, and (b) the simplified selected vegetation areas.

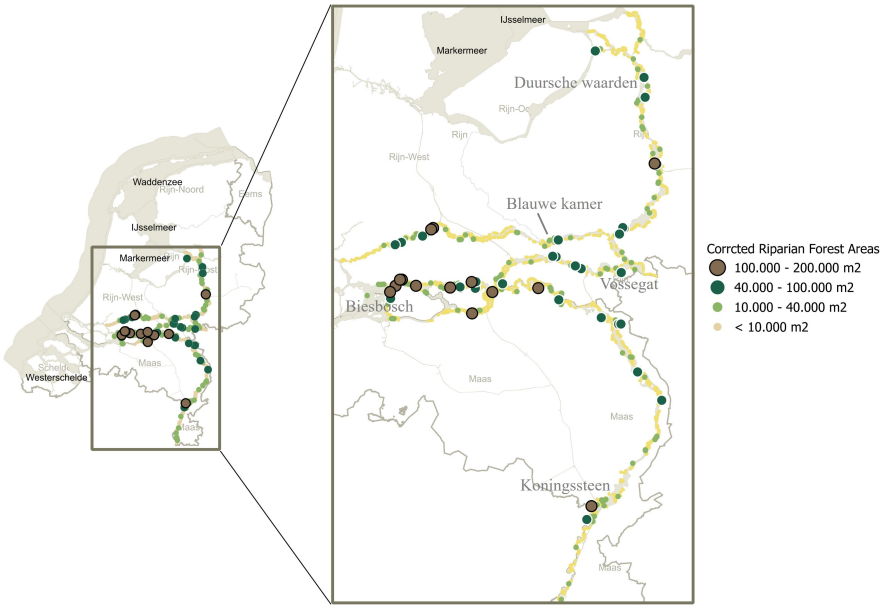

Figure 5.9.: Riparian forests categorised with respect to their area.

optimising the height of the tree's trunk can enhance their effectiveness for different failure mechanisms. For example, in the case a reduction of erosion of the inner-slope of the dike is required (linked to wave overtopping rather than wave impact), a larger trunk height could be more effective than the pollard trees with a 1-meter trunk height used in this study.

Previous studies, particularly those focused on salt marshes, have demonstrated that vegetation can effectively reduce flood risks in areas, depending on the economic stakes *(Vuik, 2019)*. To expand the applicability of riparian forests, future research should explore river dikes and assess additional failure mechanisms, while also investigating how these mechanisms relate to established safety norms. Existing research has already identified several promising locations for implementing dike-vegetation combinations, such as those described in *Penning and Levelt (2017)*. The wave damping model validated through real-scale experiments with pollard willow trees (see Appendix A and Chapter 2) can be used to identify and further explore potential locations for vegetation planting or development. However, as discussed in Section 5.3, many of these promising areas lie within the Natura-2000 network, which is dedicated to the conservation of natural environments and species. This highlights the need to also investigate the role of natural, mixed-species forests. Specifically, further research is required to obtain accurate frontal area (A_v) data for heterogeneous forests and to assess how the variability in A_v influences probabilistic safety assessments. Finally, a life-cycle analysis is essential to ensure that these structures provide the minimum safety standards for their designed lifespan (50+ years). Such an analysis will require more data on the temporal and spatial dynamics of riparian forests. The maintenance approach (such as annual pruning of part of the forest) should also be incorporated in the life-cycle analysis. The experience of the Noordwaard wave damping forest (Figure 1.3) can be used as input for this analysis. Maintenance costs will be lower for a fully natural forest; however, due to the large variation in such a forest, it is expected that larger widths of forest will be required than a designed (homogeneous) forest.

Photography by Mischa Keijser

6.

Conclusions and Recommendations

6.1. Main Findings

Wave damping studies with vegetation are often site-specific and typically result in predictions with large uncertainty. Most of the research is focused on salt marshes (*Mullarney and Henderson, 2010*; *Maza et al., 2015*; *Vuik, 2019*) and aquatic vegetation (*Luhar and Nepf, 2011*; *Gijón Mancheño, 2016*), while research on woody vegetation remains limited. The absence of a widely applicable and practical formulation makes it challenging to extrapolate the findings of these studies to woody vegetation. As a consequence, high safety factors and therefore high costs are associated with hybrid dike-forest combinations for flood protection. The uncertainties related to these hybrid structures need to be decreased; specifically, the uncertainties from our current wave damping predictions through forests need to be improved to promote the use of hybrid dike-vegetation structures in our flood protection systems. This dissertation addresses four key knowledge gaps in its four chapters, aiming to improve the reliability of integrating vegetation into flood risk mitigation strategies. To achieve this, we used data from both **real-scale** and **scaled** (1:10) physical flume experiments. Four main issues were investigated, namely: the lack of studies on the performance of willow trees under storm conditions; the difficulty of accurately determining the frontal-surface area of willow trees; uncertainties related to scaled tests with woody vegetation; and challenges in accounting for the flexibility of woody vegetation in wave damping.

1. How much wave damping through forests can we expect under storm conditions?

There are large uncertainties in the ability of vegetation to dampen waves under extreme conditions due to a lack of real-scale measurements. We tested a 40-m-long willow forest, consisting of 32 trees, in the 300-metre-long Delta flume. The results showed that these trees lead to maximum 20% wave damping without significant damage (i.e., limited loss of frontal surface-area). These tests included maximum wave heights up to 2.5 m – our storm conditions for riverine dikes – and three different tree configurations, namely: 100% canopy density with leaves, without leaves, and 50% canopy density without leaves. The estimated bulk drag coefficient, $\tilde{C_D}$, was lower than 1 for high Reynolds numbers (large water depths with large waves), and these conditions corresponded to large wave forces leading to more branch motion and lower wave damping. The leaves of the willow tree did not contribute significantly to the total amount of wave damping through the forest, but the frontal-surface area distribution relative to water levels proved extremely relevant.

2. How can we obtain reliable vegetation input for current wave damping formulas?

Commonly accepted methods to quantify vegetation by means of a average diameter and density (i.e., $b_v \times N$) in wave models, were not accurate enough to represent real-scale flume tests with live willow trees. Instead, we recommend including the frontal-surface area $A_v(z)$ of the leafless state of willow trees, in wave models. It is also important to include smaller branches and make a more detailed estimation of the surface area than cylinder models are doing. Terrestrial laser scanning techniques are appropriate for this, but suffer from shadowing effects (i.e., blockage of laser beams) due to the density of the canopies. Better estimates of the surface area were achieved by conducting manual measurements in combination with tree allometric relations to map the rather homogeneous willow forest. This technique could be extended to other species and tree ages, and with increased knowledge, the required measurements to reconstruct Av(z) could be reduced. Lastly, the large variation of wave damping outcomes between methods for vegetation mapping showcased the importance of stating the selected method for reliable $A_v(z)$ estimations – and consequently for reliable wave attenuation predictions.

3. What is the potential magnitude of scale or model errors when conducting scaled experiments with woody vegetation?

Most wave damping studies on woody vegetation use data from scaled laboratory experiments. However, data from controlled laboratory scaled experiments are prone to scaling or model errors and comparisons with real-scale tests are lacking for woody vegetation. Here, we conducted scaled tests (1:10) with 3D-printed replicas of willow trees and compared them with real-scale experiments on live trees. The maximum measured wave damping (30%) was 10 percentage points more than the damping found in the real-scale experiments (20%) with live willow trees under storm conditions. Many studies have focused on finding reliable predictive tools using scaled flume tests with vegetation mimics. Scaling down vegetation can however lead to discrepancies with realistic scales, also known as scale errors. These significant deviations illustrated that real-scale experiments, although expensive, are still needed to validate the results of scaled experiments for wave damping through woody vegetation.

4. How can the flexibility effect of woody vegetation be implemented in current wave damping models?

Flexibility is shown to be an important parameter to predict wave attenuation in aquatic vegetation, such as seagrass and kelp. Several studies focused on the flexibility of a single stem or in seagrass meadows, which showed that flexible vegetation introduces less wave damping compared to less flexible vegetation. In the case of woody vegetation, evidence on the role of flexibility of woody vegetation in oscillatory flow is missing, and in numerical models vegetation is often assumed to be rigid, represented in C_D values close to 1. Our study demonstrated that flexibility significantly influences wave damping by woody vegetation. For relatively stiff trees, the classical force-velocity relationship $F \propto U^2$ was effective. However, for the flexible realistic tree mimics, this relationship became more linear, particularly under submerged conditions. We designed and tested conical shapes with varying flexibility, showing that deflections greater than 5 ° resulted in significant force reductions – up to 50% compared to rigid counterparts. Smaller deflections ($\theta < 5°$) could be accurately captured with the quasi-static Euler-Bernoulli relation. Lastly, the CaL number was strongly correlated with the effective surface area of the flexible cones, suggesting it as a promising indicator to implement flexibility effects in wave damping models.

5. Discussion Towards Application

Pollard willow forests in the Netherlands can be used as a (nature-based) solution to reduce wave impact on dikes, thereby lowering flood risk. For a case study location, we predicted by performing multiple Monte Carlo simulations that an effectively 40-m-wide foreshore with willow forest can reduce the failure probability of outer-slope erosion by a factor of ten. The important parameters that came out of the sensitivity analysis were the frontal-surface area, forest width, and flexibility (which was represented by adjusting C_D). We also showed that the height of the trunk (position of the knot and resulting frontal-surface area distribution) can be a design parameter for optimising forest-dike solutions for flood protection. Aspects like long-term performance, including forest maintenance and environmental variability, need to be taken into account.

6.2. Recommendation further research

6.2.1. Future Measurements

Data (i.e., hydrodynamics and vegetation parameters) from real-scale experiments and field experiments (which cover extreme conditions) are crucial to implement dike-forest combinations as flood protection. Field campaigns are highly recommended to collect wave damping data from natural forests, along with data from planted and heavily managed forests (e.g., the vegetation field at Fort Steurgat , the Netherlands). Natural forests are difficult to replicate in flume testing facilities, but are nevertheless important as most floodplains (see Chapter 5) contain diverse vegetation and are nature conservation areas. Besides field data, scaled experiments are still crucial for the fundamental understanding of wave attenuation by woody vegetation, as they serve for more controlled conditions besides being relatively less time consuming and less expensive. For instance, the effect of flexible vegetation on wave damping can be successfully studied in scaled flume studies, especially with improved 3D-printing technologies, which enable the creation of vegetation mimics with varying flexibility (different printing filaments). We recommend studying conical shapes (rather than cylinders) in more detail, as they better capture the characteristics of woody vegetation, particularly the decrease in frontal-surface area and rigidity along the height. However, these conical shapes are simplified, and understanding the role of different order side-branches (i.e., the complexity of the geometry) will be crucial for up-scaling the results to live trees.

Furthermore, to improve predictive wave models, it is important to collect detailed vegetation input parameters, specifically frontal-surface area distributions. We recommend exploring Terrestrial Laser Scanning (TLS) further as a method for vegetation mapping. However, manual measurements remain critical to further refine this technique and develop accurate tree models for common species in riparian forests. These tree models, based on allometric relationships, offer more accurate input for both physical and numerical simulations. Expanding these models to include diverse vegetation types and age classes will require additional data. For example, additional manual measurements on *Salix alba* are needed to enhance existing tree models and extend them to other woody vegetation. This approach has already been successfully applied to mangrove species like *Avicennia* *(Nova, 2022)*, and could also be adapted for other common willow species in the Netherlands, such as *Salix rubens* and *Salix viminalis* *(van Starrenburg et al., 2024)*.

In addition, long-term data collection is essential to track tree growth and understand the evolution of mechanical properties across species. For instance, calibrating allometric relationships for each species by analysing their dependence on easily measurable parameters (such as tree height and diameter at breast height), while accounting for regional and site-specific variations, to provide accurate input for tree models. This requires large-scale data collection across wide geographic areas and over extended time periods. Collaborating with other fields, such as forest management and ecology, which have already collected substantial data on tree growth and long-term survival, could accelerate this process. For example, *van Casteren et al. (2012)* collected and analysed data on branch failure, including *Salix Alba*; and *Schoutens et al. (2024)* gathered on both the shoot scale and on the canopy scale, showing that measurements for these allometric relations are critical for predicting the wave-damping performance of forests. Furthermore, citizen science (engaging the public) could also play a key role in extending data sets in combination with interdisciplinary collaboration. This would not only enhance data collection on tree growth and survival—supporting intensive field campaigns—but also promote a multidisciplinary approach to advance vegetation mapping for dike-forest solutions in flood protection.

6.2.2. Modelling Practices

Modelling wave transformation through vegetation fields requires understanding of key processes, such as wave-vegetation interactions, which can be effectively captured using process-based models. We recommend enhancing existing analytical models by incorporating a flexibility parameter, distinct from the traditional calibration of the drag coefficient (C_D). This parameter, based on the effective area principle (see Chapter 4 Section 4.4), is still based on calibration but provides a more physics-based framework for representing flexible vegetation than the traditional drag coefficient calibration. For practical purposes, the spatial scale of dike-forests solutions suggests that simplified analytical models are well suited for input into probabilistic assessments – a necessary step for implementation within Dutch flood protection systems. Additionally, it is crucial to consider temporal scales by incorporating long-term processes into the models. This includes accounting for vegetation growth, decay, and subsequent impacts on flood protection safety levels over time. Addressing these factors is essential for improving the reliability of long-term flood defence strategies.

REFERENCES

Achenbach, E. (1968). Distribution of local pressure and skin friction around a circular cylinder in cross-flow up to Re = 5:106. *Journal of Fluid Mechanics*, *34*(4), 625–639. https://doi.org/10.1017/S0022112068002120

Albayrak, I., Nikora, V., Miler, O., & O'Hare, M. (2011). Flow-plant interactions at a leaf scale: Effects of leaf shape, serration, roughness and flexural rigidity. *Aquatic Sciences*, *74*(2), 267–286. https://doi.org/10.1007/s00027-011-0220-9

Alben, S., Shelley, M., & Zhang, J. (2004). How flexibility induces streamlining in a two-dimensional flow. *Physics of Fluids*, *16*(5), 1694–1713. https://doi.org/10.1063/1.1668671

Anderson, M., McKee Smith, J., & McKay, S. (2011). Wave Dissipation by Vegetation. *US Army Corps of Engineers*, (8), 14. https://doi.org/ERDC/CHLCHETN-I-82

Antonarakis, A. S., Richards, K. S., Brasington, J., & Bithell, M. (2009). Leafless roughness of complex tree morphology using terrestrial lidar. *Water Resources Research*, *45*(10), 1–14. https://doi.org/10.1029/2008WR007666

Armanini, A., Righetti, M., & Grisenti, P. (2005). Direct measurement of vegetation resistance in prototype scale. *Journal of Hydraulic Research*, *43*(5), 481–487. https://doi.org/10.1080/00221680509500146

Bao, T. Q. (2011). Effect of mangrove forest structures on wave attenuation in coastal Vietnam. *Oceanologia*, *53*(3), 807–818. https://doi.org/10.5697/oc.53-3.807

Best, Ü. S., Van Der Wegen, M., Dijkstra, J., Reyns, J., Van Prooijen, B. C., & Roelvink, D. (2022). Wave attenuation potential, sediment properties and mangrove growth dynamics data over Guyana's intertidal mudflats: Assessing the potential of mangrove restoration works. *Earth System Science Data*, *14*(5), 2445–2462. https://doi.org/10.5194/essd-14-2445-2022

Booij, N., Ris, R. C., & Holthuijsen, L. H. (1999). A third-generation wave model for coastal regions 1. Model description and validation. *Journal of Geophysical Research: Oceans*, *104*(C4), 7649–7666. https://doi.org/10.1029/98JC02622

Borsje, B. W., van Wesenbeeck, B. K., Dekker, F., Paalvast, P., Bouma, T. J., van Katwijk, M. M., & de Vries, M. B. (2011). How ecological engineering can serve in coastal protection. *Ecological Engineering*, *37*(2), 113–122. https://doi.org/10.1016/j.ecoleng.2010.11.027

Bouma, T. J., De Vries, M. B., & Herman, P. M. (2010). Comparing ecosystem engineering efficiency of two plant species with contrasting growth strategies. *Ecology*, *91*(9), 2696–2704. https://doi.org/10.1890/09-0690.1

Bouma, T. J., De Vries, M. B., Low, E., Peralta, G., Tánczos, I. C., Van De Koppel, J., & Herman, P. M. (2005). Trade-offs related to ecosystem engineering: A case study on stiffness of emerging macrophytes. *Ecology*, *86*(8), 2187–2199. https://doi.org/10.1890/04-1588

Bradley, K., & Houser, C. (2009). Relative velocity of seagrass blades: Implications for wave attenuation in low-energy environments. *Journal of Geophysical Research: Earth Surface*, *114*(1), 1–13. https://doi.org/10.1029/2007JF000951

Cavallaro, L., Viviano, A., Paratore, G., & Foti, E. (2018). *Experiments on Surface Waves Interacting with Flexible Aquatic Vegetation* (Vol. 53). https://doi.org/10.1007/s12601-018-0037-8

Chen, L. (2010). An integral approach for large deflection cantilever beams. *International Journal of Non-Linear Mechanics*, *45*(3), 301–305. https://doi.org/10.1016/j.ijnonlinmec.2009.12.004

Chen, Z., Yu, G., Ge, J., Wang, Q., Zhu, X., & Xu, Z. (2015). Roles of climate, vegetation and soil in regulating the spatial variations in ecosystem carbon dioxide fluxes in the Northern Hemisphere. *PLoS ONE*, *10*(4), 1–14. https://doi.org/10.1371/journal.pone.0125265

Cheong, S. M., Silliman, B., Wong, P. P., van Wesenbeeck, B., Kim, C. K., & Guannel, G. (2013). Coastal adaptation with ecological engineering. *Nature Climate Change*, *3*(9), 787–791. https://doi.org/10.1038/nclimate1854

Christiansen, T., Azlak, M., & Ivits-Wasse, E. (2020). *Floodplains: a natural system to preserve and restore* (tech. rep. No. 24/2019).

Cizek, L., Hauck, D., Miklin, J., Platek, M., Kocarek, P., Olsovsky, T., & Sebek, P. (2021). Relict of primeval forests in an intensively farmed landscape: what affects the survival of the hermit beetle (Osmoderma barnabita) (Coleoptera: Scarabaeidae) in pollard willows? *Journal of Insect Conservation*, *25*(3), 407–415. https://doi.org/10.1007/s10841-021-00309-8

Coops, H., Boeters, R., & Smit, H. (1991). Direct and indirect effects of wave attack on helophytes. *Aquatic Botany*, *41*(4), 333–352. https://doi.org/10.1016/0304-3770(91)90052-7

Costanza, R., D'Arge, R., de Groot, R., Farber, S., Grasso, M., Hannon, B., Limburg, K., Naeem, S., O'Neill, R. V., Paruelo, J., Raskin, R. G., Sutton, P., & van den Belt, M. (1997). The value of the world's ecosystem services and natural capital. LK - https://royalroads.on.worldcat.org/oclc/4592801201. *Nature TA - TT -*, *387*(6630), 253–260. https://www-nature-com.ezproxy.royalroads.ca/articles/387253a0.pdf

Dalrymple, R. A., Kirby, J. T., & Hwang, P. A. (1984). Wave diffraction due to areas of energy dissipation. *Journal of Waterway, Port, Coastal and Ocean Engineering*, *110*(1), 67–79. https://doi.org/10.1061/(ASCE)0733-950X(1984)110:1(67)

de Bruijn, H., de Vries, G., & 't Hart, R. (2017). *Voorschrift Toetsen op Veiligheid , Technisch Deel* (tech. rep. No. Wti). Deltares.

de Langre, E. (2008). Effects of Wind on Plants. *Annual Review of Fluid Mechanics*, *40*(1), 141–168. https://doi.org/10.1146/annurev.fluid.40.111406.102135

de Waal, J., & van Hoven, A. (2015). *Failure Mechanism Module Grass Wave Runup Zone Requirements and Functional Design* (tech. rep.). Deltares.

Deltares. (2019). *WBI 2017: BM-Gras buitentalud* (tech. rep.). RWS.

Diaz, S., Settele, J., Brondizio, E., Ngo, H., Gueze, M., Agard, J., Arneth, A., Balvanera, P., Brauman, K., Butchart, S., Chan, K., Garibaldi, L., Ichii, K., Liu, J., Subramanian, S., Midgley, G., Miloslavich, P., Molnar, Z., Obura, D., … Zayas, C. (2019). *IPBES: Summary for policymakers of the global assessment report on biodiversity and ecosystem services* (M. da Cunha, G. Mace, & H. Mooney, Eds.; tech. rep. No. 3). Bonn, Germany, IPBES Secretariat. https://zenodo.org/record/3553579#.YfmYTerMI2w

Döbken, J. W. D. (2015). *Modeling the interaction of wave hydrodynamics with flexible aquatic vegetation* [Doctoral dissertation]. http://citeseerx.ist.psu.edu/viewdoc/download?doi=10.1.1.970.1539&rep=rep1&type=pdf

Ecoshape. (2024). Building with Nature. https://www.ecoshape.org/en/

EJF. (2006). MANGROVES : Nature's defence against TSUNAMIS- A report on the impact of mangrove loss and shrimp farm development on coastal defences. Environmental Justice Foundation, London, UK.

Etminan, V., Lowe, R. J., & Ghisalberti, M. (2019). Canopy resistance on oscillatory flows. *Coastal Engineering*, *152*, 11–12. https://doi.org/10.1016/j.coastaleng.2019.04.014

Fenton, J. D. (1985). A fifth-order stokes theory for steady waves. *1*(2), 216–234.

Fu, H., Zhang, Y., Ao, X., Wang, W., & Wang, M. (2019). High surface elevation gains and prediction of mangrove responses to sea-level rise based on dynamic surface elevation changes at Dongzhaigang Bay, China. *Geomorphology*, *334*, 194–202. https://doi.org/10.1016/j.geomorph.2019.03.012

Gedan, K. B., Kirwan, M. L., Wolanski, E., Barbier, E. B., & Silliman, B. R. (2011). The present and future role of coastal wetland vegetation in protecting shorelines: Answering recent challenges to the paradigm. *Climatic Change*, *106*(1), 7–29. https://doi.org/10.1007/s10584-010-0003-7

Gijón Mancheño, A., Jansen, W., Uijttewaal, W. S., Reniers, A. J., van Rooijen, A. A., Suzuki, T., Etminan, V., & Winterwerp, J. C. (2021). Wave transmission and drag coefficients through dense cylinder arrays: Implications for designing structures for mangrove restoration. *Ecological Engineering*, *165*(April). https://doi.org/10.1016/j.ecoleng.2021.106231

Gijón Mancheño, A. (2016). Interaction between wave hydrodynamics and flexible vegetation, 92.

Granek, E., & Ruttenberg, B. I. (2008). Changes in biotic and abiotic processes following mangrove clearing. *Estuarine, Coastal and Shelf Science*, *80*(4), 555–562. https://doi.org/10.1016/j.ecss.2008.09.012

Hasselmann, K., & Collins, J. (1968). Spectral Dissipation of Finite-depth Gravity Waves Due to Turbulent Bottom Friction. *Journal of Marine Research*, (203), 77–85. https://doi.org/10.1016/b978-0-408-70700-8.50018-5

He, F., Chen, J., & Jiang, C. (2019). Surface wave attenuation by vegetation with the stem, root and canopy. *Coastal Engineering*, *152*(December 2017), 103509. https://doi.org/10.1016/j.coastaleng.2019.103509

Heller, V. (2011). Scale effects in physical hydraulic engineering models. *Journal of Hydraulic Research*, *49*(3), 293–306. https://doi.org/10.1080/00221686.2011.578914

Heller, V. (2017). Self-similarity and Reynolds number invariance in Froude modelling. *Journal of Hydraulic Research*, *55*(3), 293–309. https://doi.org/10.1080/00221686.2016.1250832

Het Expertise Netwerk Waterkeren, E. (2007). *Ontwerpbelastingen voor het rivierengebied* (tech. rep.).

Hong, L., Cheng, S., Houseago, R. C., Parsons, D. R., Best, J. L., & Chamorro, L. P. (2022). On the submerged low-Cauchy-number canopy dynamics under unidirectional flows. *Journal of Fluids and Structures*, *113*, 103646. https://doi.org/10.1016/j.jfluidstructs.2022.103646

Horstman, E. M., Dohmen-Janssen, C. M., Narra, P. M., van den Berg, N. J., Siemerink, M., & Hulscher, S. J. (2014). Wave attenuation in mangroves: A quantitative approach to field observations. *Coastal Engineering*, *94*, 47–62. https://doi.org/10.1016/j.coastaleng.2014.08.005

Horstman, E. M. (2014). *the Mangrove Tangle Short-Term Bio-Physical Interactions in Coastal Mangroves*. https://doi.org/10.3990/1.9789036536509

Hoven, A. V., Verheij, H., Hoffmans, G., & Meer, J. V. D. (2013). *Evaluation and Model Development: grass erosion test at the Rhine dike* (tech. rep.).

Hu, Z., Suzuki, T., Zitman, T., Uittewaal, W., & Stive, M. (2014). Laboratory study on wave dissipation by vegetation in combined current-wave flow. *Coastal Engineering*, *88*(June), 131–142. https://doi.org/10.1016/j.coastaleng.2014.02.009

Huang, Z., Yao, Y., Sim, S. Y., & Yao, Y. (2011). Interaction of solitary waves with emergent, rigid vegetation. *Ocean Engineering*, *38*(10), 1080–1088. https://doi.org/10.1016/j.oceaneng.2011.03.003

Hughes, S. A. (1993). Laboratory wave reflection analysis using co-located gages. *Coastal Engineering*, *20*(3-4), 223–247. https://doi.org/10.1016/0378-3839(93)90003-Q

IFRCRCS. (2014). *Mangrove plantation in Viet Nam: measuring impact and cost benefit* (tech. rep.). Vietnam Red Cross. https://doi.org/10.1596/978-1-4648-0314-7{_}ch3

IHW. (2023). Kaartbeelden [accessed in August 2024]. %7Bhttps://waterveiligheidsportaal.nl/nss/prognosis%7D

Infantes, E., Orfila, A., Simarro, G., Terrados, J., Luhar, M., & Nepf, H. (2012). Effect of a seagrass (Posidonia oceanica) meadow on wave propagation. *Marine Ecology Progress Series*, *456*, 63–72. https://doi.org/10.3354/meps09754

IPCC. (2022). Synthesis report - Climate change 2023. *An Assessment of the Intergovernmental Panel on Climate Change*, *335*(7633), 1318.

Ismail, H., Abd Wahab, A. K., & Alias, N. E. (2012). Determination of mangrove forest performance in reducing tsunami run-up using physical models. *Natural Hazards*, *63*(2), 939–963. https://doi.org/10.1007/s11069-012-0200-y

Jacobsen, N. G., Bakker, W., Uijttewaal, W. S., & Uittenbogaard, R. (2019). Experimental investigation of the wave-induced motion of and force distribution along a flexible stem. *Journal of Fluid Mechanics*, 1036–1069. https://doi.org/10.1017/jfm.2019.739

Jadhav, R. S., & Chen, Q. (2012). Field Investigation of Wave Dissipation Over Salt Marsh Vegetation During Tropical Cyclone. *Coastal Engineering Proceedings*, *1*(33), 41. https://doi.org/10.9753/icce.v33.waves.41

Jadhav, R. S., Chen, Q., & Smith, J. M. (2013). Spectral distribution of wave energy dissipation by salt marsh vegetation. *Coastal Engineering*, *77*, 99–107. https://doi.org/10.1016/j.coastaleng.2013.02.013

Järvelä, J. (2004). Determination of flow resistance caused by non-submerged woody vegetation. *International Journal of River Basin Management*, *2*(1), 61–70. https://doi.org/10.1080/15715124.2004.9635222

Jonkman, S. N., Hillen, M. M., Nicholls, R. J., Kanning, W., & Van Ledden, M. (2013). Costs of adapting coastal defences to sea-level rise - New estimates and their implications. *Journal of Coastal Research*, *29*(5), 1212–1226. https://doi.org/10.2112/JCOASTRES-D-12-00230.1

Kalloe, S. A., Hofland, B., Antolínez, J., & van Wesenbeeck, B. K. (2022a). Quantifying Frontal-Surface Area of Woody Vegetation: A Crucial Parameter for Wave Attenuation. *Frontiers in Marine Science*, *9*(March), 1–18. https://doi.org/10.3389/fmars.2022.820846

Kalloe, S. A., Hofland, B., & van Wesenbeeck, B. K. (2022b). Development of Scaled Tree Mimics for Wave Damping. *39th IAHR World Congress*, (June), 2618–2625. https://doi.org/https://doi.org/10.3850/IAHR-39WC2521711920221137

Kalloe, S. A., Hofland, B., & van Wesenbeeck, B. K. (2024). Scaled versus real-scale tests: Identifying scale and model errors in wave damping through woody vegetation. *Ecological Engineering*, *202*(November 2023), 107241. https://doi.org/10.1016/j.ecoleng.2024.107241

Karrenberg, S., Edwards, P. J., & Kollmann, J. (2002). The life history of Salicaceae living in the active zone of floodplains. *Freshwater Biology*, *47*(4), 733–748. https://doi.org/10.1046/j.1365-2427.2002.00894.x

Kelty, K., Tomiczek, T., Cox, D. T., Lomonaco, P., & Mitchell, W. (2022). Prototype-Scale Physical Model of Wave Attenuation Through a Mangrove Forest of Moderate Cross-Shore Thickness: LiDAR-Based Characterization and Reynolds Scaling for Engineering With Nature. *Frontiers in Marine Science*, *8*(January), 1–18. https://doi.org/10.3389/fmars.2021.780946

Keulegan, G., & Carpenter, L. (1958). Forces on Cylinders and Plates in an Oscillating Fluid. *American Society of Mechanical Engineers (Paper)*, *60*(75 -APMW-27).

Kirkegaard, J., Wolters, G., Sutherland, J., Soulsby, R., Frostick, L., Mclelland, S., Mercer, T., & Gerritsen, H. (2011). *IAHR Design Manual: Users Guide to Physical Modelling and Experimentation*. https://doi.org/10.1201/b11335

Klopman, G., & Meer, J. W. v. d. (1999). Random Wave Measurements in Front of Reflective Structures. *Journal of Waterway, Port, Coastal, and Ocean Engineering*, *125*(1), 39–45. https://doi.org/10.1061/(asce)0733-950x(1999)125:1(39)

Kobayashi, N., Raichle, A., & Asano, T. (1993). Wave attenuation by vegetation. *J. Waterway, Port, Coastal, Ocean Eng*, *119*(1), 30–48.

Koch, E. W., Barbier, E. B., Silliman, B. R., Reed, D. J., Perillo, G. M., Hacker, S. D., Granek, E. F., Primavera, J. H., Muthiga, N., Polasky, S., Halpern, B. S., Kennedy, C. J., Kappel, C. V., & Wolanski, E. (2009). Non-linearity in ecosystem services: Temporal and spatial variability in coastal protection. *Frontiers in Ecology and the Environment*, *7*(1), 29–37. https://doi.org/10.1890/080126

Le Mehaute, B. (1976). *An Introduction to hydrodynamics and water waves* (Vol. 21). Springer.

Leclercq, T., & de Langre, E. (2016). Drag reduction by elastic reconfiguration of non-uniform beams in non-uniform flows. *Journal of Fluids and Structures*, *60*, 114–129. https://doi.org/10.1016/j.jfluidstructs.2015.10.007

Lei, J., & Nepf, H. (2021). Evolution of flow velocity from the leading edge of 2-D and 3-D submerged canopies. *Journal of Fluid Mechanics*, *916*, 1–27. https://doi.org/10.1017/jfm.2021.197

Lei, J., & Nepf, H. (2019). Wave damping by flexible vegetation: Connecting individual blade dynamics to the meadow scale. *Coastal Engineering*, *147*(February 2018), 138–148. https://doi.org/10.1016/j.coastaleng.2019.01.008

Losada, I. J., Maza, M., & Lara, J. L. (2016). A new formulation for vegetation-induced damping under combined waves and currents. *Coastal Engineering*, *107*, 1–13. https://doi.org/10.1016/j.coastaleng.2015.09.011

Luhar, M., Infantes, E., & Nepf, H. (2017). Journal of Geophysical Research : Oceans. *Journal of Geophysical Research: Oceans*, *122*, 2647–2651. https://doi.org/10.1002/2017JC012961.Received

Luhar, M., & Nepf, H. M. (2016). Wave-induced dynamics of flexible blades. *Journal of Fluids and Structures*, *61*, 20–41. https://doi.org/10.1016/j.jfluidstructs.2015.11.007

Luhar, M., Coutu, S., Infantes, E., Fox, S., & Nepf, H. (2010). Wave-induced velocities inside a model seagrass bed. *Journal of Geophysical Research: Oceans*, *115*(12), 1–15. https://doi.org/10.1029/2010JC006345

Luhar, M., & Nepf, H. M. (2011). Flow-induced reconfiguration of buoyant and flexible aquatic vegetation. *Limnology and Oceanography*, *56*(6), 2003–2017. https://doi.org/10.4319/lo.2011.56.6.2003

Mansard, E., & Funke, E. (1980). The Measurement of Incident and Reflected Spectra Using a Least Squares Method.

Massel, S. R., & Brinkman, R. M. (1998). On the determination of directional wave spectra for practical applications. *Applied Ocean Research*, *20*(6), 357–374. https://doi.org/10.1016/S0141-1187(98)00026-1

Maza, M., Lara, J. L., Losada, I. J., Ondiviela, B., Trinogga, J., & Bouma, T. J. (2015). Large-scale 3-D experiments of wave and current interaction with real vegetation. Part 2: Experimental analysis. *Coastal Engineering*, *106*, 73–86. https://doi.org/10.1016/j.coastaleng.2015.09.010

Maza, M., Adler, K., Ramos, D., Garcia, A. M., & Nepf, H. (2017a). Velocity and Drag Evolution From the Leading Edge of a Model Mangrove Forest. *Journal of Geophysical Research: Oceans*, *122*(11), 9144–9159. https://doi.org/10.1002/2017JC012945

Maza, M., Adler, K., Ramos, D., Garcia, A. M., & Nepf, H. (2017b). Velocity and Drag Evolution From the Leading Edge of a Model Mangrove Forest. *Journal of Geophysical Research: Oceans*, *122*(11), 9144–9159. https://doi.org/10.1002/2017JC012945

Maza, M., Lara, J. L., & Losada, I. J. (2019). Experimental analysis of wave attenuation and drag forces in a realistic fringe Rhizophora mangrove forest. *Advances in Water Resources*, *131*(July), 103376. https://doi.org/10.1016/j.advwatres.2019.07.006

Mazda, Y., Magi, M., Ikeda, Y., Kurokawa, T., & Asano, T. (2006). Wave reduction in a mangrove forest dominated by Sonneratia sp. *Wetlands Ecology and Management*, *14*(4), 365–378. https://doi.org/10.1007/s11273-005-5388-0

McMahon, T. A., & Kronauer, R. E. (1976). Tree structures: Deducing the principle of mechanical design. *Journal of Theoretical Biology*, *59*(2), 443–466. https://doi.org/10.1016/0022-5193(76)90182-X

Mendez, F., & Losada, I. (2004). An empirical model to estimate the propagation of random breaking and nonbreaking waves over vegetation fields. *Coastal Engineering*, *51*(2), 103–118. https://doi.org/10.1016/j.coastaleng.2003.11.003

Mendez, F., Losada, I. J., Dalrymple, R. A., & Losada, M. (1998). Effects of wave reflection and dissipation on wave-induced second order magnitudes. *Coastal Engineering*, 537–550.

Ministerie van Landbouw Natuur en Voedselkwaliteit. (2008). *Ontwerpbesluit Grensmaas* (tech. rep.).

Ministerie van Landbouw Natuur en Voedselkwaliteit. (2020). *Bos voor de toekomst* (tech. rep.).

Möller, I., Kudella, M., Rupprecht, F., Spencer, T., Paul, M., van Wesenbeeck, B. K., Wolters, G., Jensen, K., Bouma, T. J., Miranda-Lange, M., & Schimmels, S. (2014). Wave attenuation over coastal salt marshes under storm surge conditions. *Nature Geoscience*, *7*(10), 727–731. https://doi.org/10.1038/NGEO2251

Morison, J. R., Johnson, J. W., & Schaaf, S. A. (1950). The Force Exerted by Surface Waves on Piles. *Journal of Petroleum Technology*, *2*(05), 149–154. https://doi.org/10.2118/950149-G

Mullarney, J. C., & Henderson, S. M. (2010). Wave-forced motion of submerged single-stem vegetation. *Journal of Geophysical Research: Oceans*, *115*(12), 1–14. https://doi.org/10.1029/2010JC006448

Nainar, A., Tanaka, N., Sato, T., Mizuuchi, Y., & Kuraji, K. (2021). A comparison of hydrological characteristics between a cypress and mixed-broadleaf forest: Implication on water resource and floods. *Journal of Hydrology*, *595*, 125679. https://doi.org/10.1016/j.jhydrol.2020.125679

Narayan, S., Suzuki, T., Stive, M., Verhagen, H., Ursem, W., & Ranasinghe, R. (2011). ON THE EFFECTIVENESS OF MANGROVES IN ATTENUATING CYCLONE – INDUCED WAVES. *Coastal Engineering*, *53*(9), 1689–1699.

National Research Council (U.S.) (1999). *Review of the Need for a Large-scale Test Facility for Research on the Effects of Extreme Winds on Structures*. National Academy Press.

Neild, S. A., & Wood, C. J. (1999). Estimating stem and root-anchorage flexibility in trees. (1989).

Nepf, H. M. (1999). Drag, turbulence, and diffusion in flow through emergent vegetation. *Water Resources Research*, *35*(2), 479–489. https://doi.org/10.1029/1998WR900069

Nordh, N. E., & Verwijst, T. (2004). Above-ground biomass assessments and first cutting cycle production in willow (Salix sp.) coppice - A comparison between destructive and non-destructive methods. *Biomass and Bioenergy*, *27*(1), 1–8. https://doi.org/10.1016/j.biombioe.2003.10.007

Norris, B. K., Mullarney, J. C., Bryan, K. R., & Henderson, S. M. (2017). The effect of pneumatophore density on turbulence: A field study in a Sonneratia-dominated mangrove forest, Vietnam. *Continental Shelf Research*, *147*(May), 114–127. https://doi.org/10.1016/j.csr.2017.06.002

Nova, K. F. J. (2022). *Geometrical Mangrove Models* (tech. rep.). TU Delft. Delft.

Ohira, W., Honda, K., Nagai, M., & Ratanasuwan, A. (2013). Mangrove stilt root morphology modeling for estimating hydraulic drag in tsunami inundation simulation. *Trees - Structure and Function*, *27*(1), 141–148. https://doi.org/10.1007/s00468-012-0782-8

Oppenheimer, M., Glavovic, B., Hinkel, J., van de Wal, R., Magnan, A., Abd-Elgawad, A., Cai, R., Cifuentes-Jara, M., DeConto, R., Ghosh, T., Hay, J., Isla, F., Marzeion, B., Meyssignac, B., & Sebesvari, Z. (2019, January). *Sea Level Rise and Implications for Low-Lying Islands, Coasts and Communities* (tech. rep.). https://doi.org/https://doi.org/10.1017/9781009157964.012

Ozeren, Y., Wren, D. G., & Wu, W. (2014). Experimental investigation of wave attenuation through model and live vegetation. *Journal of Waterway, Port, Coastal and Ocean Engineering*, *140*(5), 1–12. https://doi.org/10.1061/(ASCE)WW.1943-5460.0000251

Penning, E., & Levelt, O. (2017). *Quickscan effect vegetatie in voorlanden op golfbelasting* (tech. rep.).

Peters, B., Bijlsma, R., & Maas, G. (2021). Ooibossen. Van 'Ooievaar' tot 'Stroomlijn', en verder. https://edepot.wur.nl/544807

Peters, B., Kater, E., & Geerling, G. (2006). Cyclisch beheer in de uiterwaarden.

Phan, K. L., Stive, M. J., Zijlema, M., Truong, H. S., & Aarninkhof, S. G. (2019). The effects of wave non-linearity on wave attenuation by vegetation. *Coastal Engineering*, *147*(January), 63–74. https://doi.org/10.1016/j.coastaleng.2019.01.004

Phuoc, V. L. H., & Massel, S. R. (2006). Experiments on wave motion and suspended sediment concentration at Nang Hai, Can Gio mangrove forest, Southern Vietnam. *Oceanologia*, *48*(1), 23–40.

Quartel, S., Kroon, A., Augustinus, P. G., Van Santen, P., & Tri, N. H. (2007). Wave attenuation in coastal mangroves in the Red River Delta, Vietnam. *Journal of Asian Earth Sciences*, *29*(4), 576–584. https://doi.org/10.1016/j.jseaes.2006.05.008

Riis, T., Kelly-Quinn, M., Aguiar, F. C., Manolaki, P., Bruno, D., Bejarano, M. D., Clerici, N., Fernandes, M. R., Franco, J. C., Pettit, N., Portela, A. P., Tammeorg, O., Tammeorg, P., Rodríguez-González, P. M., & Dufour, S. (2020). Global overview of ecosystem services provided by riparian vegetation. *BioScience*, *70*(6), 501–514. https://doi.org/10.1093/biosci/biaa041

Rijkswaterstaat. (2024). vegetatielegger. https://geoweb.rijkswaterstaat.nl/ModuleViewer/?app=988a774e44ba4a3084e721d95c4b49a5

Rog, S. M., Clarke, R. H., & Cook, C. N. (2017). More than marine: revealing the critical importance of mangrove ecosystems for terrestrial vertebrates. *Diversity and Distributions*, *23*(2), 221–230. https://doi.org/10.1111/ddi.12514

RWS. (2019). AHN viewer. https://www.ahn.nl/ahn-viewer

RWS. (2022). *WBI2017: Schematiseringshandleiding Grasbekleding* (tech. rep.). Rijkswaterstaat, water verkeer en leefomgeving. https://www.helpdeskwater.nl/onderwerpen/waterveiligheid/primaire/beoordelen/@205746/schematiseringshandleiding-grasbekleding/

Scheel, B. T. F. (2024). *Test the potential of using riparian forests to attenuate wave load and optimize dike design* [Doctoral dissertation, Delft University of technology].

Schoutens, K., Silinski, A., Belliard, P., Bouma, T. J., Temmerman, S., & Schoelynck, J. (2024). Wave attenuation by intertidal vegetation is mediated by trade- offs between shoot- and canopy- scale plant traits. *Journal of Applied Ecology*, *00*(January), 1–10. https://doi.org/10.1111/1365-2664.14765

Schuerch, M., Spencer, T., Temmerman, S., Kirwan, M. L., Wolff, C., Lincke, D., McOwen, C. J., Pickering, M. D., Reef, R., Vafeidis, A. T., Hinkel, J., Nicholls, R. J., & Brown, S. (2018). Future response of global coastal wetlands to sea-level rise. *Nature*, *561*(7722), 231–234. https://doi.org/10.1038/s41586-018-0476-5

Schweckendiek, T., & Slomp, R. (2018). Risk-based safety standards and safety assessment tools in the Netherlands. *41th Dresdner Wasserbaukolloquium 2018: Wasserbauwerke im Bestand-Sanierung, Umbau, Ersatzneubau und Rückbau*, *S*(60), 33–44. https://tu-dresden.de/bu/bauingenieurwesen/iwd/wasserbaukolloquium/historie/kolloquium2018

Shepard, C. C., Crain, C. M., & Beck, M. W. (2011). The protective role of coastal marshes: A systematic review and meta-analysis. *PLoS ONE*, *6*(11). https://doi.org/10.1371/journal.pone.0027374

Silva, W., Klijn, F., & Dijkman, J. (2001). *Room for the Rhine Branches in the Netherlands: What the research has taught us* (tech. rep.). https://www.researchgate.net/publication/269406166_Room_for_the_Rhine_Branches_in_The_Netherlands_What_the_research_has_taught_us

Slootjes, N., & van der Most, H. (2016). *Achtergronden bij de normering van de primaire waterkeringen in Nederland - Hoofdrapport* (tech. rep.). Ministerie van Infrastructuur en Milieu.

Sonnenwald, F., Stovin, V., & Guymer, I. (2019). Estimating drag coefficient for arrays of rigid cylinders representing emergent vegetation. https://doi.org/10.1080/00221686.2018.1494050

Srinivasan, S., Popescu, S. C., Eriksson, M., Sheridan, R. D., & Ku, N. W. (2014). Multi-temporal terrestrial laser scanning for modeling tree biomass change. *Forest Ecology and Management*, *318*, 304–317. https://doi.org/10.1016/j.foreco.2014.01.038

Stratigaki, V., Manca, E., Prinos, P., Losada, I. J., Lara, J. L., Sclavo, M., Amos, C. L., Cáceres, I., & Sánchez-Arcilla, A. (2011). Large-scale experiments on wave propagation over Posidonia oceanica. *Journal of Hydraulic Research*, *49*(SUPPL.1), 31–43. https://doi.org/10.1080/00221686.2011.583388

Sumer, B., & Fredsoe, J. (1998, March). *Hydrodynamics around cylindrical structures* (P. L. F. Liu, Ed.; Vol. 26). World Scientific Publishing Co. Pte. Ltd. https://doi.org/10.1016/S0378-3839(97)00031-8

Sutili, F. J., Denardi, L., Durlo, M. A., Rauch, H. P., & Weissteiner, C. (2010). Flexural behaviour of selected plants under static load. *Hydrology and Earth System Sciences Discussions*, *7*(1), 1459–1483. https://doi.org/10.5194/hessd-7-1459-2010

Sutton-Grier, A. E., Wowk, K., & Bamford, H. (2015). Future of our coasts: The potential for natural and hybrid infrastructure to enhance the resilience of our coastal communities, economies and ecosystems. *Environmental Science and Policy*, *51*, 137–148. https://doi.org/10.1016/j.envsci.2015.04.006

Suzuki, T. (2011). *Wave Dissipation Over Vegetation Fields* [Doctoral dissertation, Delft University of Technology].

Suzuki, T., Zijlema, M., Burger, B., Meijer, M. C., & Narayan, S. (2012). Wave dissipation by vegetation with layer schematization in SWAN. *Coastal Engineering*, *59*(1), 64–71. https://doi.org/10.1016/j.coastaleng.2011.07.006

Syvitski, J. P., Kettner, A. J., Overeem, I., Hutton, E. W., Hannon, M. T., Brakenridge, G. R., Day, J., Vörösmarty, C., Saito, Y., Giosan, L., & Nicholls, R. J. (2009). Sinking deltas due to human activities. *Nature Geoscience*, *2*(10), 681–686. https://doi.org/10.1038/ngeo629

TAW. (2008). *Addendum I bij de Leidraad Rivieren* (tech. rep.). MVW.

Taylor, T. (2009). *Flowering plants. Biology and Evolution of Fossil Plants.* (Vol. 940). https://doi.org/10.1016/b978-0-12-373972-8.00022-x

Temmerman, S., Meire, P., Bouma, T. J., Herman, P. M., Ysebaert, T., & De Vriend, H. J. (2013). Ecosystem-based coastal defence in the face of global change. *Nature*, *504*(7478), 79–83. https://doi.org/10.1038/nature12859

ter Meulen, D. W. B., Cabboi, A., & Antonini, A. (2024). Hybrid operational modal analysis of an operative two-bladed offshore wind turbine. *Mechanical Systems and Signal Processing*, *223*(September 2023). https://doi.org/10.1016/j.ymssp.2024.111822

Tinoco, R. O., & Coco, G. (2018). Turbulence as the Main Driver of Resuspension in Oscillatory Flow Through Vegetation. *Journal of Geophysical Research: Earth Surface*, *123*(5), 891–904. https://doi.org/10.1002/2017JF004504

Tomiczek, T., Wargula, A., Lomónaco, P., Goodwin, S., Cox, D., Kennedy, A., & Lynett, P. (2020). Physical model investigation of mid-scale mangrove effects on flow hydrodynamics and pressures and loads in the built environment. *Coastal Engineering*, *162*(September). https://doi.org/10.1016/j.coastaleng.2020.103791

van Casteren, A., Sellers, W. I., Thorpe, S. K., Coward, S., Crompton, R. H., & Ennos, A. R. (2012). Why don't branches snap? The mechanics of bending failure in three temperate angiosperm trees. *Trees - Structure and Function*, *26*(3), 789–797. https://doi.org/10.1007/s00468-011-0650-y

van Loon-Steensma, J. M., & Schelfhout, H. A. (2017). Wide Green Dikes: A sustainable adaptation option with benefits for both nature and landscape values? *Land Use Policy*, *63*, 528–538. https://doi.org/10.1016/j.landusepol.2017.02.002

van Starrenburg, C., van Ijzerloo, L., van der Wal, D., & Bouma, T. J. (2024). Are willows suitable for flood defense? Quantifying mechanical properties of willow species [Manuscript submitted for publication]. *Estuarine, Coastal and Shelf Sciences*.

van Veelen, T. J., Fairchild, T. P., Reeve, D. E., & Karunarathna, H. (2020). Experimental study on vegetation flexibility as control parameter for wave damping and velocity structure. *Coastal Engineering*, *157*(December 2019), 103648. https://doi.org/10.1016/j.coastaleng.2020.103648

van Veelen, T. J., Karunarathna, H., & Reeve, D. E. (2021). Modelling wave attenuation by quasi-flexible coastal vegetation. *Coastal Engineering*, *164*(November 2020), 103820. https://doi.org/10.1016/j.coastaleng.2020.103820

van Wesenbeeck, B. K., de Boer, W., Narayan, S., van der Star, W. R., & de Vries, M. B. (2017). Coastal and riverine ecosystems as adaptive flood defenses under a changing climate. *Mitigation and Adaptation Strategies for Global Change*, *22*(7), 1087–1094. https://doi.org/10.1007/s11027-016-9714-z

van Wesenbeeck, B. K., Griffin, J. N., van Koningsveld, M., Gedan, K. B., McCoy, M. W., & Silliman, B. R. (2013). Nature-Based Coastal Defenses: Can Biodiversity Help? (S. Levin, Ed.). *Encyclopedia of Biodiversity*, *5*, 451–458. https://doi.org/10.1016/B978-0-12-384719-5.00323-3

van Wesenbeeck, B. K., Mulder, J. P., Marchand, M., Reed, D. J., De Vries, M. B., De Vriend, H. J., & Herman, P. M. (2014). Damming deltas: A practice of the past? Towards nature-based flood defenses. *Estuarine, Coastal and Shelf Science*, *140*, 1–6. https://doi.org/10.1016/j.ecss.2013.12.031

van Wesenbeeck, B. K., Wolters, G., Antolínez, J. A. A., Kalloe, S. A., Hofland, B., de Boer, W. P., Çete, C., & Bouma, T. J. (2022). Wave attenuation through forests under extreme conditions. *Scientific Reports*, *12*(1), 1–8. https://doi.org/10.1038/s41598-022-05753-3

van Zelst, V. T., Dijkstra, J. T., van Wesenbeeck, B. K., Eilander, D., Morris, E. P., Winsemius, H. C., Ward, P. J., & de Vries, M. B. (2021). Cutting the costs of coastal protection by integrating vegetation in flood defences. *Nature Communications*, *12*(1), 1–11. https://doi.org/10.1038/s41467-021-26887-4

van der Meer, J., Allsop, N., Bruce, T., De Rouck, J., Kortenhaus, A., Pullen, T., Schuttrumpf, H., Troch, P., & Zanuttigh, B. (2018). *EurOtop Manual: Manual of overtopping of sea defences and related structures*. www.overtopping-manual.com

Vergouwe, R. (2010). *De veiligheid van Nederland in kaart* (tech. rep. No. November). Rijkswaterstaat Projectbureau VNK.

Vogel, S. (1989). Drag and reconfiguration of broad leaves in high winds. *Journal of Experimental Botany*, *40*(8), 941–948. https://doi.org/10.1093/jxb/40.8.941

Vo-Luong, P., & Massel, S. (2008). Energy dissipation in non-uniform mangrove forests of arbitrary depth. *Journal of Marine Systems*, *74*(1-2), 603–622. https://doi.org/10.1016/j.jmarsys.2008.05.004

Vuik, V., Jonkman, S. N., Borsje, B. W., & Suzuki, T. (2016). Nature-based flood protection: The efficiency of vegetated foreshores for reducing wave loads on coastal dikes. *Coastal Engineering*, *116*, 42–56. https://doi.org/10.1016/j.coastaleng.2016.06.001

Vuik, V. (2019). *Building Safety with Nature Salt marshes for flood risk reduction* [Doctoral dissertation]. Delft University of Technology. https://doi.org/10.4233/uuid:9339474c-3c48-437f-8aa5-4b908368c17e

Waterkeringen., t. a. v. d. (1985). *leidraad voor het ontwerpen van Leidraad voor het ontwerpen van rivierdijken* (tech. rep.).

Whittaker, P., Wilson, C., Aberle, J., Rauch, H. P., & Xavier, P. (2013). A drag force model to incorporate the reconfiguration of full-scale riparian trees under hydrodynamic loading. *Journal of Hydraulic Research*, *51*(5), 569–580. https://doi.org/10.1080/00221686.2013.822936

Wieselsberger, C. (1921). New data of the laws of fluid resistance. *Physikalische Zeitschrift*, *22*, 321–328.

Winsemius, H. C., Van Beek, L. P., Jongman, B., Ward, P. J., & Bouwman, A. (2013). A framework for global river flood risk assessments. *Hydrology and Earth System Sciences*, *17*(5), 1871–1892. https://doi.org/10.5194/hess-17-1871-2013

Wolters, M., Bakker, J. P., Bertness, M. D., Jefferies, R. L., & Möller, I. (2005). Saltmarsh erosion and restoration in south-east England: Squeezing the evidence requires realignment. *Journal of Applied Ecology*, *42*(5), 844–851. https://doi.org/10.1111/j.1365-2664.2005.01080.x

Wong, P. P., Losada, I. J., Gattuso, J.-P., Hinkel, J., Khattabi, A., McInnes, K., Saito, Y., & Sallenger, A. (2013). Coastal Systems and Low-Lying Areas. *Climate Change 2014: Impacts, Adaptation, and Vulnerability. Part A: Global and Sectoral Aspects. Contribution of Working Group II to the Fifth Assessment Report of the Intergovernmental Panel on Climate Change [Field, C.B., V.R. Barros, D.J. Dokken, K.J.*, (October 2013), 1–85.

Wu, W. C., & Cox, D. T. (2015). Effects of wave steepness and relative water depth on wave attenuation by emergent vegetation. *Estuarine, Coastal and Shelf Science*, *164*(August 2015), 443–450. https://doi.org/10.1016/j.ecss.2015.08.009

Wunder, S., Lehmann, B., & Nestmann, F. (2011). Determination of the drag coefficients of emergent and just submerged willows. *International Journal of River Basin Management*, *9*(3-4), 231–236. https://doi.org/10.1080/15715124.2011.637499

Wuytack, T., Verheyen, K., Wuyts, K., Kardel, F., Adriaenssens, S., & Samson, R. (2010). The potential of biomonitoring of air quality using leaf characteristics of white willow (Salix alba L.) *Environmental Monitoring and Assessment*, *171*(1-4), 197–204. https://doi.org/10.1007/s10661-009-1271-4

Yang, S. L., Shi, B. W., Bouma, T. J., Ysebaert, T., & Luo, X. X. (2012). Wave Attenuation at a Salt Marsh Margin: A Case Study of an Exposed Coast on the Yangtze Estuary. *Estuaries and Coasts*, *35*(1), 169–182. https://doi.org/10.1007/s12237-011-9424-4

Ysebaert, T., Yang, S. L., Zhang, L., He, Q., Bouma, T. J., & Herman, P. M. (2011). Wave attenuation by two contrasting ecosystem engineering salt marsh macrophytes in the intertidal pioneer zone. *Wetlands*, *31*(6), 1043–1054. https://doi.org/10.1007/s13157-011-0240-1

Zeller, R. B., Weitzman, J. S., Abbett, M. E., Zarama, F. J., Fringer, O. B., & Koseff, J. R. (2014). Improved parameterization of seagrass blade dynamics and wave attenuation based on numerical and laboratory experiments. *Limnology and Oceanography*, *59*(1), 251–266. https://doi.org/10.4319/lo.2014.59.1.0251

Zhu, Z., Vuik, V., Visser, P. J., Soens, T., van Wesenbeeck, B., van de Koppel, J., Jonkman, S. N., Temmerman, S., & Bouma, T. J. (2020). Historic storms and the hidden value of coastal wetlands for nature-based flood defence. *Nature Sustainability*, *3*(10), 853–862. https://doi.org/10.1038/s41893-020-0556-z

A

WAVE DAMPING UNDER STORM CONDITIONS

Worldwide, communities are facing increasing flood risk, due to more frequent and intense hazards and rising exposure through more people living along coastlines and in flood plains. Nature-based Solutions (NbS), such as mangroves, and riparian forests, offer huge potential for adaptation and risk reduction. The capacity of trees and forests to attenuate waves and mitigate storm damages receives massive attention, especially after extreme storm events. However, application of forests in flood mitigation strategies remains limited to date, due to lack of real-scale measurements on the performance under extreme conditions. Experiments executed in a large-scale flume with a willow forest to dissipate waves show that trees are hardly damaged and strongly reduce wave and run-up heights, even when maximum wave heights are up to 2.5 m. *It was observed for the first time that the surface area of the tree canopy is most relevant for wave attenuation and that the very flexible leaves limitedly add to effectiveness. Overall, the study shows that forests can play a significant role in reducing wave heights and run-up under extreme conditions. Currently, this potential is hardly used but may offer future benefits in achieving more adaptive levee designs.*

This chapter has been published in *Scientific Reports* as:

van Wesenbeeck, B. K., Wolters, G., Antolínez, J. A. A., Kalloe, S. A., Hofland, B., de Boer, W. P., Çete, C., & Bouma, T. J. (2022). Wave attenuation through forests under extreme conditions. *Scientific Reports*, *12*(1), 1–8. https://doi.org/10.1038/s41598-022-05753-3

A

A.1. Introduction

Vegetated foreshores, such as marshes and mangroves, are promoted globally for their capacities in reducing impacts of waves, winds and surges (*Costanza et al., 1997*; *Temmerman et al., 2013*; *Koch et al., 2009*; *Gedan et al., 2011*; *Zhu et al., 2020*; *Shepard et al., 2011*). Besides along coastlines there is also potential for reducing wave heights and run-up in rivers and lakes by floodplain vegetation and riparian forests (*Coops et al., 1991*; *van Wesenbeeck et al., 2017*). Although the capacity of trees to reduce hydrodynamic energy is intuitive and measured under benign conditions in the field on mangroves (*Quartel et al., 2007*; *Bao, 2011*; *Horstman et al., 2014*), their effectiveness under more extreme events is not well substantiated with quantitative evidence. Numerical models generally simplify vegetation by representing it as rigid cylinders (*Dalrymple et al., 1984*; *Suzuki et al., 2012*). Laboratory-flume studies with scaled forests result in parameterised bulk drag values, but these are not yet validated for real-scale extreme situations. Hence, varying flexibility and surface area of leaves, branches and stems, result in scale effects and as a consequence calibrated drag coefficients remain inaccurate (*Maza et al., 2019*; *Nepf, 1999*).

Previous field and laboratory-flume measurements on wave attenuation over grassy vegetated foreshores and plants show that energy dissipation depends on incident wave energy, ambient water depth, and the (vertical) structure and flexibility of vegetation (*Wolters et al., 2005*; *Vuik et al., 2016*; *Yang et al., 2012*; *Bouma et al., 2005*; *Bouma et al., 2010*). Field studies included significant wave heights up to around 0.6 m (*Yang et al., 2012*; *Ysebaert et al., 2011*) with extremes up to 1.0 m. *Möller et al. (2014)* carried out flume experiments exposing real flexible grassy vegetation to maximum wave heights of 0.9 m. In contrast, for forests no such large-scale quantitative evidence exists for storm conditions. Current field observations represent relatively mild conditions with significant wave heights in the range of 0.1-0.5 m (*Mazda et al., 2006*; *Granek and Ruttenberg, 2008*; *Horstman, 2014*). To obtain a quantitative understanding of wave-attenuation capacity of forests under more extreme conditions, we ran real-scale flume tests with various water levels and significant wave heights up to 1.5 m, using both intact and defoliated 15 years old willows (*Salix alba*) trees.

A.2. Results

A.2.1. Experimental setup

We constructed a real-scale willow forest in a wave flume of 300 m long, 5.0 m wide and 9.5 m deep. The forest existed of 32 willow trees that were placed in 16 rows of 2

to build a 40-m-long forest on an 85-m-long platform (Fig. A.1). The pollard willows (*Salix alba*) existed of stems that were 15 years old and branches that were 3 years old since the last cutting. Willows were placed with their roots (in a clod) in the sandy base of the platform and fixated by applying a concrete layer of 20cm as bed. At the back of the forest a concrete levee slope was present (Fig. A.1). Wave attenuation by

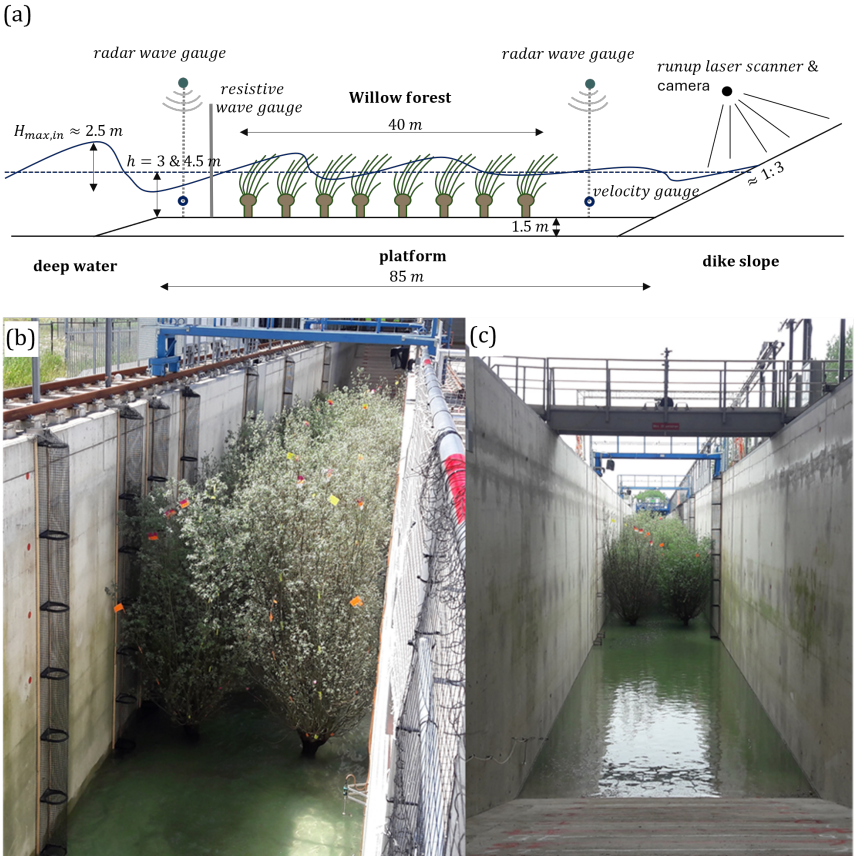

Figure A.1.: (a) Setup of experiments inside the Delta Flume with the most important instruments, (b) Front top view of willow forest, (c) view from the back slope.

the willow forest and associated run-up on the slope were measured for different water depths in the forest ($h = 3.0$ and 4.5m), significant incoming wave heights at the start of the forest. ($H_{m0,i} = 0.2$ m $- 1.5$ m) and different steepness ($S_{op} = 0.02 - 0.06$, where $S_{op} = H_{m0}/\left(gT_p^2/2\pi\right)$ is the fictitious deep water wave steepness). For willows with leaves only tests with 3.0 m water levels were performed as it was feared

that with higher water levels and higher wave heights immediate destruction of the trees would jeopardize further measurements. The tests were designed to limit wave breaking by using water depth ratios of h/H_{m0} larger or equal to 3. The flume is equipped with a reflection compensation system (ARC). All tests were performed with a JONSWAP wave spectrum and a duration of 500 waves per test to allow for a proper statistical analysis of the wave characteristics *(Kirkegaard et al., 2011)*. Due to the lack of data on specific wave spectra at Dutch willow site locations, a JONSWAP spectrum was chosen because it was considered to best represent the young/growing wave conditions. Test series on willows with leaves, without leaves, with a thinned branch density and, as control, without any willows (bare platform) were executed over a period of three weeks (Table A.1, for all tests see Supplementary Information S1). Tests generally lasted for 2-3 days after which the water was lowered. Trees stayed alive and started making new leaves during the tests. Wave characteristics were measured in front of the platform, in front of the forest and behind the forest using resistance wave gauges and radar wave gauges. Wave run-up on the slope was measured using cameras, a laser scanner and visual recordings.

Table A.1.: Summary of the tested hydrodynamic conditions for the different tree forest configurations (series). Test series 1 is omitted due to low water depths. All values are based on the wave height in front of the forest with significant incoming wave height ($H_{m0,i}$), maximum wave height (H_{max}), wave period (T_p), water depth (h) and wave steepness (S_{op}). For all tests of these series that are analyzed in this paper see Table S2.

Vegetation treatment	Series	$H_{m0,i}$ (m)	H_{max} (m)	T_p (s)	h (m)	S_{op} (−)
willow with leaves and full canopy	2	0.43 - 0.97	0.74 - 1.75	2.84 - 5.57	3.00	0.02 - 0.05
willow without leaves and full canopy	3	0.43 - 1.41	0.72 - 2.45	2.84 - 6.85	3.00 - 4.50	0.02 - 0.06
willow without leaves with reduced canopy	4	0.43 - 1.44	0.78 - 2.52	2.84 - 6.85	3.00 - 4.50	0.02 - 0.06
no willows	5	0.17 - 1.43	0.26 - 2.51	2.84 - 6.85	0.60 - 4.50	0.03 - 0.05

A.2.2. Reduction in wave height and run-up through the forest

The wave attenuation effect of the forest was represented as the measured transmitted wave height behind the willow forest (i.e., with leaves, without leaves, reduced branch density), in reference to the case with bare platform (without willows) (Eq. 2.1 in "Methods"). Plotting the wave attenuation as function of the significant incoming wave height, $H_{m0,i}$, shows that for constant 3 m water depth and equal tree configuration the wave damping seems to increase somewhat as a function of wave height (Fig. A.2A). The maximum wave attenuation by the willow forest is approximately 22% over 40 m . Maximum attenuation is found for the willow forest with leaves

and full canopy (Series 2), as could be expected based on the amount of frontal surface areas around the water line. Wave damping with leaves is $1.5-4\%$ (percentage point) higher than for a canopy without leaves (i.e., approximately 20% over 40 m). Wave attenuation with full canopy density but without leaves is $3-7\%$ (percentage point) larger than with a reduced canopy density (i.e., approximately 15% over 40 m). Wave attenuation was found to be strongly dependent on water level. Attenuation for a water depth of 3 m is larger than for 4.5 m . With larger water depths, waves moved through the thinner part of the canopy which also proved more flexible and showed significantly more bending (pers. obs.). Similar effects have been reported with increasing wave heights for salt marshes *(Möller et al., 2014)*. As effects of the bottom are already accounted for in our calculation method for wave attenuation, this likely is explained by the fact that the strongest wave damping occurs when the water depth is around the middle of the canopy height (above the trunk), where the tree has most frontal surface area. The loss of biomass during different test series was rela-

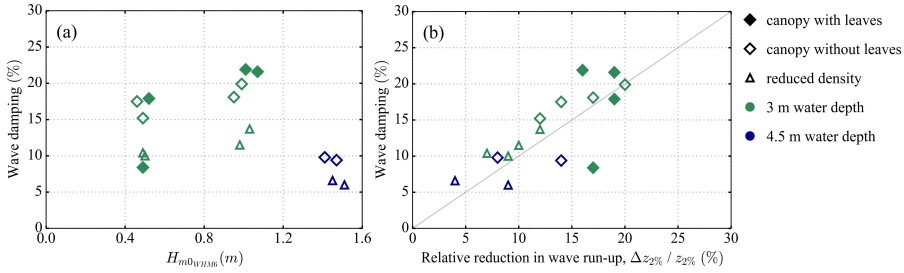

Figure A.2.: (a) Relation between measured wave attenuation (%) and incoming significant wave height ($H_{m0,i}$). Markers represent the different willow forest configurations (2 = with leaves, 3 = without leaves, 4 = reduced density branches), and the colors show water levels (green= 3 m and blue= 4.5 m), (b) Relation between relative reduction in wave run-up on the slope and the wave attenuation through the forest.

tively small (less than 1% of total branches and leaves biomass). Limited breaking of stems or branches was recorded throughout repeated extreme tests, including average wave heights of 1.5 m and maximum wave heights of 2.5 m. Likely, the extreme flexibility of the willow branches limits the amount of actual breaking but also causes reduction in wave damping with larger wave heights.

The wave attenuation by the willows was also assessed using the measured (reduction in) wave run-up on the slope (Fig. A.2B). Plotting the relative reduction in wave run-up height against the relative wave attenuation reveals these two quantities have a similar magnitude of the reduction effect (i.e., up to 20%). However, runup

is influenced by both wave height and wave steepness which is represented by the Irribarren number. The exact influence is not clearly defined for Irribarren numbers around 2, such as in these experiments, but with lower wave heights, the Irribarren number increases, which in its turn increases runup again. Hence, it can be expected that the damping of runup is somewhat less than for wave height.

Also, the observed trends are similar, such as an increase in run-up reduction for increasing wave heights and lower run-up reduction for reduced canopy density. Note that in most cases the wave attenuation based on the wave run-up is somewhat lower than the wave attenuation based on the incident wave height. This might be caused by the method used for the separation of incident and reflected waves (MEM) which is based on linear wave theory, see "Methods" section. The test result for a relative reduction in wave run-up of 17% and wave damping of 8% (test T05, filled green square) seems to be an outlier not in line with the rest of the experiments, since the most similar test in Series 3 also produced a wave damping rate of 17% (just as the wave run-up measurement for T05).

A.2.3. Implications of measurements for wave-vegetation modelling

We utilized the new measurements, to calibrate the spectral wave model SWAN (Simulating Waves Nearshore) *(Booij et al., 1999)*. This model was used in similar studies on wave attenuation over vegetated foreshores (*van Wesenbeeck et al., 2017*; *Suzuki et al., 2012*; *Vuik et al., 2016*) and is frequently used in engineering practice. Suzuki et al. implemented the effects of vegetation in SWAN based on the phase-averaged wave energy dissipation model due to rigid stems for irregular waves (*Dalrymple et al., 1984*; *Mendez and Losada, 2004*). The vegetation model is based on bulk wave dissipation (integrated over all wave frequencies), which is dependent on the incoming wave energy, the water depth and the vertical structure of the vegetation (Eq. 2.2 in "Methods"). A limitation of this vegetation model is that trees are mostly assumed to behave as a rigid material under hydraulic forces *(Mazda et al., 2006)*. Furthermore, uneven biomass distribution over the vertical and differences between stems, branches and leaves are limitedly included through varying exposed frontal area.
Generally, vegetation is described by a single branch diameter $(b_v; m)$ and density $\left(N_v; m^{-2}\right)$ per vertical elevation level (*Suzuki et al., 2012*; *Mendez and Losada, 2004*). However, plants have different branches of different sizes and densities. Therefore, here vegetation was represented by a single parameter $f_i(z)\left(m^2/m^3\right)$, which described the total frontal area per unit volume, instead of $b_v\ N_v\left(m/m^2\right)$. This

parameter is determined for the present trees by counting all branches at breast level, measuring their diameter and then applying the branching model of Jarvela *(Järvelä, 2004)* (Fig. A.3a). Only branches larger than 3 mm were considered. A single representative tree was fully measured to derive a frontal area and determine the frontal surface area distribution over the vertical. This distribution was assumed to hold for all the trees in the flume. For vegetation-wave models, especially the value of the bulk drag coefficient $\left(\tilde{C}_D\right)$ has been subject to debate. For flexible vegetation the value of this factor is reduced compared to the value for rigid cylinders because flexible vegetation moves with the flow, which results in less drag force experienced by the vegetation *(Sumer and Fredsoe, 1998)*. The $\tilde{C}_D$ parameter relies on complex physics (e.g., skin friction, pressure differences, swaying of vegetation), which in turn depend on the vegetation properties in relation to the hydraulic conditions *(Vuik et al., 2016)*. Therefore, instead of determining the $\tilde{C}_D$ values a-priori, several studies have attempted to calibrate the $\tilde{C}_D$ values to measurements and relate them to the Reynolds number (*Mendez et al., 1998*; *Jadhav and Chen, 2012*; *Anderson et al., 2011*; *Möller et al., 2014*) or the Keulegan-Carpenter number KC (*Mendez and Losada, 2004*; *Jadhav et al., 2013*; *Ozeren et al., 2014*; *He et al., 2019*).

Here, the $\tilde{C}_D$ versus the KC number, $\widehat{u}_s T_m/d$ was obtained through optimisation of C_D for the present tests by comparing model results and measurement data of the experiments (Fig. A.3b and S5). The KC number that is used here is based on the spatial weighted average of branch diameter and velocity, and the orbital motion based on H_s and wave period T_p. Values for low KC numbers are close to the relation by Keulegan and Carpenter *(Keulegan and Carpenter, 1958)* for a single rigid cylinder, as at these KC numbers branches do not bend much. For larger KC numbers the drag coefficient is decreasing, which might be due to increasing motion of the branches that reduces the relative flow velocity. With our measurements we extended C_D values for larger KC numbers, showing that C_D values for larger KC numbers are rather constant. Also, C_D values for large KC number from our experiments are considerably lower than values from previous small-scale experiment *(Winsemius et al., 2013)*. He et al. based C_D on measured wave height decay with models of mangrove trees of up to 35 cm height that included roots, trunk and canopy. These larger values for C_D might be due to wall friction that is incorporated in the C_D values derived from small-scale experiments, the influence of viscous stresses becoming relatively more important at small scale, or to swaying of tree branches, which was observed in our experiments. Jadhav et al. based their large values of C_D on wave pressure decay in field measurements on salt marsh vegetation. *Mendez and Losada (2004)* show

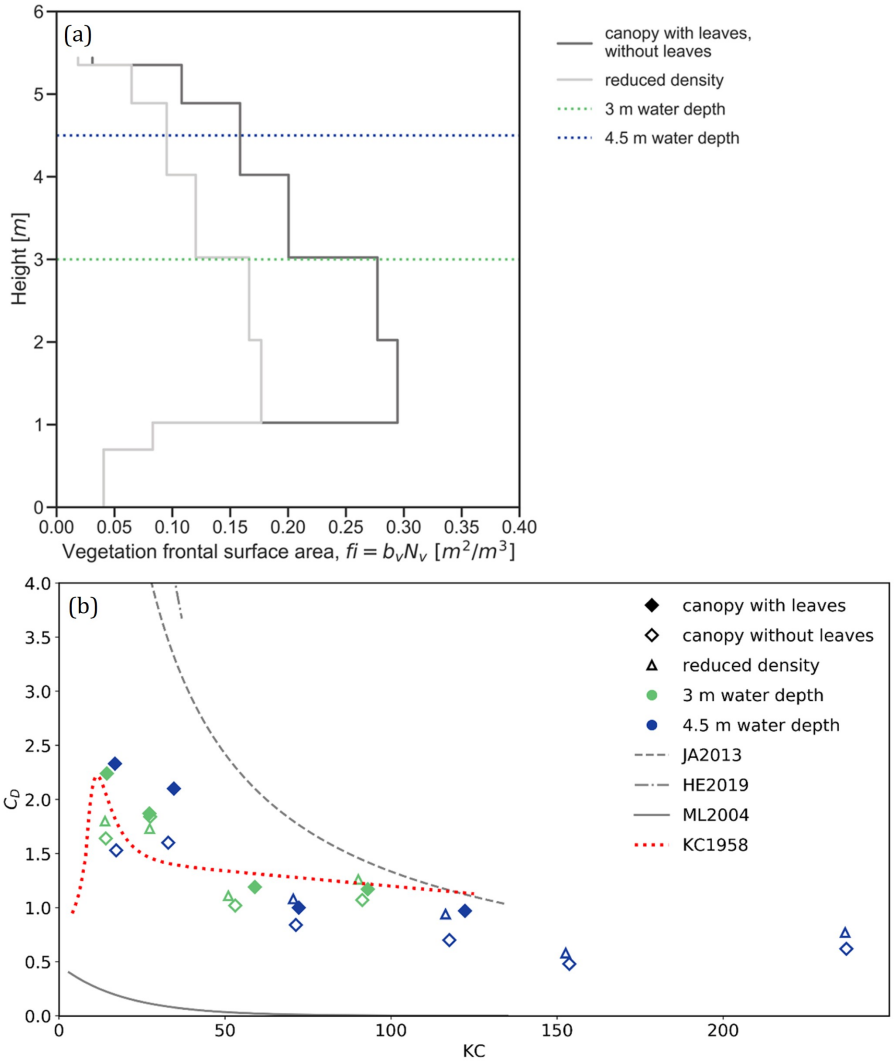

Figure A.3.: (a) Frontal surface area of willow schematization (based in biomass schematization) for test series with full biomass with and without leaves (2 and 3) and with half of the branches removed (4), (b) The *KC*-C_D relation for all test series (2 + 3 + 4) and the comparison with the relations by *He et al. (2019)* (HE2019), *Jadhav et al. (2013)* (JA2013), *Mendez and Losada (2004)* (ML2004), *Keulegan and Carpenter (1958)* (KC1958). For higher KC numbers steady flow would be a straight-line equaling C_D= 1.2.

low C_D for low KC numbers as these were small scale experiments with very flexible vegetation. For rigid mangrove mimics, *Maza et al. (2019)* did measure similar values of $\tilde{C}_D$ between 0.5 and 1.5 at scale 1:6. However, such relations did not exist yet for woody vegetation with a complex vertical structure under extreme conditions on realistic scales (i.e., a wide range of Re and KC numbers).

A.3. Discussion

The present real-scale tests added crucial measurements on the wave attenuation and run-up reduction by forests under extreme conditions and clearly illustrate that floodplain and mangrove forests can contribute significantly to flood safety. This constitutes yet another step towards large-scale implementation of vegetation and levee combinations, or so-called hybrid solutions *(Sutton-Grier et al., 2015)*. These solutions have already been promoted as the way forward under climate change and rising sea levels, as they are considered more adaptive and resilient to uncertainty in environmental boundary conditions (*Cheong et al., 2013*; *van Wesenbeeck et al., 2017*). However, integrated designs for levees or seawalls in concert with mangroves, marshes and floodplain forests are not yet captured in engineering handbooks and guidelines. Current experiments revealed that areas with only small widths of woody vegetation reduce wave impact and run-up considerably (up to 20%).

Results also showed that the amount of reduction is largely dependent on incoming wave heights and lengths, on present surface area of the vegetation and on movement of branches. Especially, representation of complex vegetation by surface area remains a large unknown in these numerical models and is mostly oversimplified by using cylinder shapes for vegetation representation. Looking in Figure A.2A, there are clear effects of reduced density on wave attenuation. If the plant frontal area is determined correctly, then for high KC and Re numbers, the fitted C_D should become a constant value, approaching 1.2, which is representative for cylinders in uniform flow *(Wieselsberger, 1921)*. This is also illustrated by measurements for rigid mangrove mimics by *Maza et al. (2017a)*. For our experiments, C_D values with high KC numbers are somewhat lower, which is likely due to flexibility of branches under high wave conditions. Even though KC and Reynolds are defined differently in different studies, which makes comparison between studies difficult, based on this work and previous work we can conclude that there is a region for high KC/RE numbers where C_D approaches uniform flow. These relationships between KC numbers and C_D allow to better calibrate C_D values for situations with high KC numbers, thereby increasing accuracy of future model predictions and avoiding overestimations of the

damping effects of trees during storms. More studies with real vegetation and reliable and representative surface areas for field conditions are needed to improve vegetation representation in numerical modelling practices.

Caution should be taken to promote trees as a generic solution for mitigation of extreme hazards, as localised studies are always required. With respect to the measurements, the present study deals with emergent vegetation only and the usually observed regime shift with vegetation submergence does not take place and effects of changes in wave profiles or currents are limited *(Jacobsen et al., 2019)*. We also focus on wind waves, as infra-gravity waves are typically not present in situations with riparian vegetation where willow grows. For mangroves growing along more open coasts, infra-gravity waves may play a role. Effects of more diverse forests, such as mangrove

forests with different age stands and biomass distribution, have not been explored yet. However, considering the importance of biomass distribution, which was demonstrated by these experiments, more diverse forests may lead to unforeseen results. Although tests with more tree species are obviously desirable, current experiment generated unique first quantitative insights in the wave attenuation capacity of mature trees that can directly be used for modelling and optimizing foreshore management. For application in the field, wave damping is just one of many design aspects that needs to be considered in the safety assessment of a willow forest. Other aspects such as maintenance, uprooting of trees, and damage due to illness or fire are worth exploring. Nevertheless, the first examples of levee foreshore combinations are emerging in the field *(Borsje et al., 2011)* and likely more are yet to come.

A.4. Methods

A.4.1. Wave measurements

The incoming wave height was based on the wave gauge on the platform in front of the forest. This wave gauge was validated for all test series using the radar measurements (RADAC1) in front of the forest. Wave attenuation by the vegetation during each test is defined as the wave height reduction relative to the incoming wave height, which is obtained from the difference between the wave energy spectra measured with and without vegetation:

$$\text{Wave attenuation} = \frac{H_{m0,\,\text{nowillows}} - H_{m0,\,\text{willows}}}{H_{m0,\,\text{nowillows}}} \tag{2.1}$$

With: H_{m0} the significant wave height behind the forest.

This method to assess wave attenuation proved most reliable, since it allowed us to exclude effects of wave reflection and damping effects of the platform (which resulted in additional wave attenuation of 2-18%). By using a combination of wave gauge with velocity gauge (EMS) the incident wave height at the foot of the dike (with the exclusion of the reflection component from the dike) could be reliably determined using the Maximum Entropy Method MEM *(Massel and Brinkman, 1998)*. Note that the distance between the end of the willow forest and the foot of the dike slope was chosen as large as physically possible in the flume (20 m) to limit the effect of evanescent wave modes. Since evanescent wave modes are typically limited to a distance of 0.4 L_p from the structure *(Klopman and Meer, 1999)*, this was fulfilled by all tests. Also, wave run-up on the slope was measured using cameras, a laser scanner and visual recordings. Wave run-up was obtained through $(z_{2\%,no\,willows}\text{-}z_{2\%,willows})$ / $z_{2\%,no\,willows}$.

A.4.2. Vegetation measurements

Experimental research and field studies on plants (either cultivated or wild), including the collection of plant material, was complied with relevant institutional, national, and international guidelines and legislation. Willows were harvested from private lands where they had been growing for 15 years. They contained stems that were 15 years old and branches that were 3 years old since the last cutting. The branches of the willow trees were categorized into 3 classes based on their diameter at breast height (DBH), namely class 1($DBH > 50$ mm), class 2($20 < DBH \leq 50$ mm) and class 3($DBH < 20$ mm) (see Fig. S4 in Supplementary Information). Relevant tree data was gathered manually, among which: the total number of branches per class for each tree at breast height, the DBH and branch length for 340 branches, and detailed sketches of 9 primary branches.

A.4.3. Frontal surface area distribution

The frontal surface area distribution over the vertical was determined for vegetation configurations with and without leaves. The total frontal surface area of the leaves was estimated by the product of the measured total dry weight (38 kg) and a specific leaf area of 145 cm^2/g *(Wuytack et al., 2010)*, resulting in a value of 1 m^2/m^3 for the leaves. However, under wave loads, leaves bend, leading to a more stream-wised position. Assuming that leaves were situated with the smallest frontal area facing the stream, the specific leaf area becomes 1 cm^2/g (considering a leaf thickness of 0.34 mm, leaf width of 20 mm and dry weight of 0.07 g), which corresponds to a pro-

jected surface area of approximately 0.005 m^2/m^3. This shows that the contribution of the leaves to the total frontal surface area is limited.

The tapering form of the branches and the occurrence of side branches in the upper layers ($i > 2$), lead to varying frontal surface areas (equivalent to $N_i \cdot b_{v,i}$) over the vertical. We used a branching method to estimate the total frontal surface area of each tree (f_{total}). This method was developed by *Järvelä (2004)* and originates from the Strahlers ordering scheme. This ordering scheme characterises branch orders (i.e., the conjunction of two branches of order "m" results in an order "$m+1$" branch, starting with the smallest branches, which are assigned to order $m = 1$). It requires only a few initial tree parameters (such as the average diameter of the smallest branches, d_{min}, and the average diameters of the highest order, d_{high}, in this case DBH) to estimate total frontal area of a tree (f_{total}) by using branching factors (R_B, R_D, R_L) between subsequent branch orders. A more detailed description of the steps is given in the work of *Järvelä (2004)*. A factor of 0.5 was applied to the resulting frontal area per order, to account for the frontal surface area of a cone shaped branch instead of cylinders. Both measurements at breast height and detailed sketches of the primary branches were input to determine the initial parameters and branching factors. These detailed sketches were also used to validate the outcome of this branching methods (See Supplementary Information S1 for further details). With this, the total frontal area for each tree was determined. Although this method is used to predict the total frontal area for trees, its distribution over the height is yet unknown. Therefore, an additional step was added to determine how total frontal area is distributed over height ($f(z)$). For this, a single tree was fully measured (i.e., diameters $b_{v,i}$ and the number of branches N_i at every meter along the height of the tree). This distribution was assumed to hold for all the trees in the flume.

A.4.4. Wave dissipation model

The spectral wave model SWAN (Simulating Waves Nearshore) *(Booij et al., 1999)* following *Suzuki (2011)* was used to model the amount of wave dissipation by willow trees. SWAN was run in its 1D stationary mode, in a Cartesian and regular computational grid. The willow forest was modelled by accounting for 7 vertical layers of vegetation (expressed as frontal surface area), which were assumed to be uniform along the forest length. SWAN is based on the bulk wave dissipation (integrated over all wave frequencies), which depends on the incoming wave energy, relative water depth and vegetation characteristics:

$$\langle \varepsilon_v \rangle = \sum_{i=1:7} \frac{1}{4\sqrt{2\pi}} \rho \tilde{C}_D \left(\frac{gk}{2\sigma} \right)^3 f_i \frac{\left(\sinh^3 k\alpha_i h - \sinh^3 k\alpha_{i-1} h\right) + 3\left(\sinh k\alpha_i h - \sinh k\alpha_{i-1} h\right)}{3k \cosh^3 kh} H_s^3 \tag{2.2}$$

where $\langle \varepsilon_v \rangle$ is the averaged wave energy dissipation due to vegetation, $\tilde{C}_D$ the bulk drag coefficient, g the gravitational acceleration constant, k the mean wave number, α the portion of the water depth covered by vegetation for layer i, h the water depth, H_s the significant wave height, and f_i the total frontal width of vegetation per surface area for layer i, which is equivalent to the generally used $b_{v,i}N_{v,i}$.

A correlation was found between the bulk drag coefficient (C_D) and the Keulegan-Carpenter number (KC) *(Keulegan and Carpenter, 1958)*, as shown in Fig. A.3b. The KC number is defined as $KC = \widehat{u}_s T_m / D_v$, where $\widehat{u}_s$ is the characteristic velocity, D_v is a representative diameter for the branches of the entire tree, and T_m is the wave period. The characteristic velocity $(\widehat{u}_s)$ is the maximum velocity per layer integrated over the water depth based on linear wave theory. The representative diameter (D_v) is determined for each water depth as the branch diameter weighted over the number of branches per vegetation layer and over the layer thickness. The KC number was determined by considering separate layers over the height. This was necessary as willow trees have complex geometries which involve diameter decay and varying branch densities. Several other references use the total width per tree/plant, which has no direct physical meaning in the sense of the original definition of the KC number *(Keulegan and Carpenter, 1958)*. Additionally, other studies show differences in flexibility and absence of extra viscous forces that influence results at a small scale.

A.4.5. Statement on plant materials

Experiments in this research were executed with cultivated willow species (*Salix alba*) of 15 years old that were obtained from a Dutch private site. Trees were replaced with new younger trees. *Salix alba* does not occur on the list of threatened species for the Netherlands and is labeled as stable.

B

SUPPORTING INFORMATION CHAPTER 2

B

B.1. Wave conditions

Table B.1.: Overview of the test series with corresponding hydrodynamic conditions and vegetation configurations.

Test series (TS)	Description	Significant wave height, H_{m0} (m)	Peak wave period, T_p (s)	Water depth, h (m)
1 (T001-T004)	Trunk only	0.19 – 0.28	1.80 - 2.80	0.6, 0.7
2 (T005-T012)	Full canopy with leaves	0.43 – 0.97	2.84 - 5.57	3.0, 4.5
3 (T013-T022)	Full canopy without leaves	0.43 – 1.41	2.84 – 6.85	3.0, 4.5
4 (T023-T030)	Reduced canopy without leaves	0.43 – 1.44	2.84 – 6.85	3.0, 4.5
5 (T031-T042)	No willows	0.17 - 1.43	1.78 - 6.85	0.6, 0.7, 3.0, 4.5

B.2. Tree parameters forest

Table B.2.: The initial parameters used as input for the simulations. [Lower limit; average value; Upper limit]. Here the Lower Limit and the Upper Limit values are given according to 95% Confidence Interval. The height of the canopy, H_{canopy}, for all the 32 trees was [3.41; 4.4; 5.5] and the minimum diameter, d_{min} was 3 mm.

	L_{high} (m)	DBH (m)	N_{high} (-)
Class 1	[2.5; 3.2; 4]	[0.05; 0.052; 0.062]	[0; 3; 9]
Class 2	[2.46; 2.5; 2.52]	0.037	[17; 28; 49]
Class 3	0.82	0.01	[27; 57; 108]

B.3. Position primary branches on the trunk

B.4. Analytical Formulation Including for Layers

In *(Mendez and Losada, 2004)* no layer schematization of the vegetation was included, hence the assumption was made that the vegetation can be described with an average diameter and density over the height. However, the vertical distribution of vegetation parameters is important for accurate wave damping predictions, especially for woody vegetation. With this perspective, *(Suzuki, 2011)* incorporated layers in wave damping models. This was included in numerical models such as SWAN and SWASH. In this section we aim to incorporate the layer schematization in the analytical formulation of *(Mendez and Losada, 2004)*.

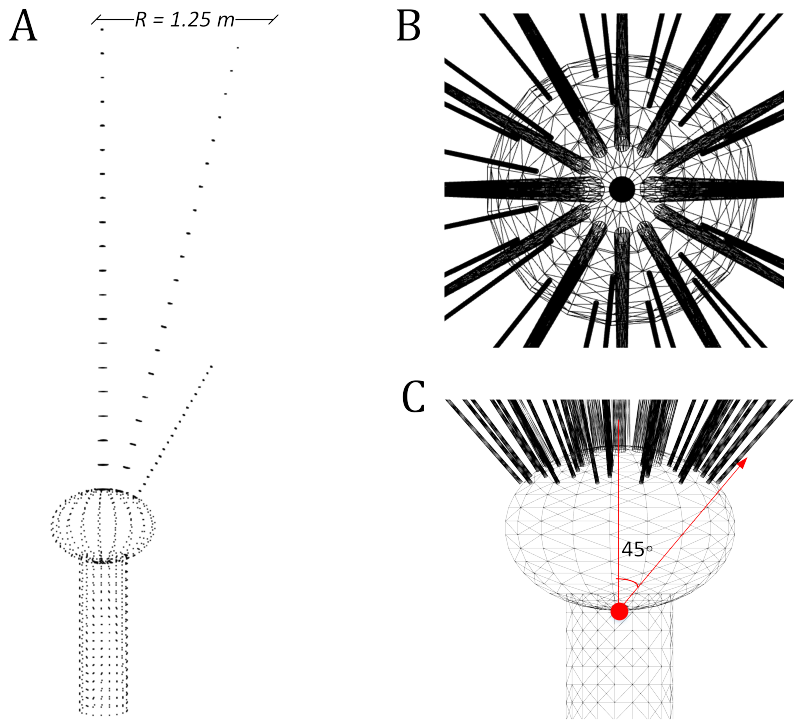

Figure B.1.: **(A)** The primary branches (class 1, 2 and 3) are positioned on the trunk taking the maximum radius of the canopy into consideration, **(B)** Positions of the primary branches on the trunk, with the largest branches (class 1) positioned at the centre of the knot, **(C)** The maximum angle

The energy balance equation:

$$\frac{\partial(Ec_g)}{\partial x} = \varepsilon_v \tag{B.1}$$

where ε_v is the time-averaged energy dissipation rate per unit area by vegetation. In this case the energy dissipation by vegetation will be the sum of dissipation by every single vegetation layer.

$$\varepsilon_v = \sum_{i=1}^{I} \varepsilon_{v,i} \tag{B.2}$$

$$\varepsilon_{v,i} = \int_{-h+\alpha_{i-1}\cdot h}^{-h+\alpha_i \cdot h} Fu\, dz \tag{B.3}$$

$$\int_{-h+\alpha_{i-1}\cdot h}^{-h+\alpha_i\cdot h} F u\, dz = \frac{1}{2\sqrt{\pi}}\rho \tilde{C_D} b_v N \left(\frac{k_p g}{2\sigma_p}\right)^3 \times \frac{(\sinh^3 k_p\alpha_{i-1}h - \sinh^3 k_p\alpha_i h) + 3(\sinh k_p\alpha_{i-1}h - \sinh k_p\alpha_i h)}{3k_p \cosh^3 k_p h} \times H_{rms}^3$$

$$\sum_{i=1}^{I} \varepsilon_{v,i} = \frac{1}{2\sqrt{\pi}}\rho \left(\frac{k_p g}{2\sigma_p}\right)^3 \frac{1}{3k_p \cosh^3 k_p h} \times \left[\sum_{i=1}^{I} \tilde{C_{D,i}} N_i b_{v,i} \left(\sinh^3 k_p\alpha_{i-1}h - \sinh^3 k_p\alpha_i h\right) + 3\left(\sinh k_p\alpha_{i-1}h - \sinh k_p\alpha_i h\right)\right] H_{rms}^3$$

We assume flat bottom, thus the water depth and group wave velocity do not change in space. The energy balance equation then be written as:

$$\frac{\partial (E c_g)}{\partial x} = \frac{1}{8}\rho g c_g \frac{\partial H_{rms}^2}{\partial x} \tag{B.4}$$

$$\frac{1}{8}\rho g c_g \frac{\partial H_{rms}^2}{\partial x} = \frac{1}{2\sqrt{\pi}}\rho \left(\frac{k_p g}{2\sigma_p}\right)^3 \times \frac{1}{3k_p \cosh^3 k_p h}\left[\sum_{i=1}^{I} \tilde{C_{D,i}} N_i b_{v,i} \left(\sinh^3 k_p\alpha_{i-1}h - \sinh^3 k_p\alpha_i h\right) + 3\left(\sinh k_p\alpha_{i-1}h - \sinh k_p\alpha_i h\right)\right] H_{rms}^3$$

$$\frac{\partial H_{rms}^2}{\partial x} = -B_0 H_{rms}^3 \tag{B.5}$$

where $B_0 = \frac{8}{2\sqrt{\pi}}\rho\frac{1}{c_g}g^2\left(\frac{k_p}{2\sigma_p}\right)^3\frac{1}{3k_p\cosh^3 k_p h}\times$

$$\left[\sum_{i=1}^{I} N_i b_{v,i}\tilde{C_{D,i}}\left(\sinh^3 k_p\alpha_{i-1}h-\sinh^3 k_p\alpha_i h\right)+3\left(\sinh k_p\alpha_{i-1}h-\sinh k_p\alpha_i h\right)\right]$$

The general solution of Equation B.5 is:

$$\frac{H_{rms}}{H_{rms,0}}=\frac{1}{1+\frac{B_0 H_{rms,0}}{2}x}=\frac{1}{1+\beta x} \tag{B.6}$$

B

$$\beta=\frac{8}{4\sqrt{\pi}}\frac{1}{c_g}g^2\left(\frac{k_p}{2\sigma_p}\right)^3\frac{1}{3k_p\cosh^3 k_p h}\left[\sum_{i=1}^{I} N_i b_{v,i}\tilde{C_{D,i}}(\sinh^3 k_p\alpha_{i-1}h-\sinh^3 k_p\alpha_i h)+3(\sinh k_p\alpha_{i-1}h-\sinh k_p\alpha_i h)\right]H_{rms,0}$$

We substitute $\frac{\sigma(\sinh 2kh+2kh)}{2k\sinh 2kh}$ for c_g. Hereafter, we simplify $\frac{2g^2k^4\sinh 2kh}{\sigma^4 k\cosh^3 kh}$ to $\frac{4k}{\sinh kh}$ as shown in Equation 1.12.

$$\beta=\frac{1}{3\sqrt{\pi}}\frac{k_p}{\sinh kh(\sinh 2kh+2kh)}\times$$

$$\left[\sum_{i=1}^{I} C_{D,i}N_i b_{v,i}(\sinh^3 k_p\alpha_{i-1}h-\sinh^3 k_p\alpha_i h)+3(\sinh k_p\alpha_{i-1}h-\sinh k_p\alpha_i h)\right]H_{rms,0}$$

In terms of H_{m0}, the formulation can be rewritten by substituting $H_S = 1.416\,H_{rms}$. The above formulation becomes:

$$\frac{H_s}{H_{s,0}}=\frac{1}{1+\frac{B_0(H_{s,0}/1.416)}{2}x}=\frac{1}{1+\beta x} \tag{B.7}$$

$$\beta=\frac{1}{3\sqrt{\pi}}\frac{k_p}{\sinh kh(\sinh 2kh+2kh)}\times$$

$$\left[\sum_{i=1}^{I} C_{D,i}N_i b_{v,i}(\sinh^3 k_p\alpha_{i-1}h-\sinh^3 k_p\alpha_i h)+3(\sinh k_p\alpha_{i-1}h-\sinh k_p\alpha_i h)\right]\left(\frac{H_{s,0}}{1.416}\right)$$

Where $N_i b_{v,i}$ can be written as one parameter, called the frontal surface area of vegetation in layer i, $A_{v,i}$. However, this β from Equation B.7 accounts for wave energy dissipation by vegetation and the flume walls, therefore now referred to as $\beta_{veg\&flume}$. However, we need to remove bottom friction and wall friction effects and find β_{veg}. For this, we use the calibration tests (i.e., tests without vegetation). From the calibration tests we find β_{flume}. This is according to the study of *Maza et al. (2019)*.

$$\frac{1}{1+\beta_{veg}x} = \frac{1}{1+\beta_{veg\&flume}x} - \frac{1}{1+\beta_{flume}x}, \tag{B.8}$$

where

$$\frac{H_s}{H_{s,0}} = \frac{1}{1+\beta_{veg\&flume}x}$$

and

$$\frac{H_{s,calibration}}{H_{s,0,calibration}} = \frac{1}{1+\beta_{flume}x}$$

We assumed a constant drag coefficient for the trunk of 1.1 ($C_{D,trunk}$), while searching for the drag coefficient of the canopy. The equation for finding $C_{D,canopy}$ is then as follows:

$C_{D,canopy} =$

$$\frac{\beta_{veg} - C_{D,trunk}A_{v,trunk}\frac{1}{\sqrt{2\pi}}\frac{kH_{s,0}}{\sinh kh(\sinh 2kh+2kh)}\left((\sinh^3 kh\alpha_{i=0} - \sinh^3 kh\alpha_{i=1}) + 3(\sinh kh\alpha_{i=0} - \sinh kh\alpha_{i=1})\right)}{\frac{1}{\sqrt{2\pi}}\frac{kH_{s,0}}{\sinh kh(\sinh 2kh+2kh)}\sum_{i=2}^{I}\left[A_{v,i}\left((\sinh^3 k_p\alpha_{i-1}h - \sinh^3 k_p\alpha_i h) + 3(\sinh k_p\alpha_{i-1}h - \sinh k_p\alpha_i h)\right)\right]}$$

C

SUPPORTING INFORMATION CHAPTER 3

C.1. Experimental conditions

Table C.1.: Overview of the entire scaled test program with equivalent real-scale tests.

Vegetation	Small-scale test	Real-scale test	h_0(m)	h_f(m)	H_{s0}(m)	T_p(s)
50% density	S101	R101	0.53	0.3	0.05	0.9
	S102	R102	0.53	0.3	0.117	1.13
	S103	R103	0.53	0.3	0.05	1.265
	S104	R104	0.53	0.3	0.101	1.79
	S105	-	0.68	0.45	0.05	0.9
	S106	-	0.68	0.45	0.103	1.265
	S107	-	0.68	0.45	0.05	1.265
	S108	-	0.68	0.45	0.1	1.79
	S109	R109	0.68	0.45	0.161	1.55
	S110	R110	0.68	0.45	0.152	2.19
100% density	S201	R201	0.53	0.3	0.05	0.9
	S202	R202	0.53	0.3	0.117	1.13
	S203	R203	0.53	0.3	0.05	1.265
	S204	R204	0.53	0.3	0.101	1.79
	S205	-	0.68	0.45	0.05	0.9
	S206	-	0.68	0.45	0.103	1.265
	S207	-	0.68	0.45	0.05	1.265
	S208	-	0.68	0.45	0.1	1.79
	S209	R209	0.68	0.45	0.161	1.55
	S210	R210	0.68	0.45	0.152	2.19
	S211	-	0.8	0.57	0.05	0.9
	S212	-	0.8	0.57	0.103	1.265
	S213	-	0.8	0.57	0.05	1.265
	S214	-	0.8	0.57	0.1	1.79
	S215	-	0.8	0.57	0.161	1.55
	S216	-	0.8	0.57	0.152	2.19
No Vegetation	S001	R001	0.53	0.3	0.05	0.9
	S002	R002	0.53	0.3	0.117	1.13
	S003	R003	0.53	0.3	0.05	1.265
	S004	R004	0.53	0.3	0.101	1.79
	S005	-	0.68	0.45	0.05	0.9
	S006	-	0.68	0.45	0.103	1.265
	S007	-	0.68	0.45	0.05	1.265
	S008	-	0.68	0.45	0.1	1.79
	S009	R009	0.68	0.45	0.161	1.55
	S010	R010	0.68	0.45	0.152	2.19
	S011	-	0.8	0.57	0.05	0.9
	S012	-	0.8	0.57	0.103	1.265
	S013	-	0.8	0.57	0.05	1.265
	S014	-	0.8	0.57	0.1	1.79
	S015	-	0.8	0.57	0.161	1.55
	S016	-	0.8	0.57	0.152	2.19

C.2. Branch Motion Real-scale Experiments

The camera set-up of the real-scale tests is shown in Figure C.1. Every 0.5 m along the wall was horizontally marked (with dots and crosses), while the vertical was marked every 1.25 m with the black cross and half-way with a red dot (62.5 cm).
The maximum tip deflection of a class 2 primary branch ($20 \leq D_b \leq 50$ mm) on the tree in the first row of the forest was determined. The total length of the branch was approximated using D_b – branchlength relations from Figure 8 in *Kalloe et al. (2022a)*, where it was shown that the total length can range between 2-4 m. We chose the average total length to be 3 m.

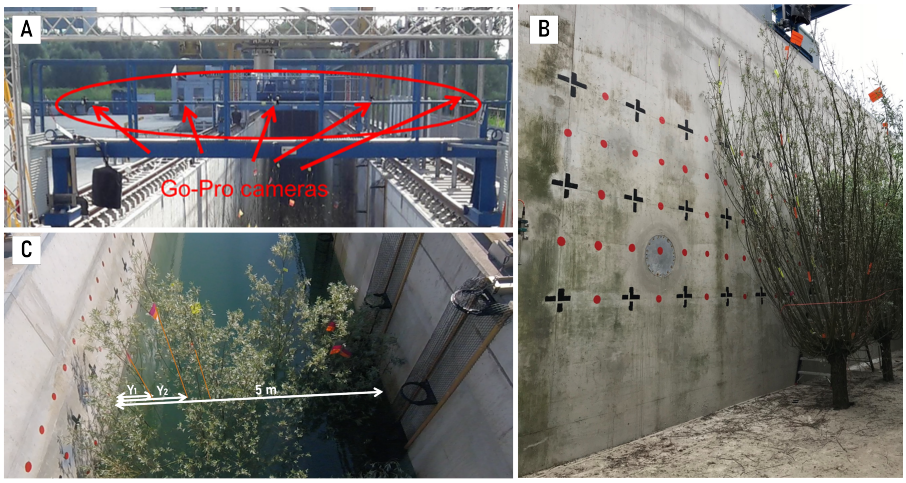

Figure C.1.: Set-up of the cameras for the qualitative analysis of branch motion from the real-scale experiments.

First, the wave signal measured at WG6 (x= 96.5 m) was translated to the position in front of the tree (x= 113.5 m). We validated this by applying this translation to the measurements by RADAC01 and predicted the measurements at WG6. This is shown in Figure C.2 for test R201.

After this, we selected 5 wave heights (Table C.2) to approximate the maximum branch deflection. These wave heights were chosen such that the flag was still visible during the wave attack.

C.2.1. Sensitivity Analysis

The deflection of the live branches was determined by video analysis. This was a qualitative analysis were the maximum deflection related to a certain wave height

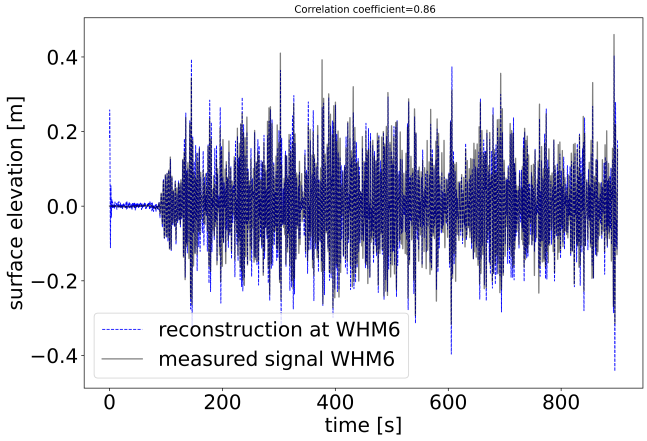

Figure C.2.: Measured elevation signal versus the reconstruction at that location of the signal for R201

Table C.2.: The selected wave heights for obtaining maximum branch deflections

R201		*S201*	
H (m)	**frame**	H (m)	**frame**
0.23	484	0.020	3440
0.29	2037	0.029	2947
0.33	1306	0.033	366
0.48	1508	0.046	4593
0.50	1677	0.050	4395

could only be approximated as the exact position of the camera and the flag relative to the reference object were unknown. A sensitivity analysis was performed to visualize the range of expected outcomes. The following ranges in values were considered:

- length of the branch, l_{br} = 3 $\pm$ 1 m,
- distance flag from wall, dy_{w-flag} = 0.64 $\pm$ 0.2 m and dz_{w-flag} = 0.5 $\pm$ 0.2 m, and
- the relative distance of the camera to the flag: dx_c= 4 $\pm$ 1 m ; dy_c=3.11 $\pm$ 1 m dz_c=5.69 $\pm$ 1 m.

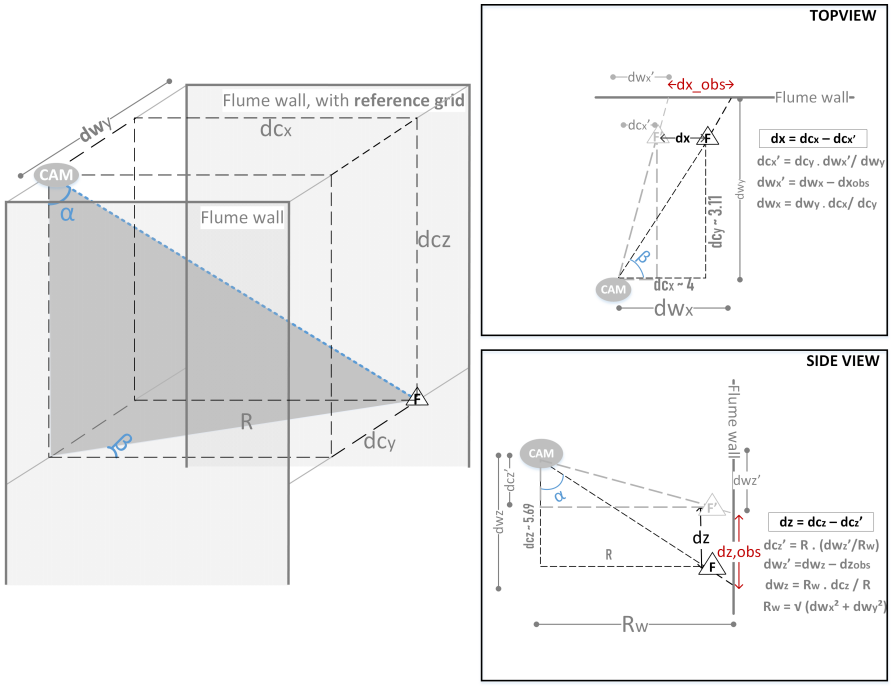

Figure C.3.: The correction applied in x-direction following the flag on the *class*2, medium branch.

C.3. Difference in Wave damping by Re

The aim of this section is to get an indication of how much of the measured overestimation of wave damping could be assigned to the Reynolds differences of the different branches. Firstly, the average drag coefficient was determined for the smallest and the largest branches. These values are based on Figure 3.9, showing the C_D-*Re* relation for a smooth rigid cylinder.

Table C.3.: Average values from *Re*-C_D graph of a smooth cylinder.

$C_{D,average}$	**Real-scale tests**	**Scaled tests**
Largest branches (order 3)	1.15	1
Smallest branches (order 1)	0.93	1.58

Afterwards, the weighted average drag coefficient of the canopy was calculated, where the weight is assigned to the ratio of the total frontal area. Tables C.4 and C.5 show the weighted average drag coefficient for the live tree and 3D-printed tree

respectively. All the branches in the real-scale experiments can be considered to be in turbulent flow conditions, as even the smallest branches have a Reynolds number $\geq 10^3$ (see Figure 3.9); hence, the weighted average drag coefficient of the canopy is expected to be around 1.

Table C.4.: Weighted drag coefficient calculation for the average live tree

Live tree							
Branch-order	**Nb(units)**	**D(m)**	**L(m)**	**Frontal area(m^2)**	**Weight**	C_D	C_{DW}
Class 1							
3 (Primary branch)	3	0.053	2.52	0.200	0.046	1.15	0.053
2	32	0.008	0.56	0.071	0.016	0.93	0.015
1	133	0.004	0.39	0.104	0.024	0.93	0.022
Class 2							
3 (Primary branch)	28	0.032	2.52	1.129	0.258	1.15	0.297
2	296	0.0051	0.56	0.422	0.096	0.93	0.090
1	1239	0.0047	0.39	1.135	0.259	0.93	0.241
Class 3							
3 (Primary branch)	57	0.01	0.82	0.234	0.053	1.15	0.061
2	239	0.0059	0.57	0.402	0.092	0.93	0.085
1	1001	0.0034	0.4	0.680	0.155	0.93	0.145
				4.38	1		**1.01**

Table C.5.: Weighted drag coefficient calculation for the average 3D-printed tree

Printed tree							
Branch-order	**Nb(units)**	**D(m)**	**L(m)**	**Frontal area(m^2)**	**Weight**	C_D	C_{Dw}
Class 1							
3 (Primary branch)	3	0.0053	0.252	0.002	0.055	1	0.055
2	24	0.001	0.056	0.001	0.019	1.58	0.029
1	48	0.001	0.039	0.001	0.026	1.58	0.041
Class 2							
3 (Primary branch)	28	0.0032	0.252	0.011	0.311	1	0.311
2	168	0.001	0.056	0.005	0.130	1.58	0.205
1	336	0.001	0.039	0.007	0.180	1.58	0.285
Class 3							
3 (Primary branch)	57	0.001	0.082	0.002	0.064	1.58	0.102
2	114	0.001	0.057	0.003	0.089	1.58	0.141
1	228	0.001	0.04	0.005	0.126	1.58	0.198
				0.04	1		**1.37**

The above tables show that approximately 60% of the entire frontal-surface area of the average printed willow tree is assigned to the branches with a diameter of 1 mm, the remaining branches are *order* 3 branches (i.e., largest branches) and, hence, are assigned to have a drag coefficient of 1. The weighted average drag coefficient of the

canopy is around 1.37 for the printed trees.

This increase of drag coefficient (1.01 to 1.37) is approximately 37%. As the drag coefficient is linearly related to the damping ratio (β), β also increases with 37% if all other parameters (such as A_v) are kept constant. The formula C.5 and C.6 show that for the forest width of 40 metres (= constant) and wave damping of 20% (Transmission coefficient, 1-0.20 = 0.80), the damping ratio, β is around 0.00625. Increasing β by 37% (β=0.00856) leads to a transmission coefficient of 0.74, hence a wave damping ratio of 26% for the same forest in a lower Reynolds regime. As previously mentioned, a maximum 30% wave height damping was measured in the scaled experiments, and a significant amount of this can be attributed to the differences in Reynolds numbers, following the reasoning above.

C.3.1. Analytical Formulation

The analytical solution stems from the energy balance equation:

$$\frac{\partial(Ec_g)}{\partial x} = \varepsilon_v, \tag{C.1}$$

where E is the amount of wave energy per horizontal area = $1/8\rho g H^2$; ρ = fluid density; H = wave height; c_g is the wave group velocity; ε_v = time-averaged energy dissipation rate per unit area due to vegetation. In this case the energy dissipation by vegetation will be the sum of dissipation by every single vegetation layer, as described in *Suzuki (2011)*.

$$\varepsilon_v = \sum_{i=1}^{I} \varepsilon_{v,i} \tag{C.2}$$

where

$$\varepsilon_{v,i} = \int_{-h+\alpha_{i-1}\cdot h}^{-h+\alpha_i \cdot h} F u \, dz$$

In which F is often simplified as the drag force (namely the pressure/ or form drag force) on the plant and u is the horizontal orbital velocity.

The general solution of the balance equation (first order ODE) is:

$$\frac{H_s}{H_{s,0}} = \frac{1}{1 + \frac{B_0(H_{s,0}/1.416)}{2}x} = \frac{1}{1+\beta x}, \tag{C.3}$$

where

$$\beta = \frac{1}{3\sqrt{\pi}} \frac{k_p}{\sinh kh(\sinh 2kh + 2kh)} \left[\sum_{i=1}^{I} C_{D,i} N_i b_{v,i} (\sinh^3 k_p \alpha_{i-1} h - \sinh^3 k_p \alpha_i h) + 3(\sinh k_p \alpha_{i-1} h - \sinh k_p \alpha_i h) \right] \left(\frac{H_{s,0}}{1.416} \right),$$

Where $N_i b_{v,i}$ can be written as one parameter, called the frontal surface area of vegetation in layer i, $A_{v,i}$. This β from Equation C.3 accounts for wave energy dissipation by vegetation and the flume walls, therefore now referred to as $\beta_{veg\&flume}$. However, we need to remove the bottom friction and wall friction effects and find β_{veg}. For this, we use calibration tests (i.e., tests without vegetation). From the calibration tests, we find β_{flume}. This is according to the study of *Maza et al. (2019)*.

$$\frac{1}{1+\beta_{veg}x} = \frac{1}{1+\beta_{veg\&flume}x} - \frac{1}{1+\beta_{flume}x}, \tag{C.4}$$

where

$$\frac{H_{m0,veg}}{H_{m0,veg,in}} = \frac{1}{1+\beta_{veg\&flume}x}$$

, and

$$\frac{H_{m0,no\,veg}}{H_{m0,no\,veg,in}} = \frac{1}{1+\beta_{flume}x}$$

For simplicity, we assume a one-layer schematization of the forest, with constant frontal-surface area along the height as we showed that the frontal-surface area between the two scales was similar – the only vegetation parameter that varies is the drag coefficient (C_D). The definition used in this work for wave damping was according to *van Wesenbeeck et al. (2022)*:

$$Dr = \frac{H_{m0,no\,veg} - H_{m0,veg}}{H_{m0,in}}, \tag{C.5}$$

This is equivalent to:

$$\frac{H_{m0,no\,veg} - H_{m0,veg}}{H_{m0,in}} = 1 - \frac{1}{1+\beta_{veg}x} \tag{C.6}$$

Thus, an increase of 10 percentage points of Dr will lead to a decrease of 10 percentage points of $\frac{1}{1+\beta_{veg}x}$.

D

SUPPORTING INFORMATION CHAPTER 4

D.1. Full Program

D.1.1. Hydrodynamic Conditions

The positions of the measuring equipment (Wave gauges and Force transducer) are shown in Table D.1.

Table D.1.: Positions of the wave gauges and force transducer.

	X (m)	Notes
WG1	4.05	
WG2	4.35	
WG3	4.95	
WG4	9.65	(before 16.01.2023, WG4 was 9.51 m)
WG5	9.95	
WG6	10.55	
WG7 & FT	11.3	
WG8	14.57	
WG9	14.87	
WG10	15.47	

Table D.2.: Comparing characteristics of tree A1 and tree D1.

		Tree A1	**Tree D1**
Trunk	height (m)	0.84	0.63
	diameter (cm)	30.88	22.92
Knot	height (m)	0.47	0.29
	diameter (cm)	70	58
Tree height	(m)	6.7	6.4
Canopy	Nclass1 (-)	10	6
	Nclass2 (-)	19	18
	Nclass3 (-)	39	30
Canopy height	(m)	5.39	5.48
Total frontal area	(m^2)	6.4	4.7

D.2. Printer settings

The printer (*Ultimaker S7 Pro Bundle*) was used with a different printer setting depending on the filament. The table below shows an overview of the important printer settings for each object (cone) and material.

	Material	E_m (MPa)	Color	Leverancier
Large cone	PLA	3200(Stiff)	black	ultimaker
	TPU 95	56	red	ultimaker
	Filaflex TPE Ultra-Soft70A	7.5	red	filament2print
	Filaflex 60A Pro	5	black	filament2print
Medium cone	PLA	3200(Stiff)	black	ultimaker
	TPU 95	56	red	ultimaker
	Filaflex TPE Ultra-Soft70A	7.5	red	filament2print
	Filaflex 60A Pro	5	black	filament2print
Small cone	PLA	3200(Stiff)	black	ultimaker
	Soft PLA-Flexible	40	neutral	filament2print

D.3. Fenton

D.4. Dynamic response cone

The numerical model in *ter Meulen et al. (2024)* (applied on an Offshore Wind Turbine) is applied for conical shapes. The equation of motion in the model is expressed as:

$$M\ddot{x}(t) + C\dot{x}(t) + Kx(t) = F(t), \tag{D.1}$$

where M is the mass matrix, C is the damping matrix, and K is the stiffness matrix; F(t) is the applied load in time, x(t) is the displacement in time (response), $\dot{x(t)}$ is the velocity and $\ddot{x(t)}$ is the acceleration. The material properties (material density and Young's modulus) are known, and hence, the M and K are known. Furthermore, we assumed a modal damping ratio of 5% for all the segments.

As mentioned above, the cone is modelled as a clammed cantilever tapered beam. The cone is initially divided into 10 segments; having 10+1 number of nodes. By performing frequency domain decomposition, we plotted the first 4 modes for a cylinder (E= 7.5 MPa with D= 0.016 m) and for our Large cone (E= 7.5 MPA, D_b= 0.0345 m, D_t= 0.001 m). Furthermore, we used a constant material density of 1.09 g/cm^3, gravitational constant of 9.81 m/s^2, and fluid density of 1000 kg/m^3.

The modal shapes for both cylinder and cone shape are shown in the figure below.

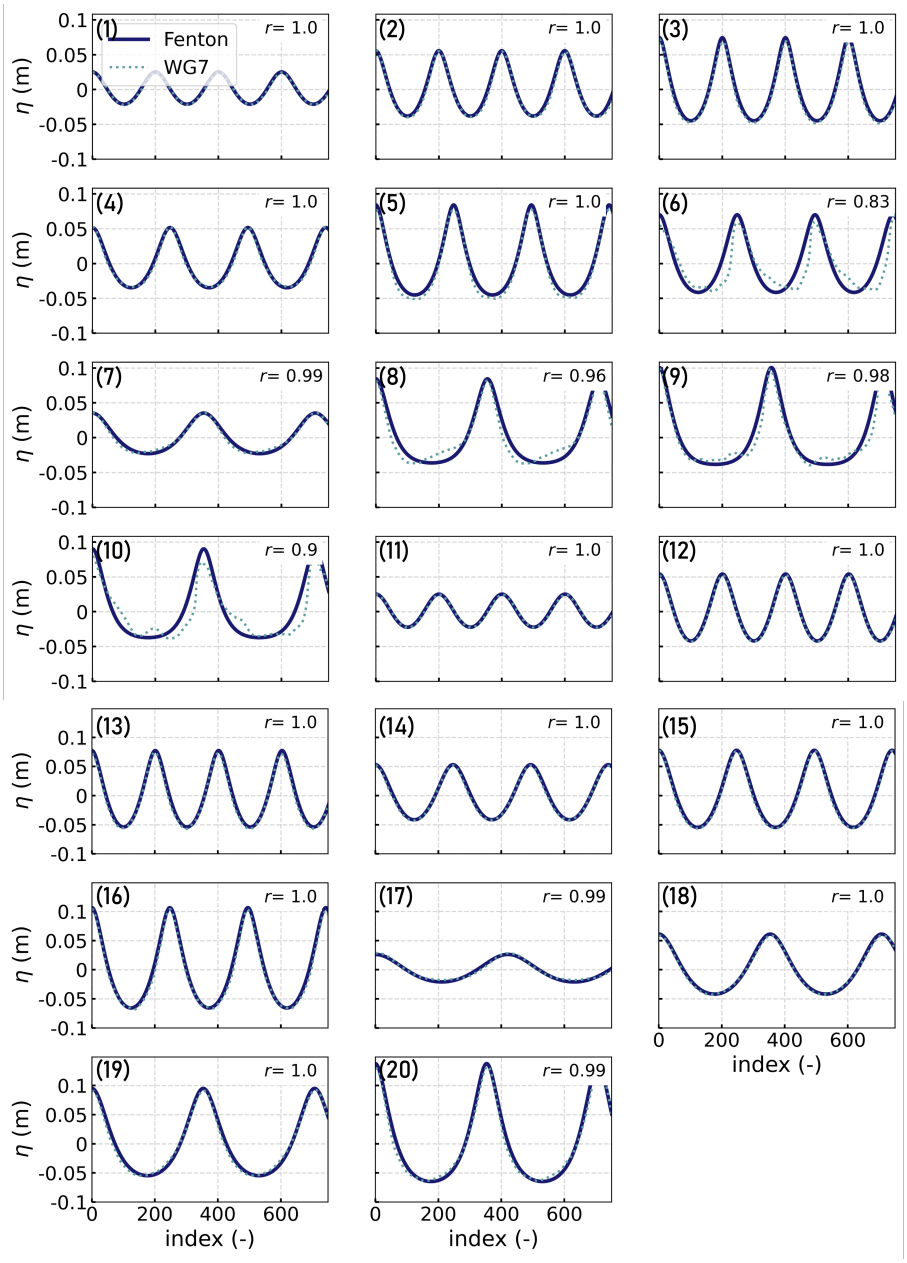

Figure D.1.: Comparing the surface elevation (η) from Fenton to WG7 (measured) of all tests (1-20), with correlation coefficient (r).

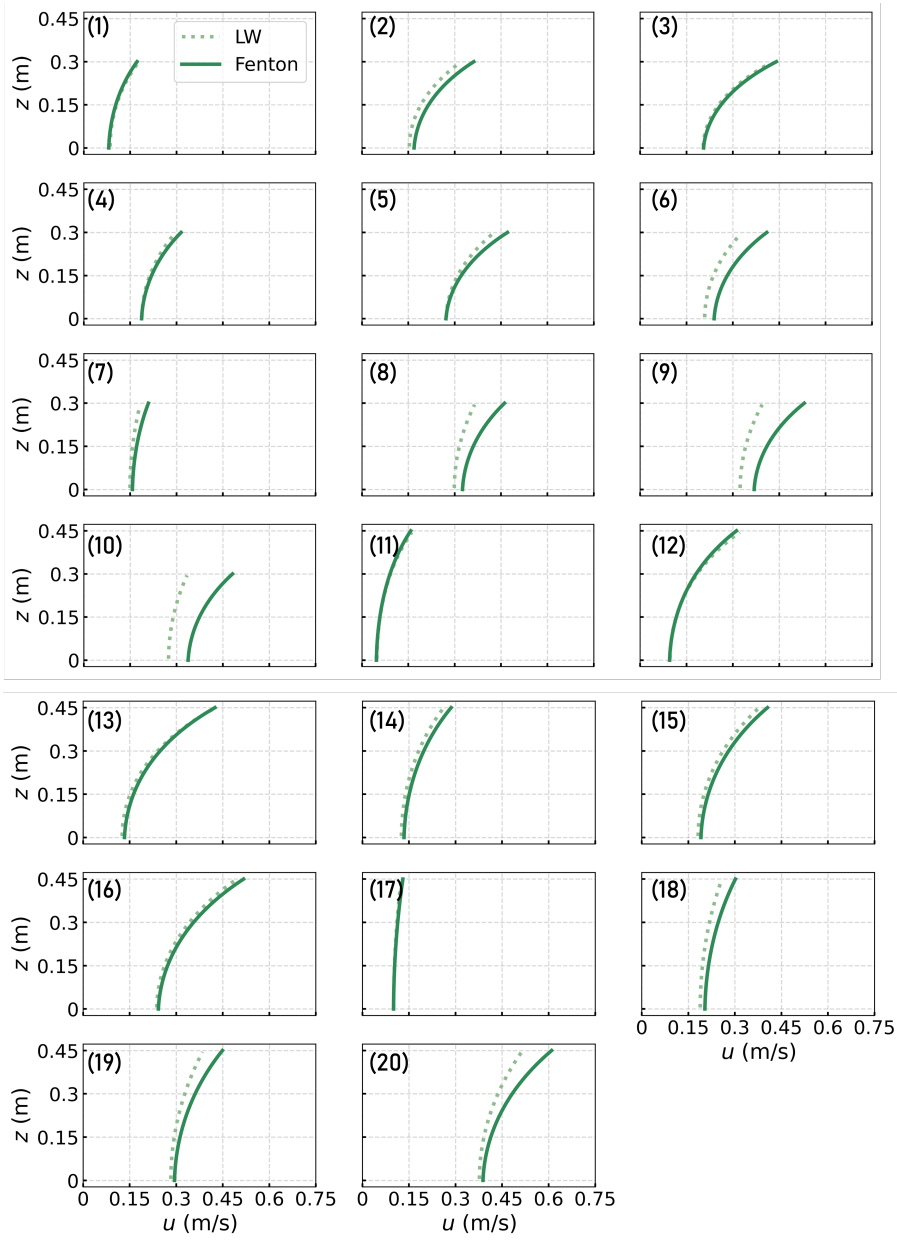

Figure D.2.: Comparing the velocity profile from Fenton theory with Linear wave theory (LW) all tests (1-20).

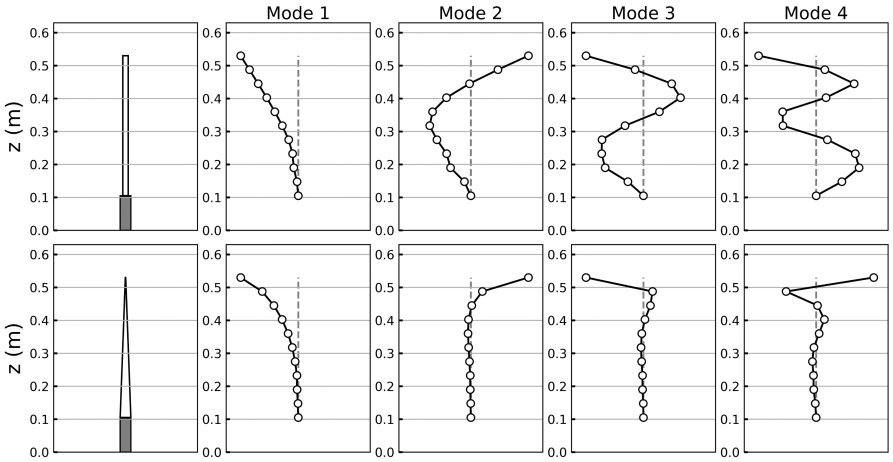

Figure D.3.: Comparing the modal shapes of a cylinder versus a cone.

D.5. Video Images - Post processing

The video data is synchronized with the remaining data (e.g., WG and FT data). The wave gauge and force data were gathered in the same Dasylab file, hence these data sets are already synchronized. Firstly, the surface elevation was detected *in front* and *behind* the object. This was done until a peak of 5 mm was found within this video data. This short data set of the video data was afterwards correlated with the Wave Gauge ($WG7$) data that was positioned inline with the cone. The shift just in the center ($t_{0,vid}$) of the object is assumed to be the average of the time found in front and behind the object. Correlation values between video data and wave gauge data were minimum 0.9.

Secondly, 5 developed waves were chosen for the analysis in this work, where 20 frames of each wave cycle was used to obtain the shape of the objects. The shape of the object was obtained for each of these frames by cropping the surroundings of the cones; the colours are masked depending on the colour of the cones (white or yellow) and the light brightness during the tests (see Figure D.4); object thinning was applied to get the centre line of the object; finally storing the pixel coordinates of the centre line (see Figure D.5C).

From pixel coordinates to metres, for this we distinguish the parts that are above water versus under water because they have slightly different pixel transformations (1 $pixel_{water}$= 0.555 m , 1 $pixel_{dry}$= 0.625 mm). Finally, statistical analysis using student t-distribution for the outcome of the 5 waves.

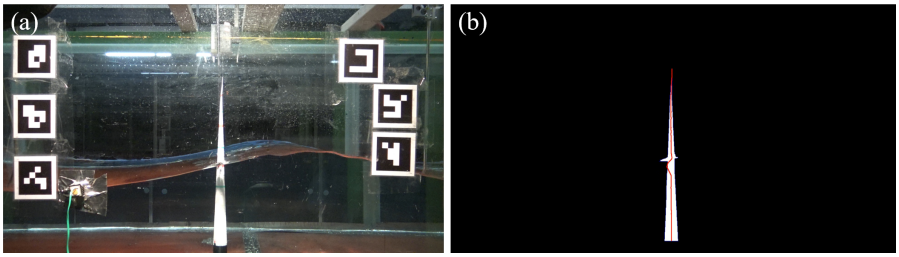

Figure D.4.: Example of the result after colour mask applied (b) on the original image (a).

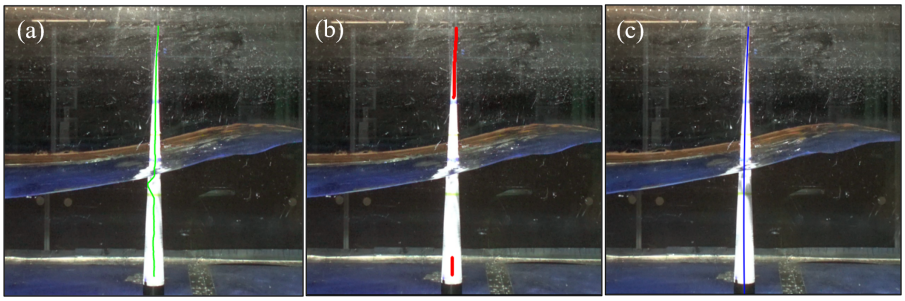

Figure D.5.: Interpolating between tip and base of the cone to remove the waterline.

D.6. Force-velocity relation complex tree

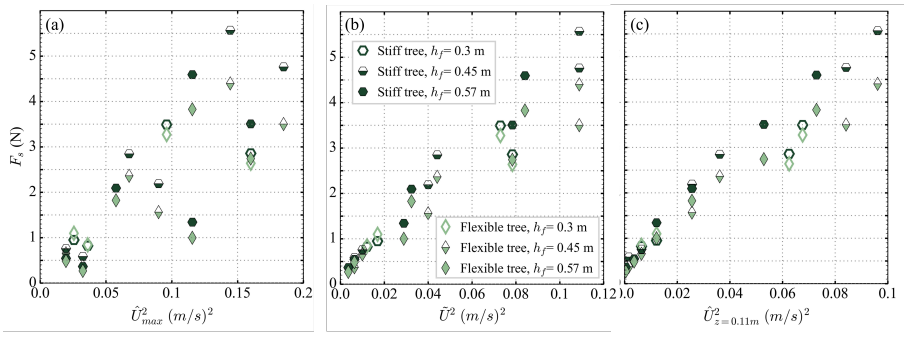

Figure D.6.: Comparing the Force-velocity relations

D.7. Possible High Frequency Oscillations in Force Data

In some cases, higher cone forces were found for the flexible Large cones compared to the stiff Large cones. This could be due to the high frequency oscillations of the higher modes (tip oscillations), which can be also reflected in the measured force time series. Below you can find a comparison between the measured forces during the rigid Large cone and during the flexible cones (7.5 MPA Large Cone) for **test 15**. The measured peak force was defined as the average maxima found for the 5 subsequent waves. It can be seen from Figure D.7A, that the stiff cone shows less deviation in the peak values between the individual waves. On the other hand, Figure D.7B shows that for the flexible Large cone (7.5 MPa), the force signal shows a 'spike' in the first wave that appears to decrease for following individual waves.

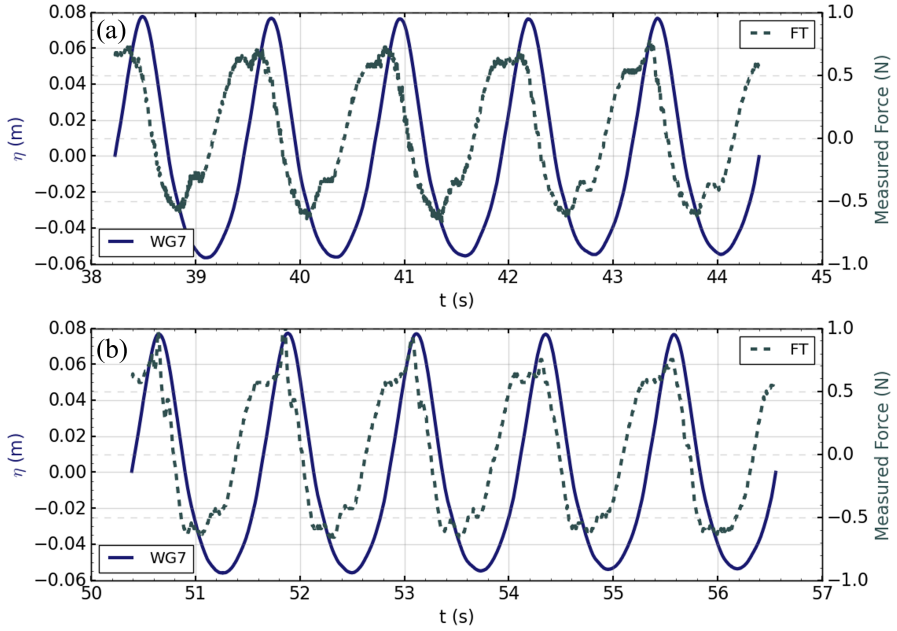

Figure D.7.: A: Force measurement of the 'Stiff Large cone' test 15 (cone+trunk); B: force measurement of the '7.5 MPa Large cone' test 15 (cone+trunk)

D.8. Peak Forces on Cones

The peak forces on the total object, namely the trunk and the cone, are given in Table D.3. The peak forces on solely the cone and the cone deflections are shown in Table D.4 and Table D.5, respectively.

Table D.3.: Overview of the peak forces on the single cones and trunk.

Test	Large Cone Stiff	Large Cone 56 MPa	Large Cone 7.5 MPa	Large Cone 5 MPa	Med Cone Stiff	Med Cone 56 MPa	Med Cone 7.5 MPa	Med Cone 5 MPa
T01	0.319	0.308	0.311	0.32	0.165	0.161	0.162	0.158
T02	0.682	0.653	0.642	0.706	0.357	0.358	0.35	0.381
R03	1.147	1.193	0.997	0.981	0.45	0.487	0.438	0.46
T04	0.759	0.804	0.749	0.754	0.38	0.372	0.367	0.358
T05	1.133	1.272	1.328	1.259	0.548	0.534	0.495	0.456
T06	1.419	1.409	1.339	1.363	0.577	0.504	0.404	0.398
T07	0.296	0.284	0.285	0.295	0.166	0.165	0.161	0.161
T08	0.971	0.863	0.996	0.938	0.388	0.36	0.289	0.312
T09	1.51	1.396	1.713	1.517	0.671	0.639	0.323	0.365
T10	1.894	1.617	1.419	1.448	0.621	0.6	0.421	0.416
T11	0.23	0.224	0.23	0.23	0.109	0.102	0.104	0.102
T12	0.458	0.438	0.45	0.474	0.223	0.23	0.211	0.191
T13	0.609	0.56	0.577	0.611	0.3	0.3	0.289	0.276
T14	0.461	0.446	0.473	0.468	0.264	0.266	0.249	0.243
T15	0.7	0.706	0.848	0.667	0.37	0.356	0.317	0.308
T16	1.008	0.958	1.127	0.939	0.521	0.455	0.408	0.353
T17	0.249	0.238	0.241	0.246	0.139	0.139	0.137	0.14
T18	0.416	0.386	0.518	0.42	0.232	0.205	0.215	0.202
T19	0.833	0.802	0.976	0.85	0.458	0.401	0.392	0.397
T20	1.364	1.329	1.321	1.24	0.726	0.671	0.526	0.508

Table D.4.: Overview of the peak forces on the cones (excluding trunk).

Test	Large Cone Stiff	Large Cone 56 MPa	Large Cone 7.5 MPa	Large Cone 5 MPa	Med Cone Stiff	Med Cone 56 MPa	Med Cone 7.5 MPa	Med Cone 5 MPa
T01	0.197	0.191	0.193	0.2	0.051	0.057	0.045	0.046
T02	0.544	0.521	0.543	0.535	0.213	0.182	0.157	0.173
T03	1.045	1.055	0.933	0.875	0.284	0.307	0.188	0.141
T04	0.679	0.724	0.69	0.693	0.221	0.221	0.143	0.166
T05	0.963	1.085	1.187	1.124	0.325	0.356	0.25	0.218
T06	1.098	1.224	1.185	1.235	0.371	0.29	0.225	0.224
T07	0.201	0.191	0.189	0.202	0.073	0.076	0.071	0.069
T08	0.831	0.731	0.899	0.825	0.235	0.232	0.185	0.173
T09	1.517	1.191	1.48	1.255	0.378	0.364	0.23	0.203
T10	1.66	1.052	1.273	1.05	0.31	0.371	0.274	0.177
T11	0.15	0.144	0.151	0.15	0.035	0.028	0.033	0.032
T12	0.33	0.298	0.325	0.313	0.131	0.107	0.093	0.076
T13	0.486	0.476	0.516	0.456	0.189	0.145	0.123	0.126
T14	0.386	0.352	0.455	0.395	0.188	0.151	0.157	0.156
T15	0.638	0.674	0.844	0.668	0.307	0.254	0.222	0.225
T16	0.948	0.887	1.1	0.912	0.457	0.403	0.301	0.247
T17	0.164	0.162	0.185	0.166	0.052	0.054	0.052	0.049
T18	0.377	0.354	0.473	0.392	0.19	0.165	0.169	0.161
T19	0.731	0.7	0.885	0.787	0.367	0.306	0.307	0.306
T20	1.184	1.147	1.19	1.086	0.555	0.498	0.365	0.337

D.9. Peak Forces on 6-Cone Tree

Table D.5.: Overview of the measured deflections.

Test	Large Cone Stiff	Large Cone 56 MPa	Large Cone 7.5 MPa	Large Cone 5 MPa	Med Cone Stiff	Med Cone 56 MPa	Med Cone 7.5 MPa	Med Cone 5 MPa
T01	-	-	0.44	-	-	-	1.64	3.00
T02	-	-	1.09	1.29	-	0.78	10.78	-
T03	-	-	1.85	2.70	-	1.63	15.68	20.67
T04	-	-	0.55	1.35	-	0.78	10.85	13.04
T05	-	-	2.62	4.05	-	2.70	19.93	24.54
T06	-	-	0.00	-	-	-	-	-
T07	-	-	0.43	-	-	0.01	2.19	2.71
T08	-	-	2.07	2.42	-	1.35	15.64	16.94
T09	-	-	-	-	-	-	-	-
T10	-	-	-	-	-	-	-	-
T11	-	-	0.43	0.55	-	0.05	2.62	2.38
T12	-	-	1.08	1.62	-	1.34	6.95	9.11
T13	-	-	2.83	0.00	-	2.39	10.23	10.11
T14	-	-	1.52	1.62	-	1.34	6.16	7.18
T15	-	-	2.07	2.68	-	2.67	13.28	10.90
T16	-	-	4.80	5.16	-	-	15.81	-
T17	-	-	0.43	0.33	-	0.02	3.18	3.88
T18	-	-	1.85	1.90	-	1.34	9.13	8.65
T19	-	-	2.60	3.82	-	2.95	15.02	15.16
T20	-	-	5.57	6.53	-	-	21.08	-

Table D.6.: Over of the peak forces on the 6-cone tree including and excluding the trunk.

	6*Med Cone (Total object)		6*Med Cone (excluding trunk)	
Test	**Stiff**	**7.5 MPa**	**Stiff**	**7.5 MPa**
T01	0.336	0.355	0.189	0.208
T02	1.112	0.979	0.773	0.64
T03	2.063	1.405	1.645	0.987
T04	1.317	1.011	0.973	0.667
T05	2.079	1.554	1.645	1.12
T06	2.61	1.482	2.224	1.096
T07	0.411	0.393	0.262	0.244
T08	1.558	0.947	1.307	0.696
T09	2.708	1.306	2.383	0.981
T10	2.648	1.59	2.323	1.265
T11	0.234	0.248	0.134	0.148
T12	0.613	0.486	0.419	0.292
T13	1.056	0.685	0.789	0.418
T14	0.767	0.63	0.532	0.395
T15	1.366	0.939	1.052	0.625
T16	2.124	1.218	1.764	0.858
T17	0.389	0.357	0.259	0.227
T18	0.777	0.626	0.607	0.456
T19	1.442	1.054	1.212	0.824
T20	2.453	1.462	2.154	1.163

E

SUPPORTING INFORMATION CHAPTER 5

E.1. Vegetatielegger

The Vegetatielegger (since 2014) is a map with information of where different types of vegetation are allowed to be in the Netherlands owned by Rijkswaterstaat, it takes into account the river discharge, water quality, and nature enhancement conform to the Waterwet (since 2009). The vegetation types on the map include 4 homogeneous vegetation classes, namely: Gras en akker, Riet en ruigte, Bos, Struweel; and 3 Mixed vegetation classes, namely: Mengklasse 90/10, Mengklasse 70/30, Mengklasse 50/50.

The classification into four homogeneous vegetation types was based on roughness, indicating the extent to which vegetation can hinder river discharge and, as a consequence, increase river water level. The vegetation height is an important parameter regarding the roughness and is therefore also a key distinction between the homogeneous classes. Specifically, gras and akker have a maximum height of 50 cm, riet and ruigte can reach up to 1 to 2 metres, struweel is between 2 and 5 metres (struiken), while bos is 5- 15 metres in height. An important difference between 'bos' and 'struweel' is that bos has a limited amount of branches in the first few layers compared to struweel, making struweel the roughest vegetation class as a consequence (Figure E.1).

The vegetation of 'mengklasse' (mixed class) is classified following Table E.1, showing the minimal percentage of the vegetation type with the lowest roughness and the

maximum percentage of the vegetation type with the highest roughness.

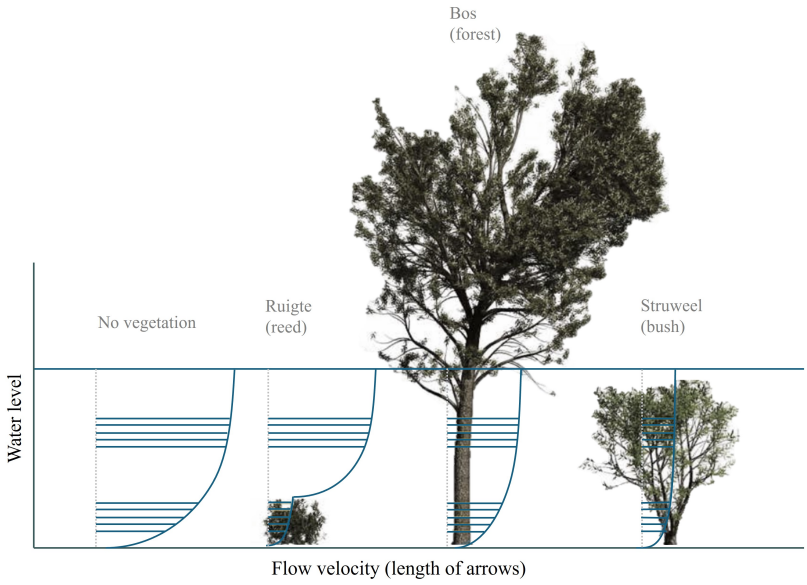

Figure E.1.: Vegetation schematization in riverine areas and their affect on the flow velocity, adjusted from *Peters et al. (2006)*.

Table E.1.: Description of mixed vegetation classes of the VEGETATIE LEGGER.

mixed class	**gras & akker**	**riet & ruigte**	**bos**	**struweel**
70/30	minimum 30 %	maximum 40 %		Undefined
50/50	minimum 10 %	Undefined	Maximum 60 %	
90/10	minimum 80 %	maximum 20 %		

It is important to note that in the case of a homogeneous vegetation class type at some location, there is room to develop a higher roughness class than the one given on the map, if this new vegetation area is < 500 m^2. It is therefore easier to change to a less rough vegetation class than to a rougher vegetation class, to avoid the river discharge issues. Lastly, removing vegetation that is already present in the area is not easily allowed from a water quality perspective, this needs to conform to the Waterwet.

E.2. Dike Design

When the incident waves break, the wave impact zone of the dike slope is affected (subsection E.2.2). Afterward, the wave front moves upward; this upward motion continues until it reaches a maximum height R_u, after which the wave flows back down the slope (subsection E.2.3). If the run-up height exceeds the crest height, overtopping occurs (subsection E.2.1), allowing water to flow over the crest and down the inner slope.

E.2.1. Overtopping

Formulation 4.3 from *(van der Meer et al., 2018)* is used, namely:

$$\frac{q}{\sqrt{g \cdot H_{m0}^3}} = \frac{0.023}{\sqrt{\tan\alpha}} \cdot \gamma_b \cdot \xi_{m-1,0} \cdot \exp -(2.7 \frac{R_c}{\xi_{m-1,0} \cdot H_{m0} \cdot \gamma_b \cdot \gamma_f \cdot \gamma_\beta \cdot \gamma_v})^{1.3}, \quad \text{(E.1)}$$

with a maximum of:

$$\frac{q}{\sqrt{g \cdot H_{m0}^3}} = 0.09 \cdot \exp -(1.5 \frac{R_c}{H_{m0} \cdot \gamma_f \cdot \gamma_\beta \cdot \gamma_v})^{1.3}, \quad \text{(E.2)}$$

where

$$\xi_{m-1,0} = \frac{\tan\alpha}{\sqrt{\frac{H_{m0}}{L_0}}} \quad \text{(E.3)}$$

and the deep water wave length $L_0 = \frac{gT^2}{2\pi}$.

E.2.2. Wave impact

We calculate the resistance time for the top-layer (t_{top}) and the sub-layer (t_{sub}). The resistance of the top-layer:

$$t_{top} = f_\alpha \frac{1}{c_b} ln[\frac{max((H_{m0} - c_c);0)}{c_a}]$$

The resistance time for the sub-layer depends on the total thickness of the top-layer and the sub-layer (d_{tot}), the sand fraction (c_d) and the significant wave height. The resistance time of the sub-layer is calculated as follows:

$$t_{sub} = f_\alpha [\frac{max((d_{tot} - 0.2);0)}{c_d (1/3)^{1.5} max((H_{m0} - 0.5);0)}],$$

where $_\alpha$ is a correction factor that accounts for differences in the duration of erosion

for varying slopes, calculated in the following manner:

$$f_\alpha = \frac{\frac{(r_\alpha - 1)}{3}}{\tan\alpha} + 2 - r_\alpha,$$

where r_c is 1.51 and $c_d = 1.1 + 8 * max((f_{sand} - 0.7); 0)$

E.2.3. Wave run-up

Erosion due to wave run-up is assessed by comparing the critical overload D_{crit} with the cumulative overload $D_{load,z}$. The critical overload represents the strength of the grass revetment, and depends on the level of damage/failure. *de Waal and van Hoven (2015)* stated two different values for damage and failure of the grass revetment, namely $D_{crit,damage} = 4000\ m^2/s^2$ and $D_{crit,failure} = 7000\ m^2/s^2$.

The cumulative overload $D_{load,z}$, as presented by *de Waal and van Hoven (2015)* for a stationary storm event is calculated as follows:

$$D_{load,z} = \sum_{i=1}^{N} max\left[(\alpha_m U_{i,z}^2 - \alpha_s U_{crit}^2); 0\right]), \tag{E.4}$$

where $U_{i,z}$ is the front velocity of the wave run-up for a single wave i on the evaluation level z; U_{crit} is the critical velocity; α_m is a correction factor for increased load; and α_s a correction factor for decreased strength (e.g., at transitions and objects such as stairs and roads). These α-factors are set equal to 1. Furthermore, N is the number of waves during a time interval $N = \frac{3600\Delta T}{T_m}$, with ΔT as the load duration of a stationary event (constant still water level) and T_m is the mean wave period.
The critical front velocity U_{crit} represents the quality of the grass revetment, with lower values indicating weaker revetments. For stronger grass revetments, U_{crit} is 6.60 m/s, while for weaker ones, it is 4.30 m/s. Overload occurs when the front velocity $U_{i,z}$ exceeds U_{crit}, and the cumulative overload $D_{load,z}$ is calculated by summing up all instances of overload.

The front velocity of the wave run-up $U_{i,z}$ is calculated as follows:

$$U_{i,z} = U_{i,max} \cdot max\left(0; min\left(1; \frac{Ru_i - z}{0.25 Ru_i}\right)\right), \tag{E.5}$$

where $U_{i,max}$ is the maximum front velocity along the slope of wave run-up i at a certain evaluation level above the still water level ($z = z_{eval} - z_{swl}$), $U_{i,max} = c_u\sqrt{gRu_i}$, where c_u is a constant equal to 1.1 *(de Waal and van Hoven, 2015)* and Ru_i is the run-

up level of run-up event i with respect to the water level.

The run-up level Ru_i of run-up event i with respect to the water level is calculated as follows:

$$Ru_i = Ru_{2\%} \sqrt{\frac{ln\left(1 - \frac{i}{N+1}\right)}{ln(0.02)}}, \tag{E.6}$$

where $Ru_{2\%}$ is the 2% run-up level, the run-up level that is exceeded by 2% of incident waves and the number of waves N. With the 2% run-up level $Ru_{2\%}$ described in *van der Meer et al. (2018)* as follows:

$$\frac{R_{u2\%}}{H} = a \cdot \gamma_b \cdot \gamma_f \cdot \gamma_\beta \cdot \xi \tag{E.7}$$

With a maximum of:

$$\frac{R_{u2\%}}{H} = b \cdot \gamma_f \cdot \gamma_\beta \left(4 - \frac{1.5}{\sqrt{\gamma_b \cdot \xi}}\right), \tag{E.8}$$

where a and b are stochastic normal-distributed variables; γ_b, γ_f and γ_β are influence factors for a berm, roughness elements, and oblique wave attack, respectively. ξ is the Iribarren number (or breaker parameter), as shown in Equation E.3.

LIST OF SYMBOLS

α_{shape}	alpha shape factor	–
α	angle of side branch	°
α_i	ratio of the depth of layer i	–
$\bar{D}$	average diameter throughout the length of the cone	m
ε_v	averaged energy dissipation by vegetation	$N/m/s$
$\hat{U}_{h,max}$	horizontal orbital velocity at the waterline according to linear wave theory	m/s
ν	kinematic viscosity fluid	m^2/s
ω	wave radian frequency	s^{-1}
ρ_w	fluid density	kg/m^3
θ	deflection of slender tree branches	°
$\tilde{Ca}$	averaged Cauchy number	–
$\tilde{L}$	averaged dimensionless number for the relative velocity between branch and fluid	–
$\tilde{U}$	depth-averaged maximum horizontal velocity following Linear Wave Theory	
ξ	breaker parameter	–
A_v	frontal-surface area density per tree	$m/tree$
B_f	length of the forest perpendicular to the dike	m
c_d	sand fraction	–
D	cumulative overload parameter	m^2/s^2
$D_{crit,failure}$	critical cumulative overload parameter	m^2/s^2
d_{min}	minimum branch diameter (of a first order branch)	m
d_{tot}	total thickness of the top-layer and sub-layer	m
f_n	correction factor scaled experiment	–

F_p	averaged peak force	N
F_s	significant peak forces	N
f_{cor}	a correction factor based on the number of blocked laser beams	–
h_d	water depth at deep water	m
h_{tree}	tree height	m
L_0	deep water wave length	m
q_{tol}	maximum allowable overtopping discharge	l/s/m
Rc	mimimum crest freeboard	m
t_{load}	duration of the wave load	hrs
t_{sub}	resistance time for the sub-layer	hrs
t_{top}	resistance time for the top-layer	hrs
$\widetilde{C}_D$	bulk drag coefficient	–
$A_{TLS,n}$	total frontal-surface area obtained from TLS measurements	m^2/tree
$A_{veg,i}$	total vegetation width per horizontal area	m^{-1}
b_v	average diameter of the individual stems	m
C_{D_can}	drag coefficient for the canopy layers	–
C_{D_tr}	drag coefficient for the trunk layers	–
C_{Dw}	weighted average drag coefficient of the canopy based on diameter sizes	–
c_g	wave group velocity	–
C_M	inertia coefficient	–
D_B	Branch diameter at the location above the knot	m
D_{canopy}	canopy diameter	m
D_{knot}	knot diameter	m
D_{trunk}	trunk diameter	m
Dr	wave damping ratio by vegetation	–
dx	maximum branch deflection	m
E_m	Young's modulus of the model	MPa
E_p	Young's modulus of prototype	MPa
F_D	drag force	N
F_i	inertia force	N
f_n	correction factor for scale and model effects	–
Fr	Froude number	–

g	gravitational acceleration constant	m/s^2
H	wave height	m
h	water depth	m
h_v	height of the vegetation that is submerged	m
H_{canopy}	canopy height	m
h_f	water depth at the foreshore	m
H_{knot}	knot height	m
H_{m0}	significant wave height estimated from wave spectrum	m
$H_{rms,in}$	root-mean-square wave height in front of the forest	m
H_{rms}	root-mean-square wave height	m
H_{trunk}	trunk height	m
I	second moment of area	m^4
k	wave number	m^{-1}
KC	Keulegan-Carpenter number	–
L	branch length	m
l_{cone}	length of the cone	m
L_m	model length scale	m
L_p	real-world length scale	m
N	number of vegetation stems per horizontal area	$units/m^2$
N_b	number of side branches	–
N_{class1}	number of branches of diameter class 1	–
N_{class2}	number of branches of diameter class 2	–
N_{class3}	number of branches of diameter class 3	–
$N_{l,t}$	total amount of laser points by the laser scanner	–
N_l	total amount of laser point blocked in the layer before reaching layer n	–
n_L	scale factor	–
r	penetration distance of a laser beam	m
R_B	ratio that includes the number of side branches per mother branch	–
R_D	diameter ratio between subsequent order of branches	–
R_L	length ratio between subsequent order branches	–
Re	Renolds number	–
$Ru_{2\%}$	2% run-up level	m

T_p	peak wave period	s
U_{crit}	critical front velocity depending on quality of revetment	m/s
u_h	horizontal orbital velocity	m/s
x	distance inside the forest	m
M	moment due to external load	Nm

ACKNOWLEDGEMENTS

This PhD journey has been nothing short of an adventure, a path that I would describe as ‘unexpected’. When I applied on that November day in 2019, I believed in the topic and thought “niet geschoten is altijd mis”. Little did I know that this decision would lead me down a road full of surprises—some challenging, others deeply rewarding, but all of them invaluable. As I reflect on these years, I realise that what made this journey truly special were the people who shared it with me. This acknowledgement is for you, those who supported, guided and celebrated with me.

From the beginning, my choice to apply for this PhD was not just about the topic. During my Master’s thesis, I worked with an incredible team and that experience stayed with me. Bas Hofland and Bregje van Wesenbeeck, you were instrumental then, and I thank you for giving me this opportunity and your guidance during my entire PhD journey. Bas, your support and your ability to address every question—no matter how simple or complex—were invaluable. I am very grateful for your supervision that you’ve always given with enthusiasm, your critical insight, and openness. Bregje, you have been a true mentor—empowering and encouraging me in many moments during my PhD. Thank you for your invaluable guidance, support, and constructive feedback over the years. I was also very lucky to work closely together with Alejandra and Coco in Woody, I really appreciate our collaboration and all your support during these years.

I also thank Stefan Aarninkhof for being my promotor in the early stages of the PhD. Your broad perspective and valuable insights that added to the first stages of the research. I still remember when I submitted the first paper; for this, I also want to thank José Antolinez. Your support in publishing my first article, your investment in my growth, and your ongoing encouragement were deeply motivating. Juan López, thank you for your support and input in the discussion chapter of the thesis. During the Ph.D., I have learnt a lot from many meetings and presentations. First, I would like to thank all the members of WOODY user group, special thanks to Tjeerd Bouma, Robert Slomp, Daphne van der Wal, Guido Wolters, Samantha Haage and

Maartje van Dijk for all your input. To the Master's and Bachelor's students I had the chance of working with—Max, Kelvin, Rushil, Madelief, April, Eli, Anxiang, and Bart—you taught me a lot, and I am grateful for the opportunity to learn alongside you. The experiments in the water lab were another cornerstone of this journey. Thanks to Pieter, Chantal, Ari, Arno, Frank, and Jennifer: I am thankful for all your help during this period. Thanks to Mischa for sharing your beautiful photographs with me to include in this thesis. King, a special thanks to you for making the impossible possible—especially with those thin 3D-printed branches—was remarkable; and your ongoing genuine support. To everyone who helped create the tree replicas, thank you, especially to Parmodini, Achraf and Vlad for your patience with this.

My time in Ghent added a beautiful chapter to this story. Peter Troch, thank you for hosting me and your hospitality. I felt really welcomed and had the motivation to write the Flexibility chapter with pleasure in your department. I also want to thank my office mates in Ghent - Joe, Raphael, Felipe, Paulino, Timothy, and Laurens- thank you for making me feel welcomed and filling those cold December days with such warmth.

The third floor became my "home base"—a place of countless coffee breaks, and brainstorming sessions. It was a constant in all the unknowns of this PhD. Chit and Jennifer, your coffee catch-ups on the first floor always brought positivity to my mornings. My office room 3.62 shared with Paul, Gijs, Jakob, Mario, Vincent, Flores, Tosca, and Bart. Together, I think we created a space filled with great memories (like our fun interior decorating and music hours), where work felt enjoyable and inspiring – thank you a lot. A big thank you to all my colleagues that in general made this a beautiful experience at the university; special thanks to Lisa, Roy, Menno, Marlies, Ligaya, Ana, Jill, Anne, Christa, Anna, Jelle, Paul, Mia, Valeria, Otti, Inge, Natasha, Sargol, Floor, and Jianwei.

Balancing the demands of a Ph.D. required not skipping work-outs (and psor) sessions. Thank you Ermano, Federica, Ties, Dorette, Dimitris, Camilo, Jos, Vidya, Robert, Jessica, Jerom, Danny, Juan, Gaby, Rogellio, and Moni for all the good times, whether it were serious coffee breaks or serious (psor) drinks. Chris, Patricia, Gina, Valeria, Pengxu, and Mike, thank you for all your support, especially encouraging me to keep taking care of myself and going to the gym. Chris, I am very happy that we still had a short overlap in Ph.D. time before Covid started; I have learnt a lot from you and thank you for the proof-reading sections of my thesis. To my friends—Manon, Shan, D'tasha, Samantha, Natalia, and Ceylan— thank you for always cheering for me. Natalia and Samantha, our surfing adventures came at just the right moments,

offering a much-needed escape. Tatjana, thank you for being there during both the highs and the lows, a true friend through it all.

Finally, to my family: Parmodini, Avinash, Davini and Leo thank you for your unwavering support. Shiro and Amadou, I am grateful for all our discussions and your advice. And to my parents, Papa and Mama, your unconditional love and support have always been my foundation on which all this is built.

ABOUT THE AUTHOR

Sudarshini Kalloe was born on 11 July 1995 in Paramaribo, Suriname. She obtained her high school diploma from the Miranda Lyceum in 2012, Paramaribo. In 2015, she obtained her Bachelor of Science degree from the Faculty of Civil Engineering and Geosciences at Delft University of Technology and continued her studies in the Master of Science programme in Civil Engineering at the same faculty. She obtained her Master of Science degree in 2019 with a thesis entitled *'Wave damping potential of woody riparian vegetation'*. After graduating, she worked at Van den Herik as a tender engineer.

In 2020, she started her Ph.D. study at the Department of Hydraulic Engineering in the Faculty of Civil Engineering and Geosciences, Delft University of Technology.

Photography by Mischa Keijser

As the wave comes by, the willow branches bend as if in a fluid dance. In their wake, their side-branches flicker, as though waving the passing wave goodbye.

The Author